

The Contribution of Swirl Recovery to the Induced Drag of Propeller-Wing Systems

MSc Thesis

Robert Kooij

Delft University of Technology

The Contribution of Swirl Recovery to the Induced Drag of Propeller-Wing Systems

MSc Thesis

by

Robert Kooij

to obtain the degree of Master of Science
at the Delft University of Technology,
to be defended publicly on Friday February 3, 2023 at 9:30 AM.

Student number:	4444531	
Thesis committee:	Prof. Dr. Ir. L. L. M. Veldhuis	TU Delft, chair
	Dr. Ir. T. Sinnige	TU Delft, supervisor
	Ir. R. Nederlof	TU Delft, supervisor
	Dr. Ir. D. Ragni	TU Delft
Date:	Tuesday 24 th January, 2023	

An electronic version of this thesis is available at <http://repository.tudelft.nl/>.

Cover image retrieved from:
https://en.wikipedia.org/wiki/Airbus_A400M_Atlas on 28/11/2021.

Preface

This thesis is written as the final part in the fulfillment of the Master of Science degree in Aerospace Engineering. After my bachelors, I chose Flight Performance, which fully gratified my expectations and more. With this thesis, my time as a student, which I enjoyed very much, has come to an end.

It has not been possible to reach this point by myself. Therefore, I would like to thank all the teachers who helped me during my educational career. For the duration of this thesis, I especially would like to thank my supervisors, R. Nederlof and T. Sinnige, for their help in the understanding of propeller-wing systems and feedback on my work.

Furthermore, I would like to thank my parents for the fantastic opportunities and support they have always given me. Moreover, I greatly thank my two brothers, who I can always count on, and my girlfriend, who always encourages me to achieve my goals and supported me throughout the duration of the thesis.

Robert Kooij
Delft, January 2023

Summary

Due to the desire to reduce the impact of traveling on the environment and the increase in fuel prices over the past years, the propeller has regained interest as a propulsion mechanism in the aviation industry. One of the reasons for this is the high propulsive efficiency of propellers compared to turbojet engines. Furthermore, electric motors are well suited to combine with propellers, and their efficiency is rather insensitive to scaling such that the propeller can be placed at different positions around the aircraft structure resulting in new design freedoms. The placement of the propeller influences the aerodynamic performance of the aircraft. When the propeller is placed in front of the wing, which is a so-called tractor configuration, the propeller slipstream influences the aerodynamic performance characteristics of the wing.

The increase in axial velocity increases the dynamic pressure over the surface of the wing, such that the lift of the wing is increased within and around the slipstream. The flow within the propeller slipstream also contains a swirling motion. The swirl, or tangential velocity, in the slipstream is a loss of energy as this does not contribute to the production of the thrust of the propeller. The tangential velocity in the propeller slipstream changes the local angle of attack of the wing sections behind the propeller. Behind the propeller side where the blades are moving up, an increase in the local angle of attack of the wing results in an increase in the magnitude of the resultant force. Besides the increase in magnitude, the increase in the angle of attack results in a rotation of the resultant force vector into the direction of flight. Behind the other side of the propeller, where the blades are moving down, the local angle of attack of the wing is reduced resulting in a decrease in the magnitude of the resultant force. The reduction of the angle of attack also rotates the resultant force vector towards the trailing edge of the wing. When the resultant forces of both wing sections are decomposed in the direction of flight, a net force results in the direction of flight, which is the swirl recovery of the wing. Part of the lost energy from the propeller in the form of a swirling motion is recovered by a net force that reduces the drag of the propeller-wing system. Depending on the propeller-wing system, the swirl recovery can be positive, such that the drag of the wing is reduced, or negative, such that the drag of the wing is increased. Swirl recovery is similar to the lift-induced drag of the wing which results from the rotation of the resultant force vector toward the trailing edge of the wing due to downwash, which follows from the generation of lift by the wing.

Previous studies on the aerodynamic interaction between propeller and wing systems show the benefits of placing the propeller in front of the wing such that the total induced drag of the wing, which is the combination of the lift-induced drag and swirl recovery, reduces. In this research, the relative contribution of the lift-induced drag and swirl recovery is analyzed by a decomposition of the total induced drag of the wing, such that maximum performance benefits can be obtained from the aerodynamic interaction between the propeller and wing for future designs.

A numerical model based on the potential flow theory is developed to conduct a parametric study on the induced drag of propeller-wing systems. One of the advantages of the numerical model compared to alternative methods to analyze propeller-wing systems, such as CFD or wind tunnel experiments, is the ability to decouple the influence of the wing-induced and the propeller-induced velocities on the aerodynamic performance of the wing resulting in the lift-induced drag and swirl recovery, respectively. Furthermore, the computational expense of the numerical models based on the potential flow theory is generally low, enabling an analysis of many different propeller-wing system configurations. The propeller, modeled to operate at maximum efficiency, is used for the parametric study to obtain realistic ratios between axial and tangential velocities in the propeller slipstream. With various thrust settings of the propeller, the propeller-induced velocities are controlled. The Fokker F-27 is used as a reference for realistic sizing of the propeller-wing system configuration. The lift coefficient of the wing was fixed for different propeller-wing configurations during the performed analyses with the low-order numerical tool. This allows for a better comparison of the relative contribution of the lift-induced drag and swirl recovery of the system from an aircraft design perspective.

The gradient of the isolated wing lift distribution is an important parameter when considering the induced drag of propeller-wing systems. From analyses with the low-order numerical tool, the contribution of the swirl recovery is found to be dominant over that of the lift-induced drag for the operating points of the propeller with inboard-up configurations that are used in the parametric study. The most benefit is obtained from positive swirl recovery when the lift of the isolated wing section behind the up-rotating side of the propeller is larger compared to the lift of the wing section behind the down-rotating side of the propeller. This is the case when the propeller is placed at a position where the gradient of the isolated spanwise wing lift distribution is large. This is partially in line with the literature, in which conclusions are made that inboard-up rotating configurations result in a reduction of the induced drag of the wing. When the propeller is placed where the gradient of the isolated spanwise wing lift is positive from root to tip, an inboard-down configuration can lead to a reduced induced drag of the wing.

The propeller-induced velocities are increased by a velocity multiplication factor. With this increase, it is shown that for lower disk loadings, the contribution of the net positive swirl recovery is larger than the increase in the lift-induced drag by the increased gradient of the spanwise wing lift distribution. The axial and tangential velocities within the propeller slipstream are larger for higher disk loadings. This increases the difference in the lift at the wing sections behind the two propeller sides, increasing the net positive swirl recovery contribution to the induced drag of the wing. By higher disk loadings, the difference in the lift of the two wing sections behind the propeller sides increases such that the net positive swirl recovery increases. With this increase in lift difference, the gradient of the spanwise wing lift distribution increases, such that the contribution of the lift-induced drag becomes larger than the contribution of the net positive swirl recovery.

The parametric study conducted in this thesis provides improved insight into the relative contribution of the lift-induced drag and swirl recovery to the total induced drag of the wing in propeller-wing systems. From the conclusions made, design choices can be substantiated to increase the performance of propeller-wing systems, resulting in a reduction of fuel consumption within the aviation industry.

Contents

Preface	i
Summary	ii
List of Figures	viii
List of Tables	ix
Nomenclature	x
1 Introduction	1
I Background	5
2 Isolated Propeller & Wing Characteristics	6
2.1 Isolated Propeller Characteristics	6
2.1.1 Propeller Performance	6
2.1.2 Propeller Slipstream Velocities	7
2.2 Drag of the Isolated Wing	7
2.2.1 Isolated Lift-Induced Drag	7
2.2.2 Parasite Drag	9
3 Propeller-Wing Interaction Fundamentals	10
3.1 Effects of the Wing on the Propeller	10
3.2 Effects of the Propeller on the Wing	11
3.2.1 Effects on the Lift Distribution	11
3.2.2 Lift-Induced Drag of Propeller-Wing Systems	12
3.2.3 Swirl Recovery of a Wing with Infinite Span	12
3.3 Literature on Propeller-Wing Systems	14
4 Modeling of Propeller-Wing Systems	16
4.1 Interaction Modes	16
4.2 Potential Flow Theory	16
4.2.1 Relevance & Assumptions	17
4.2.2 Limitations	17
4.3 Propeller-Wing System Analysis Methods	17
4.3.1 Numerical Propeller & Wing Models	17
4.3.2 Propeller-Wing System Models	18
4.4 Modeling Approach	18
II Numerical Model & Validation	20
5 Numerical Model of the Propeller-Wing System	21
5.1 Propeller Model	21
5.1.1 BEM Model	22
5.1.2 Slipstream Tube Model	23
5.1.3 Axial Velocity Averaging	24
5.2 Wing Model	26
5.2.1 VLM Formulation for Propeller-Wing Systems	27
5.2.2 Jet Correction	29
5.2.3 Modeling of Lift-Induced Drag for Propeller-Wing Systems	32
5.2.4 Modeling of Swirl Recovery	35
5.3 Propeller & Wing Model Integration	36

6	Validation of the Numerical Model	38
6.1	Isolated Propeller Model	38
6.1.1	BEM Model	38
6.1.2	Slipstream Tube Model.	39
6.2	Isolated Wing Model	41
6.2.1	XFLR5 Verification	42
6.2.2	Experimental Validation	42
6.3	Propeller-Wing System.	43
6.3.1	Spanwise Propeller Location.	44
6.3.2	Rotational Direction of the Propeller.	46
6.4	Limitations of the Numerical Model	47
III	Results & Conclusions	49
7	Results of a Parametric Study on Propeller-Wing Systems	50
7.1	Setup of the Parametric Study	50
7.1.1	Propeller Operating Point	50
7.1.2	Wing Properties.	51
7.1.3	Presentation of the Results	52
7.2	Drag Decomposition for Spanwise Propeller Positions	54
7.2.1	Spanwise Performance	54
7.2.2	System Performance.	56
7.3	Drag Decomposition for Propeller Rotational Directions	58
7.3.1	Spanwise Performance	58
7.3.2	System Performance.	59
7.4	Variation of the Spanwise Lift Distribution	61
7.5	Dominating Induced Drag Component	63
7.6	Variation of the Aspect Ratio of the Wing	66
7.7	Variation of the Taper Ratio of the Wing.	67
7.8	Discussion	68
8	Conclusions	70
8.1	Conclusions.	70
8.2	Recommendations	71
	References	75
	Appendices	76
A	Lifting-Line Theory & Vortex Lattice Method Comparison	76
A.1	Induced Drag by LLT & VLM.	76
A.2	Trefftz Plane Analysis	77
B	Prabhu Correction for Downwash of Propeller-Wing Systems	79
C	Swirl Averaging	82
D	Prabhu-Rethorst Correction	84
D.1	Cosine Velocity Distribution	85
D.2	Operating Point 1.	85
D.3	Computational Time	86

List of Figures

1.1	The NASA X-57 Maxwell conceptual aircraft with distributed propulsion and wingtip-mounted propellers.	1
1.2	Schematic of induced velocities on the sectional forces of the airfoil from a propeller-wing system.	2
1.3	Thesis outline.	3
2.1	Breakdown of slipstream velocity components induced by the propeller.	7
2.2	Schematic of wingtip vortices.	8
2.3	Two-dimensional section of a finite wing with relevant angles, velocities, and forces.	8
3.1	Schematic of the influence of the wing on the propeller.	11
3.2	Decoupled and combined effects of the propeller slipstream on the spanwise lift distribution of the wing.	12
3.4	Effect of the spanwise propeller position, y_p . The relevant system parameters of the APROPOS propeller-wing system are $J = 0.92$, $c_T = 0.127$, $\alpha_p = 0$ degree, and $\alpha = 4.2$ degrees.	14
3.5	Effect of the spanwise lift distribution on the induced drag of the wing.	15
4.1	Global overview of the numerical model.	19
5.1	Overview of the numerical model with details of the propeller model.	21
5.2	Velocity parametrization from the BEM including the dummy variable Ψ	22
5.3	Visualization of the slipstream tube model.	24
5.4	Direct and averaged axial propeller-induced velocities with an advance ratio of 0.8 at $x = 1.52R$	25
5.5	Schematic of radial strip i for averaging the axial velocity over the height of the propeller.	25
5.6	Spanwise coefficients for the direct and averaged axial velocities of a propeller at OP 1 at $y_p = 0.5b/2$ with radius $r_p = 0.13b/2$	25
5.7	Overview of the numerical model with details of the wing model.	26
5.8	Top view of the VLM with horseshoe vortices.	27
5.9	Definition of a single panel used in the VLM model.	27
5.10	Propeller-wing system geometry used for the correction method.	30
5.11	Wing with virtual wing extension for the correction of non-center located propeller slipstreams.	30
5.12	Comparison of the lift distribution for a wing with jet with $r_j/b = 0.1$ at $y/b = 0.25$	31
5.13	Influence of the correction of the mirror propeller at OP 1 located at $y_p = 0.2b/2$ with radius $r_p = 0.2b/2$ with only the axial propeller-induced velocities.	32
5.14	Results directly following from the Rethorst correction with $R/b/2 = 0.143$ and $\mu = 0.667$	33
5.15	Schematic of the downwash by the trailing vortices from a wing in a jet.	33
5.16	Downwash of the centered located jet by the circulation based on only the freestream velocity.	34
5.17	Lift-induced drag of a wing with a center located jet with $\mu = 0.667$	34
5.18	Lift-induced drag distribution with a tip located jet with $\mu = 0.667$	34
5.19	Circulations with local and freestream velocities as reference for the center and tip jet with $\mu = 0.667$	35
5.20	Side view of the propeller-wing system configuration within the propeller slipstream for the analysis in Part III.	36
5.21	Top view of the propeller-wing system configuration for the analysis in Part III.	37

6.1	Validation of the BEM model with data from the isolated propeller in the experiment of Sinnige et al.	39
6.2	Induced velocities by the BEM method and slipstream tube model at $x = R$ for $J = 0.8$	40
6.3	Induced velocities by the BEM method and slipstream tube model at $x \rightarrow \infty$ for $J = 0.8$	40
6.4	Induced velocities by the slipstream tube model and the CFD analysis at $x = 0.19R$ from Sinnige et al.	41
6.5	Validation of the VLM with <i>XFLR5</i>	42
6.6	Model 2 of the wind tunnel experiment from Sinnige et al. where the propeller is located at the wingtip.	42
6.7	Validation of the VLM with experimental data from Sinnige et al..	43
6.8	Front view of the conventional propeller-mounted configuration of model 2 of the wind tunnel experiment from Sinnige et al..	44
6.9	Drag polar of the propeller-wing system for a conventional and tip-mounted inboard-up rotating propeller.	45
6.10	Technical drawing of model 1 from the experiment from Sinnige et al..	46
6.11	Validation of the numerical model with the experimental results from model 1 from Sinnige et al. with a flap deflection of 10 degrees.	47
7.1	Propeller operating points at maximum efficiency in the BEM model.	51
7.2	Propeller-induced velocities and their resulting angle of attack change over the propeller radius.	52
7.3	Definition of the wing sections for different spanwise propeller positions for the propeller-wing system.	53
7.4	Spanwise coefficients for an inboard-up rotating propeller at OP 1 located at $y_p = 0.5b/2$	54
7.5	Spanwise coefficients for an inboard-up rotating propeller at OP 1 located at $y_p = b/2$	56
7.6	Drag decomposition for spanwise positions of an inboard-up rotating propeller.	56
7.7	Spanwise coefficients for a propeller at OP 2 located at $y_p = b/2$	58
7.8	Lift-to-drag ratios with respect to the baseline configuration with different operating points.	60
7.9	Drag decomposition for inboard-down and inboard-up rotating propellers at various spanwise positions at OPs 1 and 5.	60
7.10	Lift distributions for inboard-up and inboard-down rotating propellers at the tip for OPs 1 and 5.	60
7.11	Spanwise performance of the wing with twist with propellers at OP 1 at $y_p = 0.25b/2$	62
7.12	System drag decomposition for inboard-up and inboard-down rotating propellers at OP 1.	62
7.13	Local change of angle of attack influencing the local spanwise coefficients.	62
7.14	Spanwise velocity and lift by the arbitrary tangential velocity with $u_{z_{amp}} = 0.25U_\infty$	64
7.15	System drag decomposition by the arbitrary tangential velocity.	64
7.16	System drag decompositions for the systems with propeller-induced velocities increased by the velocity multiplication factor (VMF).	65
7.17	System drag decomposition for aspect ratios of the wing with a tip-mounted propeller at OP 1.	66
7.18	Spanwise coefficients scaled by the maximum values of the isolated wing with AR of 9.33 for a tip-mounted propeller at OP 1 for wings with aspect ratios of 9.33 and 18.67.	67
7.19	Lift distributions and drag decompositions of the wing with taper ratios of 1.0 and 0.2 with propeller at OP 1.	67
A.1	Lift-induced drag obtained with the LL theory and VLM.	77
A.2	Trefftz plane for the lift-induced drag calculation.	77
A.3	Schematic of the Trefftz plane analysis for an isolated wing.	77
A.4	Lift-induced drag obtained with the VLM and Trefftz plane analysis for a wing with aspect ratio of 10.	78
B.1	Circulation distribution divided into parts for the Prabhu downwash correction	79
B.2	Vortex shedding into the wake by parts.	79
B.3	Downwash distribution obtained by the Prabhu method.	80
B.4	Lift-induced drag distribution with a center located jet with $\mu = 0.667$	80

B.5	Jet velocity located at the wingtip.	81
B.6	Incorrect downwash distribution obtained with the Prabhu correction for a tip-located jet with $\mu = 0.667$	81
C.1	Swirl averaging applied to a sine wave with an amplitude of 5 m/s.	82
C.2	Spanwise performance by the influence of the swirl averaging method.	83
D.1	Discretization method of a non-uniform axial velocity profile for the Prabhu-Rethorst correction.	84
D.2	Axial velocity distributions for the Prabhu-Rethorst correction.	85
D.3	Corrections for the cosine axial velocity distribution.	86
D.4	Corrections for the propeller at OP 1 axial velocity distribution.	87

List of Tables

5.1	Subscript notation for jet correction.	31
7.1	Propeller operating points (OP) for during the analysis.	51
7.2	Propeller-wing system performance results for two different propeller positions.	55
7.3	Maximum drag reduction obtained with the inboard-up rotating propeller for different OPs.	57
7.4	System performance of inboard-up and inboard-down rotating propellers mounted at the tip of the wing.	59
7.5	System performance of a twisted wing with inboard-up and inboard-down rotating propellers mounted at $y_p = 0.25b/2$	61
C.1	System coefficients of the system with averaged swirl velocities with respect to the direct configuration.	83

Nomenclature

Abbreviations

AD	Actuator disk
BEM	Blade element momentum
CFD	Computational fluid dynamics
FIM	Full interaction mode
HOFW	Higher-order free-wake
LL	Lifting-line
OP	Operating point
SIM	Single interaction mode
SMF	Swirl multiplication factor
VLM	Vortex lattice method
VMF	Velocity multiplication factor

Latin letters

AR	Aspect ratio	–
B	Number of propeller blades	–
b	Wing span	m
c	Chord length	m
C_D	System drag coefficient	–
c_d	Sectional drag coefficient	–
C_L	System lift coefficient	–
c_l	Sectional lift coefficient	–
c_P	Propeller power coefficient	–
c_T	Propeller thrust coefficient	–
D	Drag	N
D	Propeller diameter	m
d	Sectional drag	N/m
e	Oswald efficiency factor	–
F	Aerodynamic influence coefficient	–
F	Tip correction factor	–
G	Rethorst correction to the aerodynamic influence coefficient	–
g	Airfoil camber shape function	N
J	Advance ratio	–
L	Lift	N
l	Sectional lift	N/m
M	Mach number	–
m	Mass	kg
n	Rotational speed	1/s
R	Propeller radius	m
R	Resultant force	N
r	Radial coordinate	–
Re	Reynolds number	–
S	Wing surface area	m ²
T	Thrust	N
U	Velocity	m/s
u	Propeller induced velocity	m/s
v	Propeller-induced velocity in BEM formulation	m/s
W	Total velocity in the BEM formulation	–
w	Velocity in z-direction	m/s
x	Flight direction	–

x_v	Propeller offset in streamwise direction	m
y	Spanwise direction	—
z	Vertical direction	—

Greek letters

α	Angle of attack	°
β	Propeller blade angle	°
Γ	Circulation	m ² /s
γ	Vorticity strength of shed element	m/s
ε	Velocity ratio in the Prabhu correction	—
η	Efficiency	—
η	Non-dimensional spanwise coordinate in the Rethorst correction	—
η	Spanwise location of trailing vortex in the Prabhu correction	m
θ	Wing twist angle	°
λ	Local advance ratio	—
λ	Wing taper ratio	—
μ	Velocity ratio for the Rethorst correction	—
ρ	Density	kg/m ³
φ	Angular position	°
φ	Swirl angle	°
Ψ	Dummy variable in BEM method	rad
Ω	Angular velocity of the propeller	rad/s

Subscripts

a	Axial direction
b	Bound vortex
$base$	Value of the base configuration
D	Drag
d	Sectional drag
dir	Obtained with direct swirl for slipstream tube model
e	Even part in the Rethorst correction
eff	Effective
F	Based on the freestream
g	Geometric
IU	Inboard-up
j	Jet
j	Located within the jet in the Rethorst correction
li	Induced by the downwash
lp	Left propeller
max	Maximum
n	Normal direction
nj	No jet
np	No propeller resulting in the isolated wing
o	Located outside the jet in the Rethorst correction
o	Odd part in the Rethorst correction
OU	Outboard-up
p	Propeller
rp	Right propeller
sr	Following from swirl recovery
t	Tangential direction
w	Wake
∞	Undisturbed quantity
07	At 70% of the propeller radius

Introduction

Over the past years, the increasing fuel prices and the increase in environmental awareness have emphasized the desire to reduce fuel consumption in aviation. One method of reducing fuel consumption of aircraft is by returning to propeller propulsion due to their higher propulsive efficiency compared to turbofan propulsion [1]. Furthermore, propellers can easily be driven by electric motors, giving the possibility to fly on an electric energy source. Scaling down the size of the electric motor gives new degrees of design freedom in aircraft design, such as distributed electric propulsion [2]. An example of alternative propulsion is seen in the conceptual design of the NASA X-57 Maxwell [3], which is visualized in Figure 1.1. Distributed propulsion is combined with wingtip-mounted propellers in tractor configuration as they are located in front of the wing.



Figure 1.1: The NASA X-57 Maxwell conceptual aircraft with distributed propulsion and wingtip-mounted propellers [4].

With the increased design freedom for the propeller-wing systems by the benefits of electric propulsion, the importance of understanding the aerodynamic interactions between propeller and wing can be emphasized. Early studies [5, 6] on propeller-wing configurations have shown that performance improvements such as lift augmentation and drag reduction are obtained when propellers are placed properly.

The drag of propeller-wing systems lowers by the reduction of the induced drag of the wing [7]. The induced drag of a propeller-wing system follows from vertical induced velocities in front of the wing and consists of two components. The downwash component induced by the generation of lift by the wing results in the lift-induced drag, d_{li} , and is visualized on the left in Figure 1.2. On the right, the vertical propeller-induced velocity is visualized, resulting in the swirl recovery, d_{sr} , contributing to the thrust of the propeller-wing system. For upwash, this drag becomes negative, such that it contributes to the thrust of the system. The directions of these induced velocities, however, can vary for different propeller-wing system configurations. The propeller-induced velocities influence the spanwise lift distribution of the wing, such that both the lift-induced drag and swirl recovery are influenced.

Although there is knowledge of the benefits of the propeller placement in the design of propeller-wing systems by reducing the induced drag of the wing, it is not fully understood how the lift-induced drag and swirl recovery contribute to the induced drag of the system. In literature, induced drag has always been considered a single force. To increase the performance of future propeller-wing systems, this research focuses on the decoupling of and the interaction between lift-induced drag and swirl recovery to investigate their relative contribution to the induced drag of propeller-wing systems.

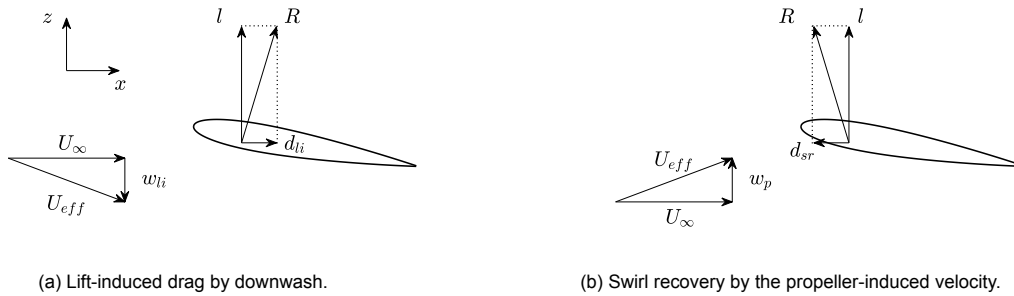


Figure 1.2: Schematic of induced velocities on the sectional forces of the airfoil from a propeller-wing system.

Research Aim and Questions

With the lack of knowledge on how the contributors of the induced drag and the lift of propeller-wing systems influence each other and contribute to the drag, a research aim is formulated such that more insight is obtained into the drag of the propeller-wing system:

Investigate the relative contribution of swirl recovery to the induced drag of the propeller-wing system, by means of a low-order numerical model.

This research aim can be obtained by finding answers to the following sub-questions:

- What are the most dominant aerodynamic performance characteristics of the propeller-wing system?
- How can the propeller-wing system be modeled such that the lift-induced drag and swirl recovery of the system can be decoupled?
- How is the spanwise position of the propeller related to the spanwise lift distribution of the wing?
- What is the relation between the induced drag contributors and the propeller-induced velocities?
- How do the aerodynamic performance characteristics of the propeller-wing system relate to each other for different system configurations?

Answers to these sub-questions give more insight into the contribution of the lift-induced drag and swirl recovery of the propeller-wing system to the induced drag of the system.

Thesis Outline

The body of this thesis consists of the current introduction followed by three parts consisting of eight chapters, as illustrated in Figure 1.3. Within Part I, background information on propeller-wing systems is provided to the reader. The physical principles of the propeller and wing are discussed individually, and a closer look is taken towards the interaction fundamentals. Hereafter, various methods of the modeling of the propeller-wing system are presented in Chapter 4, after which a modeling approach is chosen such that an analysis of the propeller-wing system can be performed. Part II covers details of the numerical model. Chapter 5 presents the details of the numerical model, and in Chapter 6 the

numerical model is validated. Discrepancies of the numerical model with results from wind tunnel experiments are discussed. In Part III, the numerical model is used to analyze various propeller-wing system configurations. Chapter 7 contains the results from the analysis conducted with the numerical model. The main findings of those results are stated in the conclusions in Chapter 8, where the discrepancies of the numerical model are taken into account. In the same chapter, recommendations for future research on propeller-wing systems are provided.

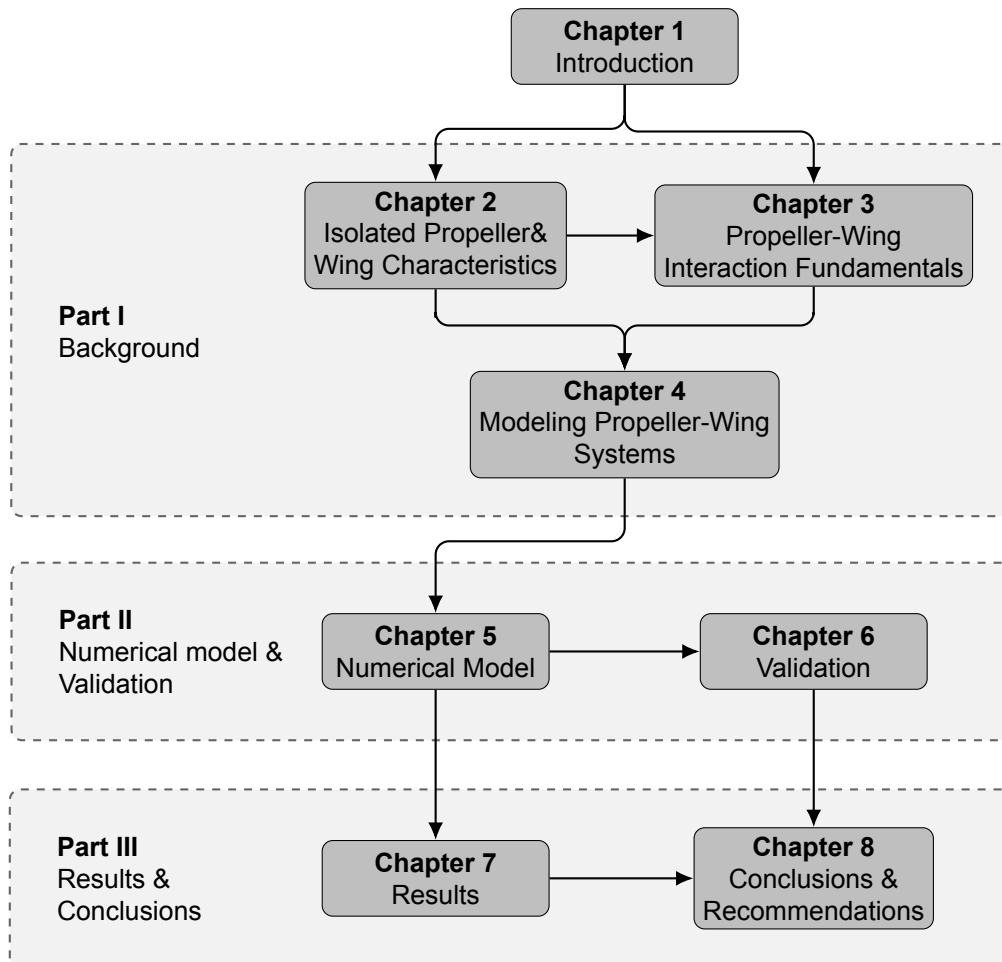


Figure 1.3: Thesis outline.

Definitions & Sign Convention

Within the literature on propeller-wing systems, various definitions and sign conventions are used for the components of the drag and induced velocities by the propeller and wake of the wing. In this section, a description is given for these forces and velocities within this thesis, such that no misinterpretation is possible for the reader. Three important definitions that are used within this thesis are clarified for the classification of the drag components:

- **Induced drag:** The drag or thrust component that results from the rotation of the resultant force vector due to any induced velocity in the vertical direction.
- **Lift-induced drag:** The drag component that results due to the rotation of the resultant force vector from the vertical velocity component induced by the wake of the wing following from the production of lift by the wing.
- **Swirl recovery:** The net thrust that results from the rotation of the resultant force vector due to the vertical velocity component induced by the propeller. In other words, this could also be defined as the propeller-induced thrust component of the system.

The induced drag of the wing is the summation of the lift-induced drag and swirl recovery. The lift-induced drag usually increases the induced drag of the propeller-wing system, whereas, for the swirl recovery, this depends on which side the section of the wing is located concerning the propeller sides. In this thesis, the swirl recovery is treated as a thrust force. This means that if it is stated that the swirl recovery increases, the drag of the system decreases. On the propeller side, where the blades are moving up, the swirl recovery is positive, reducing the drag of the system. This situation is visualized in Figure 1.2b. Although the swirl recovery is considered a thrust force, variables d_{sr} , $c_{d_{sr}}$, and $C_{D_{sr}}$ are used to indicate the contribution of the swirl recovery. During the analyses of the propeller-wing systems, the usage of these variables provides a more clear view of the contribution of the swirl recovery to the induced drag of the system. On the other side, where the propeller blades are moving down, the swirl recovery is negative such that it contributes to the drag of the system. The subscripts *li* and *sr* are used to indicate the lift-induced drag and swirl recovery components of the induced drag of the propeller-wing systems, respectively.

The definitions of the velocities induced by a jet and a propeller are distinguished. This thesis uses the jet to define a uniform axial velocity higher than the freestream velocity. A propeller slipstream has a non-uniform axial and tangential velocity profile. The jet and propeller axial velocities are indicated by the subscripts *j* and *p*, respectively.



Background

The first part of the thesis aims to provide more insight into the fundamentals of propeller-wing systems. In Chapter 2, the performance of the isolated propeller and wing are considered. When enough understanding of the isolated components is provided, the fundamentals of the propeller-wing interactions are elaborated on in Chapter 3. With the fundamentals of the propeller-wing interactions covered, well-considered decisions are made for developing a numerical model to further investigate the aerodynamic interactions of the propeller-wing system configuration.

2

Isolated Propeller & Wing Characteristics

Before propeller-wing systems can be evaluated, the isolated propeller and wing characteristics are introduced. In Section 2.1, a closer look is taken towards the isolated propeller, whereafter the isolated wing characteristics are provided in Section 2.2.

2.1. Isolated Propeller Characteristics

The propeller characteristics are divided into two parts. First, in Section 2.1.1, the performance of the isolated propellers is covered. The characteristics determine the propeller-induced velocities, which are covered in Section 2.1.2. The section gives a breakdown of the velocity components in the propeller slipstream. They are relevant in the remainder of the thesis as they have a separate influence on the performance of the wing.

2.1.1. Propeller Performance

Thrust is produced by accelerating air backward. The amount of thrust produced by the propeller or jet engine, T , can be related to the mass flow, \dot{m} , and the difference in velocity in front and behind the propeller, U_∞ and U_j , respectively. This relation is seen in Equation 2.1. The propulsive efficiency of the propeller and jet engine is a relation between the two velocities and is given by Equation 2.2. From this equation, it becomes clear that it would never be possible to obtain a propulsive efficiency of 100% when thrust is produced. From these relations, it can be clarified why propellers generally have higher propulsive efficiency compared to jet engines. The latter produces thrust by giving a relatively high acceleration to a low air volume compared to propellers [8]. A smaller difference between U_∞ and U_j increases the propulsive efficiency.

$$T = \dot{m} (U_j - U_\infty) \quad (2.1)$$

$$\eta = \frac{2}{1 + \frac{U_j}{U_\infty}} \quad (2.2)$$

The propeller parameters should be scaled to fairly compare the performances of different propellers. First, the propeller thrust and power coefficients are given by Equations 2.3 and 2.4, where n and D_p represent the rotational speed and propeller diameter, respectively. For propeller-wing systems, another thrust coefficient is relevant as it is scaled by the freestream velocity of the propeller-wing system as is seen in Equation 2.5.

$$c_T = \frac{T}{\rho_\infty n^2 D_p^4} \quad (2.3)$$

$$c_P = \frac{P}{\rho_\infty n^3 D_p^5} \quad (2.4)$$

$$T_c = \frac{T}{\rho_\infty U_\infty D^2} \quad (2.5)$$

Another parameter for comparing propellers is the advance ratio of the propeller, J , which relates the freestream velocity with the tip velocity of the propeller blades. This relation is seen in Equation 2.6. The advance ratio of the propeller is directly related to the velocity of the propeller blades through a fluid. For low values of the advance ratio, the velocity of the propeller blade is high, which results in high aerodynamic loads. The advance ratio is included in Equation 2.7, which presents the definition of the propeller efficiency, η_p [8]. Furthermore, the blade pitch, β , is an important propeller characteristic. It is defined as the angle between the propeller blade chord line and the plane of rotation of the propeller. The local blade pitch and advance ratio together determine the local angle of attack of the blade and, therefore, the forces acting on it.

$$J = \frac{U_\infty}{n D_p} \quad (2.6)$$

$$\eta_p = \frac{c_T J}{c_P} \quad (2.7)$$

2.1.2. Propeller Slipstream Velocities

A schematic visualization of the breakdown of the velocities in the propeller slipstream is given in Figure 2.1. The propeller creates a pressure jump across the disk such that the flow accelerates. This accelerated flow in the axial direction is denoted by V_a in the figure. Furthermore, the slipstream contracts, which results in the radial velocity within the slipstream. This velocity is visualized by V_r . Furthermore, due to the torque force on the propeller blades, another velocity component, V_t , results. This velocity is tangential to the direction of the rotation of the propeller blades [9]. Important to note is that only the axial velocity in the propeller slipstream contributes to the production of the thrust of the propeller.

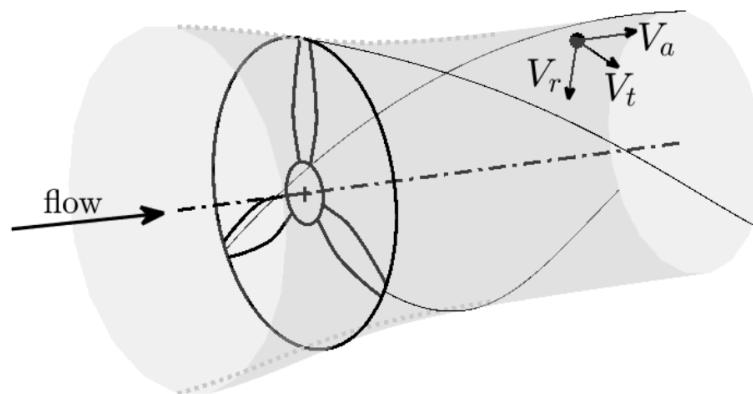


Figure 2.1: Breakdown of slipstream velocity components induced by the propeller [10].

2.2. Drag of the Isolated Wing

The performance of a wing is mainly determined by the amount of lift and drag it produces. In this section, a closer look is taken at the drag contributors of a wing. Firstly, the lift-induced drag of a wing is covered in Section 2.2.1, whereafter sorts of parasite drag are further elaborated on in Section 2.2.2.

2.2.1. Isolated Lift-Induced Drag

Wings produce lift by developing a pressure difference between their upper and lower surface. From the pressure imbalance, the flow near the tip tends to curl from the lower high-pressure side to the upper low-pressure side. This curling flow is denoted as the wingtip vortex and is visualized in Figure 2.2. It must be noted that the curling flow is strongest at the wingtip but is present in the wake over the entire span of the wing, which is also known as vortex shedding [11].

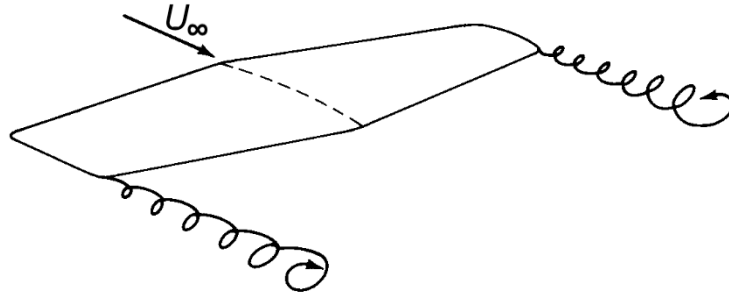


Figure 2.2: Schematic of wingtip vortices [12].

This influence of the wingtip vortex and vortex shedding is clarified best by having a closer look at a wing section as visualized in Figure 2.3. The wing section is orientated with the geometric angle of attack, α_g , with respect to the freestream. This angle includes the local twist of the wing. The curling flow in the wake of the wing creates downwash, w_{li} , which influences the incoming flow in front of the wing. The downwash reduces the effective angle of attack, α_{eff} , by the induced angle of attack, α_{li} , as is stated in Equation 2.8. The effect of the downwash from the generation of lift can be noted by its effect on the resultant force vector of the airfoil section. The resultant force vector of the airfoil section rotates with the lift-induced angle of attack. Decomposing this rotated resultant force into the direction of drag and lift, which are in the direction of flight and perpendicular to that by definition, respectively, gives the lift-induced drag of the airfoil section. The lift-induced drag is present for wings with a finite span that generates lift.

$$\alpha_{eff} = \alpha_g - \alpha_{li} \quad (2.8)$$

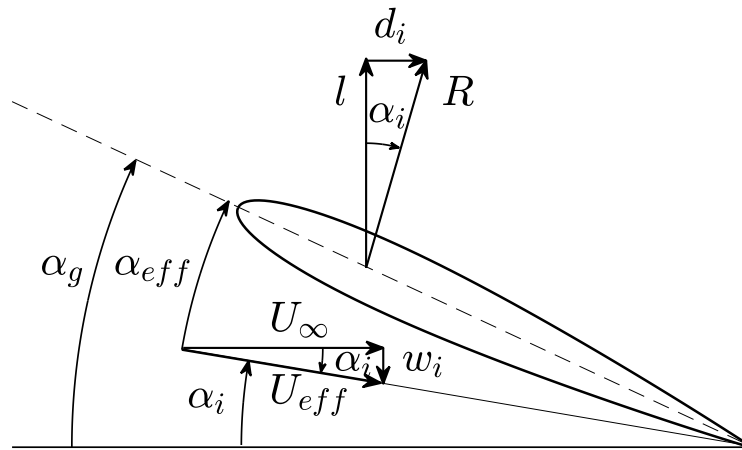


Figure 2.3: Two-dimensional section of a finite wing with relevant angles, velocities, and forces.

The total lift-induced drag for a wing is obtained with Equation 2.9. From this equation, it is seen that the lift-induced drag depends on three variables. The lift coefficient, C_L , represents the amount of lift generated by the wing. The span efficiency factor, e , represents how the lift is distributed over the span of the wing, and AR represents the aspect ratio of the wing. The overarching effect of these parameters is their influence on the strength of vortex shedding over the span of the wing, and, thereby, their influence on the lift-induced drag of the wing, $C_{D_{li}}$.

$$C_{D_{li}} = \frac{C_L^2}{\pi e AR} \quad (2.9)$$

The lift-induced drag takes a larger part of the total drag for wings at low-speed [13]. Increasing the flight speed increases the friction forces, which results in a relatively lower drag contribution of the lift-induced drag for the total drag compared to a low-speed flight. The impact of the lift-induced drag in low-speed flight conditions makes it especially interesting in the study of propeller-powered aircraft, as they often fly at lower speeds compared to aircraft powered by jet engines. For a generic subsonic jet transport, the amount of lift-induced drag is about 25% of the total drag of the aircraft. This value can increase up to 60% during take-off when the lift coefficient is high [14].

2.2.2. Parasite Drag

Besides the lift-induced drag, parasite drag influences the performance of the wing, which is not mainly dependent on the development of lift. Pressure drag and friction drag are other sorts of parasite drag [15]. Pressure drag is caused by the difference between the pressure in front and aft of an object and is mainly dependent on the shape and velocity of the object. The pressure drag arises due to flow separation. Friction drag results from the friction between a fluid, such as air, and the surface of an object moving through it. Besides the velocity and shape of the object, it is also dependent on the smoothness of the surface. The wave drag is outside the scope of the thesis as it is negligible for most propeller-driven aircraft wings [16]. In the remainder of the thesis, the contribution of the parasite drag is not considered.

3

Propeller-Wing Interaction Fundamentals

With the performance of the isolated propeller and wing covered, a closer look is taken at the interaction between the propeller and wing. It is known that the propeller and wing interact with each other, such that they influence each other's performance. To fully understand the performance of the propeller-wing system, both the effects of the wing on the propeller and vice versa are presented. As stated in Chapter 1, the thesis is focused on the tractor propeller-wing configuration, and therefore, only the interactions of this configuration are covered. In Section 3.1, the influence of the wing on the propeller is covered, whereafter the effects of the propeller slipstream on the wing are covered in Section 3.2. Finally, various studies in the literature on the aerodynamic performance of the propeller-wing system are discussed in Section 3.3.

3.1. Effects of the Wing on the Propeller

For a lift-producing wing, there is circulation in the flow. The phenomenon is explained in detail in Section 4.2. The circulation of the wing is seen by the velocities around the wing. In front of the wing, the velocity is in an upward direction, whereas the flow behind the wing is in a downward direction. In Figure 3.1, the bound circulation of the wing, Γ_b , is visualized in black. The induced velocities by the bound vortex are visualized in the same color. The upwash from the wing can be split into two velocity components. The vertical velocity component can be seen as an increase in the angle of attack of the propeller as shown in experiments by Heidelberg and Woodward [17]. The other velocity component induced by the wing is in the freestream direction. This velocity differs above and below the leading edge. Above the leading edge, an increase in velocity is present, and below the leading edge, a reduction of the velocity of the flow is present. The section of the propeller disk above the leading edge of the wing experiences an increase in incoming velocity with respect to the freestream velocity. It, therefore, generates less thrust compared to a similar isolated propeller. Below the leading edge, the opposite happens, resulting in an increased thrust on the lower side of the propeller. These variations in forces over the propeller disk area result in a nose-up pitching moment of the propeller. A similar force variation results when the sides of the propeller disk are compared. The up-rotating propeller blade moves with the wing-induced velocities, resulting in a higher local advance ratio than the propeller blade moving into the wing-induced velocities. As explained in the previous chapter, the local advance ratio is related to the local angle of attack of the propeller blade. From this change in angle of attack at the propeller blades on both sides of the propeller, a lower thrust is obtained at the section of the propeller disk where the propeller blade is moving up compared to the propeller blade that is moving down. Due to this variation in thrust over the sides of the propeller disk area, a yawing moment results in the direction of the up-going propeller blade [18]. Besides the upwash of the wing, the propeller is influenced by blockage of the flow by the wing. In front of the wing, the static and dynamic pressure are increased and decreased, respectively. This phenomenon leads to a decreased effective advance ratio such that the local blade angle of attack is increased. This increases the thrust and torque of the propeller compared to those of an isolated propeller [18]. In Figure 3.1, the blockage

effect is shown by the red velocity components. Furthermore, the wake of the wing tends to roll up, as is visualized with a blue color in Figure 3.1. These trailing vortices induce velocities in the direction as visualized in the figure at the location of the propeller disk in front of the wing. An inboard-down rotating propeller rotates with the velocities induced by the wake, and an inboard-up rotating propeller rotates into them. The propeller of the latter configuration has a higher effective advance ratio, increasing the aerodynamic forces of the propeller.

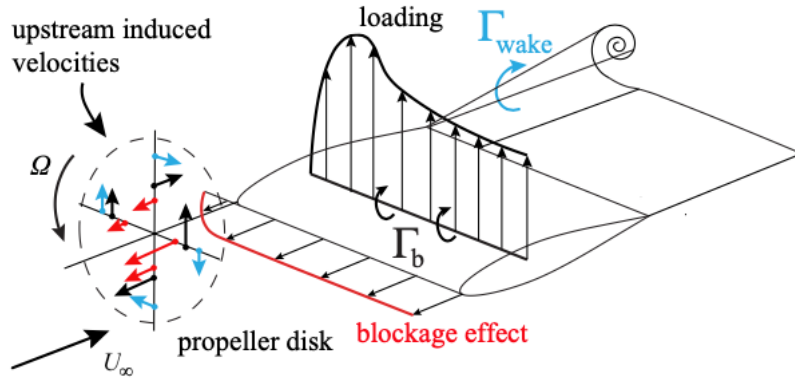


Figure 3.1: Schematic of the influence of the wing on the propeller [18].

The previously described effects of the wing on the propeller are dependent on the local performance of the wing. When the wing is producing more lift, for example, the increased induced velocities by the higher bound circulation increase their effect. Placing a propeller in front of a wing not only results in effects of the wing on the propeller, but the propeller also affects the performance of the wing. These influences on the performance are covered in the following section.

3.2. Effects of the Propeller on the Wing

For propeller-wing systems in tractor configuration, the wing is located in the slipstream of the propeller. The propeller-induced velocities influence the performance of the wing. In Section 3.2.1, the effects of the propeller slipstream on the lift distribution of the wing are analyzed. As discussed in the previous chapter, the shape of the lift distribution influences the lift-induced drag of the system. A more detailed explanation of the influence of the lift distribution on the lift-induced drag is provided in Section 3.2.2. Hereafter, the other force contributing to the induced drag of the wing, which is swirl recovery, is covered in Section 3.2.3.

3.2.1. Effects on the Lift Distribution

The lift distribution of the wing is affected by the velocities induced by the propeller. The slipstream influence on the wing lift distribution can be separated into two effects. First, the wing section behind the propeller experiences an increase in dynamic pressure as the propeller increases the axial velocity of the flow in the slipstream. The increase in dynamic pressure in the propeller slipstream increases the lift at the section of the wing behind the propeller. This separated effect is visualized in the spanwise lift distribution in Figure 3.2a. The lift distribution of the wing without the influence of the propeller is indicated by the dashed line. Second, the lift distribution of the wing is affected by the tangential velocities induced by the propeller. Upwash is induced by the propeller on the side of the propeller where the blades are moving up. This increases the local angle of attack at the wing section behind this side of the propeller. On the other side of the propeller disk, where the propeller blades are moving down, a decrease in the angle of attack is experienced by the local section of the wing. These changes in the angle of attack result in wing sections with an increase and decrease of the local lift compared to an isolated wing [19]. The change in lift distribution by the tangential induced velocities of the propeller is visualized in Figure 3.2b. The rotational direction of the propeller determines the shape of the lift distribution by this effect. For an inboard-up rotating propeller, the angle of attack is increased on the inboard side by the upwash of the propeller blade, and the angle of attack is decreased on the outboard side by the downwash of the down-going blade. The increase in dynamic pressure and change in attack angle is depended on the velocity profile within the slipstream of the propeller [1].

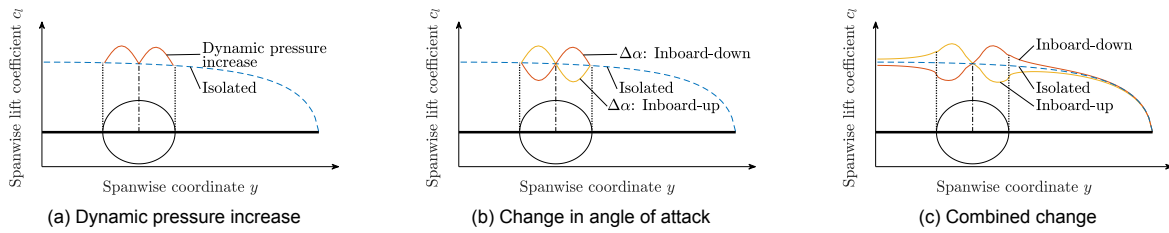


Figure 3.2: Decoupled and combined effects of the propeller slipstream on the spanwise lift distribution of the wing.

In reality, the changed lift distribution by the influence of the propeller slipstream is not an addition of the individual effects from the axial and tangential velocity components. In Figure 3.2c, a visualization of the lift distribution of a wing influenced by the propeller slipstream is shown. It can be noted that the lift is not only changed within the sections behind the propeller but also in the wing sections located beside the propeller slipstream. The change in lift distribution due to the propeller slipstream induces strong trailing vortices in the wake of the wing, which also influences the regions besides the propeller slipstream such that the spanwise lift distribution of the wing is changed [10]. As the vortices influence the lift distribution over the entire span of the wing, the sudden peaks in lift distribution are more spread out over the entire span of the wing [20]. These sudden changes in the lift distribution influence the span efficiency, which is further elaborated on in the next section.

3.2.2. Lift-Induced Drag of Propeller-Wing Systems

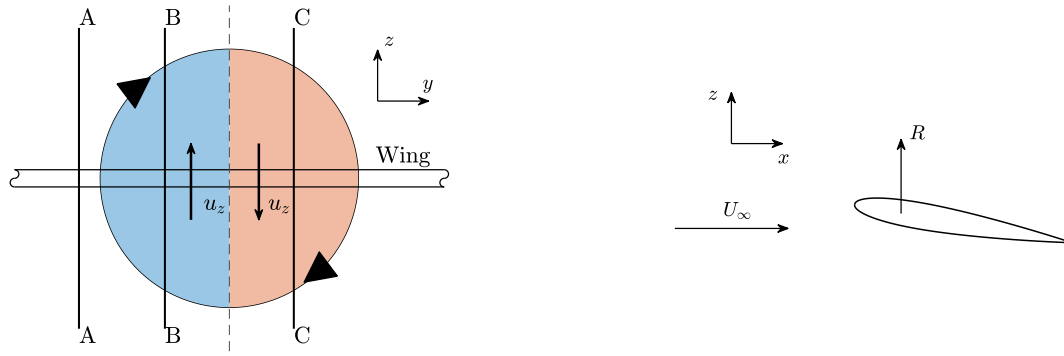
The lift-induced drag is directly related to the spanwise lift distribution of the wing, making the shape of the lift distribution important for evaluating the lift-induced drag of the wing. Equation 3.1 shows the relation between the lift-induced angle of attack, α_{li} , at spanwise position y_0 and the gradient of the spanwise circulation distribution, $d\Gamma/dy$, at spanwise position y . This equation is fundamental in Prandtl's classical lifting-line (LL) theory [12]. As explained in Section 2.2, the lift-induced angle of attack is related to the lift-induced drag of the wing. The circulation of the wing, Γ , is related to the lift of the wing as is explained in more detail in Section 4.2. In the previous section, it is shown that the lift distribution is affected by the propeller slipstream, therefore changing the lift-induced drag of the wing.

$$\alpha_{li}(y_0) = \frac{1}{4\pi U_\infty} \int_{-b/2}^{b/2} \frac{(d\Gamma/dy) dy}{y_0 - y} \quad (3.1)$$

Sinnige et al. [21] emphasized the importance of the spanwise location of the propeller through an experimental study on propeller-wing systems. Aerodynamic interactions between the propeller and wing change the effective span efficiency parameter of the wing. It is shown that, besides providing thrust, the propeller can effectively reduce drag through the aerodynamic interaction between the propeller and wing. The reduction of drag is obtained by the contribution of swirl recovery, which is elaborated on in the next section.

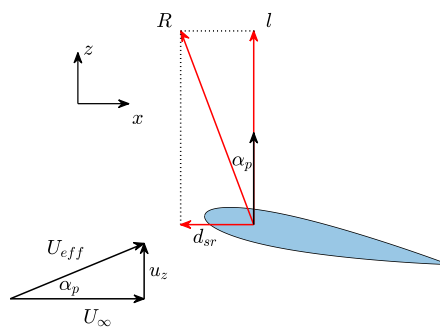
3.2.3. Swirl Recovery of a Wing with Infinite Span

The angular momentum, or swirl, in the wake of the propeller slipstream, is considered a loss in energy as it does not contribute to the thrust production of the propeller. The wing behind the propeller can recover some of this energy by generating an extra thrust component. The force is explained by the schematic visualization of a propeller located in front of a wing with an infinite span such that the lift-induced drag of the wing can be neglected, as seen in Figure 3.3. Over the span of the wing, three different cross-sections are indicated. The left side of the propeller, where the blades are moving up, is shown in blue, and the right side, where the blades are moving down, is shown in red. The propeller is not influenced by the wing-induced velocities, such that the direction of the tangential velocity vectors is equal in magnitude and in opposite directions of each other on both sides of the propeller. The locations of the three different cross-sections are indicated with A-A, B-B, and C-C. As the wing has an infinite span, downwash induced by the wing, resulting in the lift-induced drag, is left out of consideration such that only the freestream and propeller-induced velocities remain.

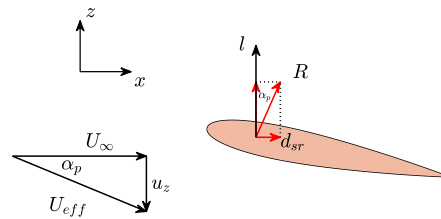


(a) Front view of the propeller. The up-rotating propeller blades are on the blue (left) side and the down-rotating propeller blades are on the red (right) side.

(b) Section A-A outside of the propeller slipstream.



(c) Section B-B behind the up-rotating propeller blades.



(d) Section C-C behind the down-rotating propeller blades.

Figure 3.3: Schematic visualization a propeller located in front of a wing with infinite span.

Without the downwash from the wing, only the resultant force vector remains when a section of the wing is considered outside of the propeller slipstream. This section is visualized in Figure 3.3b. In Figure 3.3c, section B-B is visualized, where the up-rotating propeller blades induce a positive vertical velocity. The angle of attack of the airfoil section increases by α_p , such that the magnitude of the resultant vector of the airfoil section increases and rotates forward. The swirl recovery is seen when the resultant vector of the airfoil section is decomposed into drag and lift, which remains in the direction of flight and perpendicular to that by definition. On the other side of the propeller, section C-C is considered. This section is visualized in Figure 3.3d. Here, the down-rotating propeller blades induce a negative vertical velocity. Within this side of the propeller slipstream, the local angle of attack is reduced by α_p . By this reduction, the magnitude of the resultant force vector of the airfoil reduces, and it rotates backward. By decomposing the resultant force into lift and drag at this section, two things are noted. First, it is seen that the lift and drag of the wing are both smaller compared to those from the airfoil at section B-B. Second, it is seen that the contribution of the local swirl recovery to the total drag of the wing is negative. When a drag balance of the wing is considered, swirl recovery is present at the wing on both sides of the propeller, but as the resultant force is larger behind the up-rotating propeller side due to the increase in the local angle of attack compared to the down-rotating side, a net thrust force results into the direction of flight which is considered as swirl recovery by the wing. Additionally, assuming that the spanwise lift distribution is constant, such that the gradient of the spanwise lift distribution is zero, the net positive swirl recovery from the wing is independent of the rotational direction of the propeller. This follows from the fact that the difference in magnitude of the resultant force of the wing sections behind the two propellers is the same for both rotational directions of the propeller.

3.3. Literature on Propeller-Wing Systems

Many numerical and experimental studies have been conducted for research on propeller-wing systems. In this section, the findings of various relevant studies are highlighted. At the end of the section, the conclusions of the studies will be summarized, such that the relevance of the research within thesis will become clear.

Veldhuis [9] has investigated the influence of propeller-wing system geometry parameters on the performance of the system. Due to the contraction of the slipstream, the streamwise propeller position with respect to the wing is found to be influential on the performance. A propeller position where the propeller is located close to and below the leading edge of the wing results in a negative effect on the performance of the wing as a negative angle of attack decreases the lift of the wing. Furthermore, the vertical position of the propeller with respect to the wing is investigated. The vertical placement of the propeller could lead to a change in the angle of attack of the wing by the contraction of the slipstream. Considerably the most investigated geometrical parameter of the propeller-wing system is the spanwise position of the propeller with respect to the wing. Various studies have shown the lift augmentation, and drag reduction of the system when the propeller with inboard-up rotational direction is placed closer to the tip of the wing [9, 19, 22]. Figure 3.4 shows the lift and drag coefficients of a propeller-wing system for various spanwise positions of the propeller resulting from a wind tunnel experiment from Veldhuis [9]. A substantial increase in lift and decrease in drag results from the propeller positions near the tip of the wing compared to the positions near the root of the wing.

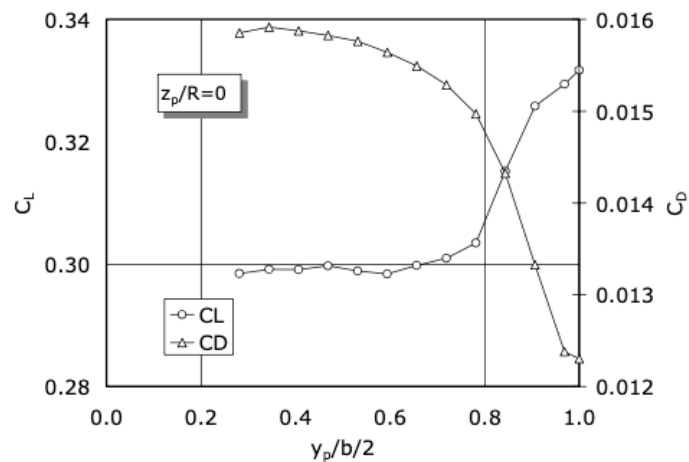


Figure 3.4: Effect of the spanwise propeller position, y_p . The relevant system parameters of the APROPOS propeller-wing system are $J = 0.92$, $c_T = 0.127$, $\alpha_p = 0$ degree, and $\alpha = 4.2$ degrees [9].

Snyder and Zumwalt [7] also investigated the aerodynamic performance of propeller-wing systems through a wind tunnel experiment. The same results were found by keeping all parameters unaltered, except for the spanwise position and rotational direction of the propeller. An increase in the aerodynamic efficiency of the wing results from a decrease in the induced drag of the wing. It was also shown that the benefits of the inboard-up rotating propeller, which is counter-rotating the wingtip vortex, are more significant compared to those of the inboard-down rotating propeller.

In a numerical study from Miranda and Brennan [22], similar conclusions to those of the previous studies were made. The influence of the isolated wing lift distribution is examined. The performance of the propeller-wing system is increased when more load is present near the tip of the wing. The elliptical lift distribution results in the lowest lift-induced drag when the wing is isolated from the propeller. Including propeller-induced velocities change the optimum spanwise wing lift distribution as is visualized in Figure 3.5.

The spanwise position of the propeller was also investigated in an experimental study by Sinnige et al. [21]. A conventional propeller position, which is located closer to the center of the wing, is compared to a wingtip-mounted propeller. A drag reduction of 5-15% was obtained by the wingtip-mounted propeller

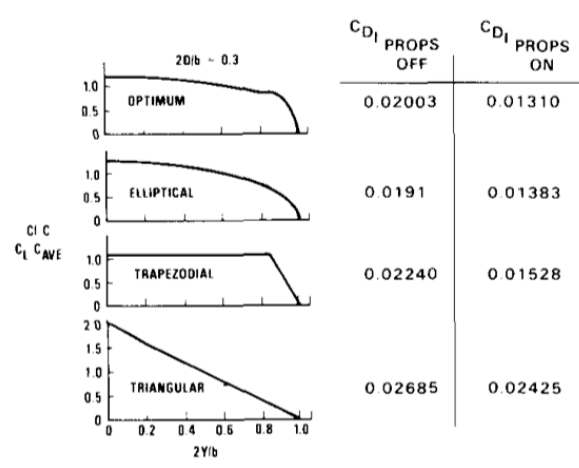


Figure 3.5: Effect of the spanwise lift distribution on the induced drag of the wing [22].

relative to the conventional configuration. Important to note is that the lift coefficient of the system was fixed at 0.5, which is important as the lift is also changed by the location of the propeller position as was shown by previously discussed studies. The strength of the wingtip vortex increases with the increase of the lift coefficient. It was found that by the increase of the system lift coefficient to 0.7, a reduction of 25-50% is obtained by the wingtip-mounted configuration compared to the conventional configuration.

Cole et al. [23] conducted a recent study on the aerodynamic interactions of the propeller-wing system. The results from this numerical study are diametrically opposed to those from previous studies. A specific case showed that an inboard-down rotating propeller located at about 30% of the span from the root of the wing, above the leading edge, results in the best performance of the system. The majority of the benefit results from a reduced induced drag on the wing section within the propeller slipstream.

Most of the previously discussed studies have shown the benefits of placing the propeller, rotating inboard-up, towards the tip of the wing. By this placement of the propeller, the induced drag of the system decreases, and the lift increases. From previous sections, it is seen that the induced drag consists of two components: lift-induced drag and swirl recovery. None of these studies decouple the induced drag to investigate the separate influence and relation of these induced drag contributors. In the following chapter, various approaches to analyzing propeller-wing system configurations are discussed such that a numerical model can be constructed to investigate the individual contributions of the lift-induced drag and swirl recovery to the induced drag of the wing.

4

Modeling of Propeller-Wing Systems

The most important phenomena of the isolated propeller, wing, and propeller-wing systems are discussed in previous chapters. To be able to conduct new research on the propeller-wing system, such that the answers can be found to the research questions, a numerical model should be developed. In this chapter, the design approach and choices of the numerical model are elaborated on. First, the definition of interaction modes of numerical models for propeller-wing systems is explained in Section 4.1. Secondly, the fundamentals of the potential flow theory are covered in Section 4.2 as many models from previous studies rely on the theory. Hereafter, the models from previous studies on propeller-wing systems are discussed in Section 4.3. Finally, in Section 4.4, a reasoning behind the used modules within the model is provided, and an overview of the model is given.

4.1. Interaction Modes

The previous chapter explained the various interaction effects between the propeller and wing. From the experiment conducted by Sinnige et al. [21], it is concluded that the influence of the wing on the propeller is limited. Comparing the loading of the isolated propeller with the loading of the propeller integrated into the propeller-wing system, an increase of about 2% is seen in the presence of the wing. It has to be noted that during this experiment, the propeller was located in front of the tip of a tailplane. When the propeller is placed in front of a full wing, higher circulations could increase the effects on the propeller performance. Ebbens [24] quantified the coupling between the propeller and wing with a numerical model based on the potential flow theory. In this study, although the influence of the wing on the propeller remains small, it is concluded that the full interaction between the propeller and wing has a non-negligible effect on the system performance. Such a model, where the performance of the wing influences the propeller, is denoted as a full interaction mode (FIM) [20]. This model characteristic is essential when the whole system performance is required, which is the case in optimization studies of propeller-wing systems or when the interest of the study lies with the performance of the propeller. The numerical model relies on a single interaction mode (SIM) when the performance of the wing does not influence the propeller performance. In various studies presented in Section 3.3 effect of the wing on the propeller was left out of consideration, making the numerical models rely on a SIM. In the study by Cole et al. [23], however, the numerical model relying on a FIM was used to reach a thrust equilibrium of the propeller-wing system.

The emphasis of this thesis is the understanding of the relative contribution of the lift-induced drag and swirl recovery of the wing by the influence of the propeller-induced velocities. For this understanding, there is no interest in the performance of the propeller by the influence of the wing. For this reason, a numerical model in which the performance of the wing does not influence the propeller performance will suffice to make it rely on a SIM.

4.2. Potential Flow Theory

Many numerical models used in research on propeller-wing systems are based on the potential flow theory. Before various models from the literature are discussed, a closer look at the relevance and

assumptions of the potential flow is taken in Section 4.2.1. To better understand why this theory should be used in the analysis of propeller-wing systems, the limitations and drawbacks of the theory are shortly presented in Section 4.2.2.

4.2.1. Relevance & Assumptions

The complexity of the equations describing aerodynamic flows reduces significantly with the assumptions of the potential flow theory compared to methods such as computational fluid dynamics (CFD). Besides the relatively low computational cost for potential flow solvers compared to CFD, it also makes it easier to study the fundamentals of the aerodynamic phenomena of propeller-wing systems. The decoupling and influence of the flow interaction phenomena, as described in Chapter 3, can be relatively simply obtained by numerical models relying on the potential flow theory compared to CFD and experiments. Therefore, the potential flow theory is often used at an academic level [11, 12].

In the potential flow theory, the velocity field is described by the gradient of a scalar function which is the velocity potential. A potential flow is an idealized model of the actual flow by assuming the flow to be inviscid and irrotational. The viscous effects of the flow are mainly limited to the boundary layer [12]. The assumption that the flow is irrotational is related to the first assumption, as the viscosity induces turbulence in the fluid. Assuming an irrotational flow simplifies the complexity of the modeling equations significantly. Another advantage of the theory is the fact that the principle of superposition can add individual potential flow elements. The assumptions used by the potential flow theory also bring limitations to the models that rely on it, which will be further discussed in the next section.

As is described in Section 2.2, lift by a wing is obtained by a pressure difference over the upper and lower surfaces. In the potential flow theory, this pressure difference can be represented by circulation. A vortex is the flow element within potential flow representing the circulation, and it can induce velocities to mimic the flow around the wing. The relation between the vortex strength and lift produced by an airfoil section can be seen in Equation 4.1. This is also known as the Kutta-Joukowski theorem and is a very powerful relation in theoretical aerodynamics [12].

$$l = \rho_{\infty} U_{\infty} \Gamma \quad (4.1)$$

4.2.2. Limitations

The assumptions on which the potential flow theory relies also have a downside. A non-lifting body in a potential flow does not experience any drag, also known as d'Alembert's Paradox [25]. In the potential flow theory, the boundary layer is not present as the viscosity of the flow is left out, which results in the lack of flow separation. With the potential flow theory, it is only possible to obtain relevant solutions to the aerodynamic problem at small angles of attack such that flow separation does not dominate the solution of the problem [19]. Even at small angles of attack, the results obtained with models relying on the potential flow theory should be analyzed critically to be aware of what the influence of the viscous effects would be in the real flow problem.

4.3. Propeller-Wing System Analysis Methods

In literature, many analysis methods have been used to perform research on propeller-wing systems. Several models are an integration of a propeller and wing model. The individual models based on the potential flow theory are presented in Section 4.3.1. Hereafter, in Section 4.3.2, the integration of these models is discussed and other analysis methods, which are not based on the potential flow theory, are presented.

4.3.1. Numerical Propeller & Wing Models

Various approaches are taken to include the propeller analysis of the propeller-wing model. Three different modeling approaches based on the potential flow are considered for modeling the propeller. The actuator disk (AD) theory is the most straightforward method. An infinitely thin disk can replace the propeller in a one-dimensional and axisymmetric stream tube [26]. The classical AD only includes a uniform axial velocity within the propeller slipstream. This is a disadvantage as the swirl in the propeller slipstream is an important characteristic influencing the performance of the wing. Another method for

modeling the propeller is the blade element momentum (BEM) method, which relies on the momentum theory and the blade element theory [26]. This method can determine both propeller performance characteristics and propeller-induced velocities. From this method, axial and tangential induction factors can be obtained for each radial position such that the axial and tangential velocity profiles of the propeller result. The slipstream tube model can follow the BEM method to obtain the propeller-induced velocities in the slipstream. The BEM method obtains the radial circulation distribution from the propeller, which the slipstream tube model then uses to calculate the propeller-induced velocities in and outside the slipstream [9, 22].

Two methods based on the potential flow theory, which are often used for modeling wings, are highlighted from literature. The first method is Prandtl's classical lifting-line (LL) theory, where the lift and lift-induced drag are obtained from a sectional analysis. The theory assumes a straight-bound vortex representing the lifting surface, and the wake behind the surface is represented by trailing vortices [11]. The downside of the LL theory is the lack of variation in the wing planform characteristics, such as the taper ratio. The vortex lattice method (VLM) is similar to the LL theory, where multiple lifting lines can be used to model more complex wing shapes. In this method, the wing is divided into panels containing its lifting line with trailing vortices. The VLM can vary in complexity, which is further elaborated in the next section.

4.3.2. Propeller-Wing System Models

The models of the previous section that can be used to model the isolated propeller or wing can be integrated to model a full propeller-wing system. In these models, the wing model uses the propeller-induced velocities to evaluate the performance. When the propeller model does not use the wing-induced velocities, the model is based on a SIM.

Fixed and free-wake models are used to model isolated propellers and wings. The wake of the VLM from the previous section can be prescribed to increase the accuracy of the model. These methods increase the computational expense of the numerical model. Especially free-wake solutions are computationally expensive as iterations are needed to obtain the shape of the wake [11]. The fixed and free-wake models can also be used to model propeller-wing systems, as the propeller and wing influence each other's wake. Furthermore, the results of these methods are time-dependent and, therefore, often need additional computations to obtain a steady-state solution, dependent on the analysis [10]. Cole [27] has developed a higher-order free-wake (HOFW) model for the aerodynamic performance prediction of propeller-wing systems. It is argued that the computational time does not become too expensive by using distributed vorticity elements [28]. The HOFW method is a time-dependent analysis method, which, for most analysis, need additional computations to obtain a steady-state solution. The main advantage of the method is the better inclusion of the interactions between propeller and wing compared to low-fidelity methods such as with VLMs [29]. These detailed interactions can be important for optimization studies and studies where a detailed performance of the propeller-system is required but does not have to be included in the numerical model of this research as this does not contribute to the understanding of the fundamental contribution of the lift-induced drag and swirl recovery to the induced drag of the wing.

CFD or wind tunnel experiments can be used for a more detailed analysis of propeller-wing systems and do not rely on the potential flow theory. The accuracy of the outcome of these analysis methods could be an advantage in the analysis of propeller-wing systems. The high computational expense that comes with CFD can be considered one of the disadvantages. Another disadvantage could be the detailed results from these analysis methods. Decoupling the effects of system parameters on the system performance could be more complicated, if not impossible.

4.4. Modeling Approach

From the research aim, it can be determined that the model must be capable of decoupling the lift-induced drag and swirl recovery of the propeller-wing system. Furthermore, the model must be capable of evaluating multiple system configurations. As the evaluation of many configurations is necessary for the research, CFD and experimental research are unsuitable for the analysis of this thesis. The HOFW

method is suitable for analyzing the interaction between the propeller and wing, as has been shown by Cole [27]. The method becomes more relevant as the method is a FIM. However, the amount of details that can be obtained on the performance and the interaction between the propeller and wing from the HOFW model is not needed during the analysis of this thesis. This also leaves other free-wake analysis methods out of consideration. Within the research, various propeller-wing system configurations have to be examined. For this reason, the computational cost of the numerical model should be low, which is not the case for the analysis mentioned above methods.

Willemsen [19] and Ebbens [24] used the VLM, with horseshoe and ring vortex elements, respectively, to analyze the propeller-wing systems. Both models used an iterative method to include the influence of the wing on the propeller, making them a FIM. A FIM, however, is not needed to be able to analyze and understand the relative coupling between the lift-induced drag and swirl recovery of the propeller-wing system. A numerical model with a FIM would better suit models which are to be used to find optimal propeller-wing system configurations.

As multiple analysis methods have been considered, a modeling approach can be chosen. As argued previously, the numerical model can be a SIM. Figure 4.1 shows a schematic overview of the numerical model that will be developed. The model consists of two integrated models: the propeller and the wing model. A BEM method is used in the propeller model to analyze a specific propeller operating point. The different operating points of the propeller result in different propeller slipstream velocity profiles. Subsequently, the results from the BEM method can be used by the slipstream tube model, such that the propeller-induced velocities can be obtained. The wing model consists of a VLM, which is adapted to take the propeller-induced velocities from the propeller model into account. The VLM can be used to obtain the most relevant parameters of the wing for this study, which are lift, lift-induced drag, and swirl recovery. As seen from the flow chart of the model, there is no information going from the wing to the propeller model, making the model a SIM. An essential advantage of the model is that for the analysis of various propeller positions, no iterations are needed to obtain a new propeller performance due to the influence of the wing. This decreases the computational expense of the model significantly compared to the models based on a FIM. With the global overview of the model presented, the details of the model can be elaborated on in the next part of the thesis.

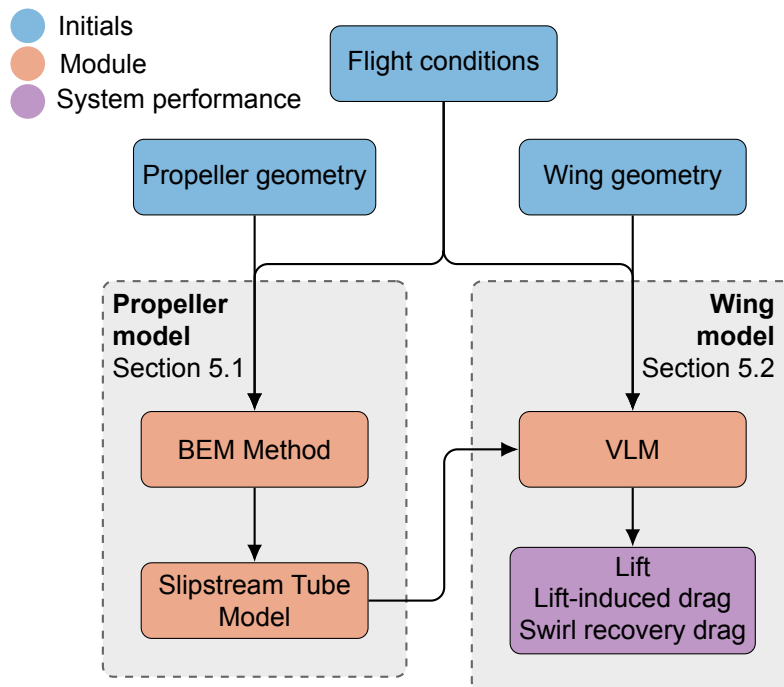


Figure 4.1: Global overview of the numerical model.



Numerical Model & Validation

The second part of the thesis focuses on the development of the numerical model and its validation. First, in Chapter 5 the modeling of the propeller and wing is covered. An additional explanation is provided on the integration of the propeller and wing models. Second, the validation of the numerical model is conducted in parts. The isolated propeller and wing model are validated separately, whereafter, the system is validated with wind tunnel data from experimental research.

5

Numerical Model of the Propeller-Wing System

The numerical model consists of two separate models integrated to model the propeller-wing model. First, the propeller model is covered in Section 5.1. The propeller-induced velocities obtained with the propeller model are forwarded to the wing model, elaborated on in Section 5.2. Before the numerical model is validated, final notes are made on the integration between the propeller and wing model in Section 5.3.

5.1. Propeller Model

The propeller model consists of the BEM method and the slipstream tube model, which are covered in detail in Sections 5.1.1 and 5.1.2. The axial velocity of the propeller is averaged before passing through to the wing model, which is explained in Section 5.1.3. A flow chart of the propeller model with relevant modules and variables is shown in Figure 5.1.

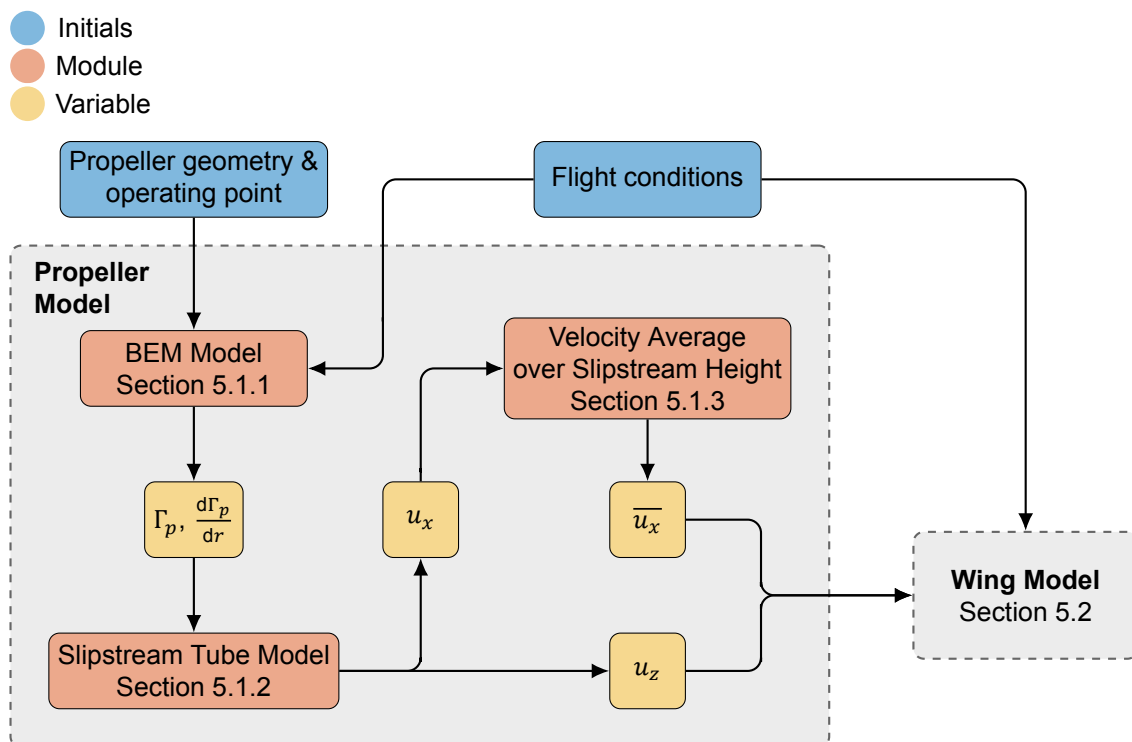


Figure 5.1: Overview of the numerical model with details of the propeller model.

5.1.1. BEM Model

With the blade element momentum (BEM) method, the circulation distribution over the radial positions of the propeller can be obtained for different operating conditions. The propeller blades are divided into a finite number of elements. An iterative process is used to obtain the circulation at each radial element of the propeller blades. The BEM model from Drela [30] is used to formulate the BEM method in the numerical model. This formulation is also used for existing codes, widely used for the analysis and design of propellers and rotors, such as XROTOR, QPROP, and QMIL [31].

First, the propeller blades are discretized into a finite number of radial sections. For each radial section, the axial and tangential velocities are presented in Equation 5.1, which include the self-induced velocities of the propeller, u_a , and u_t . Ω and r represent the rotational speed and radial position of the radial segment of the propeller, respectively. To decrease the computational expense of the BEM model, a dummy variable, Ψ , is introduced, which is the angle from the center of the total inflow velocity with the total inflow velocity as seen in Figure 5.2. The local velocities at the location of the radial section, W_a and W_t , are functions of the dummy variable as seen in Equation 5.2. The velocities are located in the circle, showing the assumption in this solution method: the induced velocity is perpendicular to the total velocity. This is only valid for lightly loaded propellers with Goldstein's circulation distribution [30].

$$\begin{aligned} U_a &= V + u_a \\ U_t &= \Omega r - u_t \end{aligned} \quad (5.1)$$

$$\begin{aligned} W_a(\Psi) &= \frac{1}{2}U_a + \frac{1}{2}U \sin(\Psi) \\ W_t(\Psi) &= \frac{1}{2}U_t + \frac{1}{2}U \cos(\Psi) \\ v_t(\Psi) &= U_t - W_t \end{aligned} \quad (5.2)$$

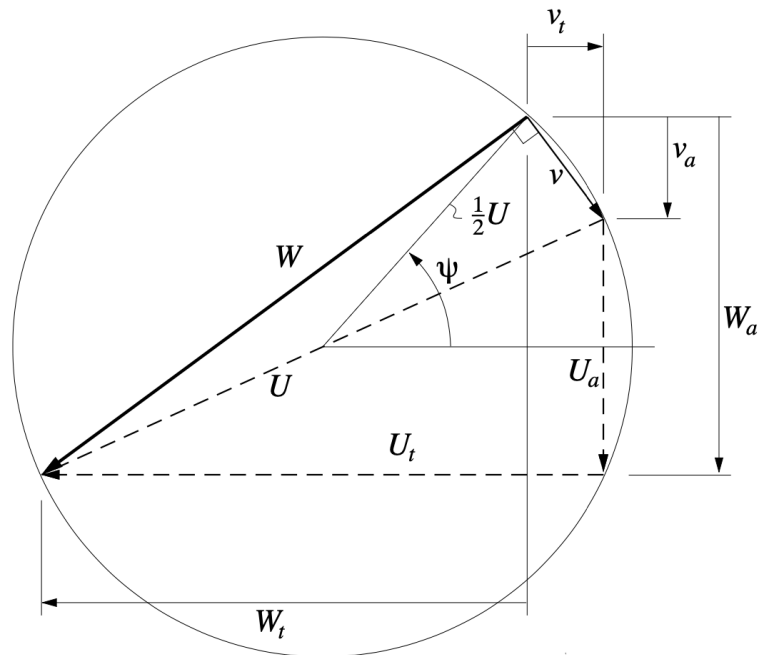


Figure 5.2: Velocity parametrization from the BEM including the dummy variable Ψ [30].

The tangential velocity, v_t , is obtained by combining the two theories on which the BEM method relies. The first method, based on the momentum theory, is associated with the torque imparted by the rotor. From this theory, Equation 5.3 follows, where λ_w is the local advance ratio. A tip correction factor, F ,

is applied because the pressure difference over the propeller blade results in air flow over the blade tip from the higher to the lower pressure side. This effectively reduces the resulting forces near the tip, which is not taken into account by the two-dimensional analysis of the BEM method. The other method, based on the blade element theory, follows from the relation of Helmholtz's Theorem and is seen in Equation 5.4. In this equation, the sectional lift coefficient of the propeller section, c_l , can be obtained from experiments and depends on the local angle of attack, α , and Reynolds number, Re . Furthermore, the Prandtl-Glauert correction, seen in Equation 5.5, is applied to take the compressibility of the fluid into account. The lift coefficient for an incompressible fluid, $c_{l,0}$, is corrected with the freestream Mach number, M_∞ [12].

$$\Gamma_p(\Psi) = v_t \frac{4\pi r}{B} F \sqrt{1 + \left(\frac{4\lambda_w R}{\pi B r} \right)^2} \quad (5.3)$$

$$\Gamma_p(\Psi) = \frac{1}{2} W c c_l(\alpha, Re) \frac{1}{\sqrt{1 - M^2}} \quad (5.4)$$

$$c_l = \frac{c_{l,0}}{\sqrt{1 - M_\infty^2}} \quad (5.5)$$

The Newton–Raphson method is used for the iterative procedure to obtain the local bound circulation. Equation 5.6 shows the iterative procedure, where $\Delta\Gamma_p$ represents the difference between the two circulations found with Equations 5.3 and 5.4. To numerically obtain the gradient in the denominator, $d\Psi$ is set to ± 0.005 radians. This iteration scheme is repeated until the desired residual between the circulations of the equations is obtained.

$$\Psi_{\text{new}} = \Psi_{\text{old}} - \frac{\Delta\Gamma_p}{d(\Delta\Gamma_p)/d\psi} \quad (5.6)$$

5.1.2. Slipstream Tube Model

Continuous vortex sheets can replace the helicoid vortex sheet in the propeller slipstream. This replacement results in a time-averaged solution of the propeller slipstream. The slipstream tube model consists of these continuous vortex sheets and is first introduced by Miranda and Brennan [22]. An advantage of the model is the possibility to obtain the propeller-induced velocities at any point in or outside the slipstream. Figure 5.3 shows a schematic visualization of the slipstream tube model, where a finite number of tubes are located within each other with the x -axis as their common longitudinal axis. The velocities are induced by three components of the slipstream tube model: The bound vorticity at the propeller disk, the axial vorticity, and the tangential vorticity.

For each radial section of the propeller, the bound vortex, Γ_p , which follows from the BEM method, is distributed over the circumference of the bound vortex of the slipstream tube. The strength of the individual vorticity elements is given by Equation 5.7. The vorticity of the bound vortex is shed into the wake by the axial and tangential vortex sheets. The amount of vorticity shed into the wake depends on the difference between the strength of the bound vorticity of the radial elements of the propeller, $d\Gamma_p/dr$. The strength of the distributed axial and tangential vorticity elements, defined as γ_t and γ_a , are presented in Equations 5.8 and 5.9, respectively. The equations for the induced velocities by the bound vortex and axial and tangential vorticity sheets from the slipstream tube can be found in Appendix D in the work from Veldhuis [9]. The equations are obtained after integrating the original equations over the streamwise direction.

$$\gamma_p = \frac{B}{2\pi r} \Gamma_p \quad (5.7)$$

$$\gamma_t = \frac{n B}{U_\infty} \frac{d\Gamma_p}{dr} \quad (5.8)$$

$$\gamma_a = \frac{B}{2\pi r} \frac{d\Gamma_p}{dr} \quad (5.9)$$

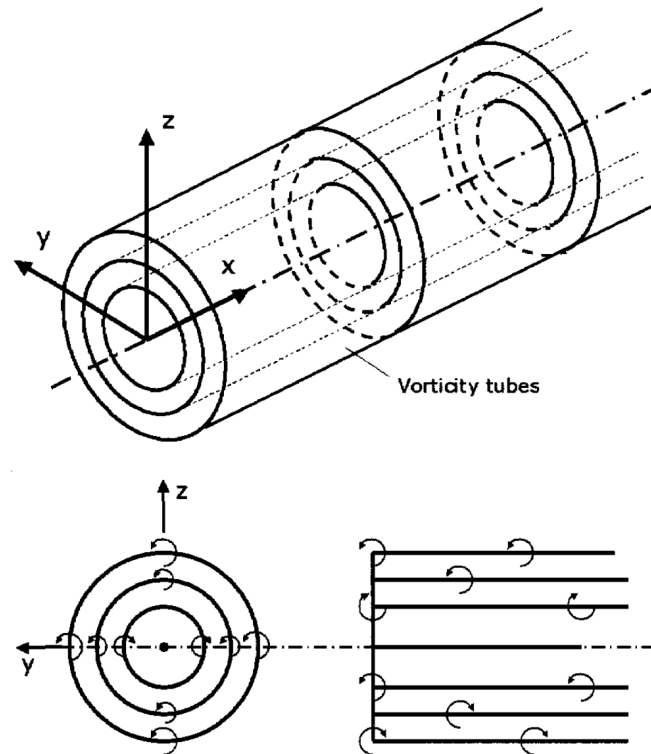


Figure 5.3: Visualization of the slipstream tube model [9].

Important to note is that singularities can arise when the evaluation of the velocities is chosen too close to the vortex sheets control points of the tube. The velocities of the propeller at the location of the wing are evaluated precisely in between the vortex sheets of the slipstream tube model, such that singularities are avoided. This essentially is the discretization of the outer integral of the velocities induced by the bound vortex of the model. The number of radial sections could be increased when the bound circulation distribution of the propeller blades from the BEM method is interpolated between the radial sections. The amount of radial sections used in the BEM model is 23.

5.1.3. Axial Velocity Averaging

When a wing is placed within the slipstream of the propeller, the velocities can be evaluated directly over the span of the wing at the control points of the wing. For a wing without dihedral, the control points are located at $z = 0$. The propeller performance is evaluated by means of the BEM method of the propeller used in the experiment by Sinnige et al. [21] at $x/R = 0.8530$, where the advance ratio and blade pitch at 75% of the radius are 0.9 and 30 degrees, respectively. Behind the center of the propeller, the induced velocities obtained with the slipstream tube model are only slightly higher than the freestream velocity. When the propeller-induced velocities are calculated for a trailing wing surface by the slipstream tube model, the axial velocity increase is minimal near the propeller center as seen in Figure 5.4 with the blue line. However, when only looking at one horizontal position, the increase in axial velocity when moving up or down from the center is ignored. This increase in dynamic pressure above and below the horizontal center does influence the lift of the trailing surface [32]. Therefore, the propeller axial radial velocity distribution at each spanwise station is averaged in the vertical sense.

For each vertical strip in the spanwise direction of the wing, i , the axial velocity is evaluated for j elements over the height of the slipstream domain. The amount of elements is proportional to the local height of the slipstream. This is schematically visualized in Figure 5.5. The velocities of the elements within the strip are multiplied by their area, and whereafter, the elements are summed for strip i . The average velocity, $\overline{u_{x_i}}$, is obtained by dividing the summation by the area of the whole strip. The previously mentioned direct obtained velocity from the slipstream tube model over the span of the

wing has been averaged by the explained method and is also shown in Figure 5.4 and indicated by the red line. The averaging of the velocity over the slipstream height results in an increase in axial velocity around the center of the propeller and a reduction near the boundary of the propeller.

$$\overline{u_{x_i}} = \frac{\sum_1^j u_{x_{i,j}} \Delta y}{j \Delta z} \quad (5.10)$$

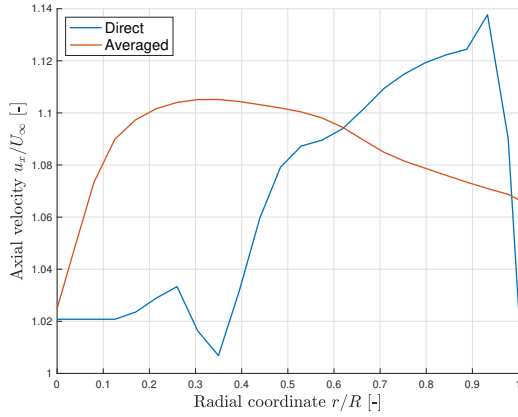


Figure 5.4: Direct and averaged axial propeller-induced velocities with an advance ratio of 0.8 at $x = 1.52R$.

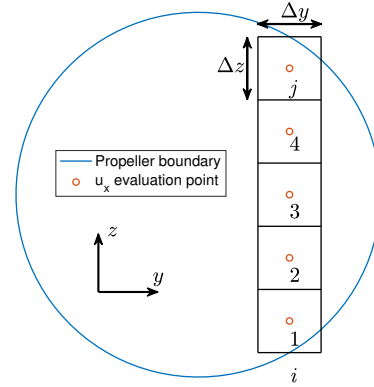
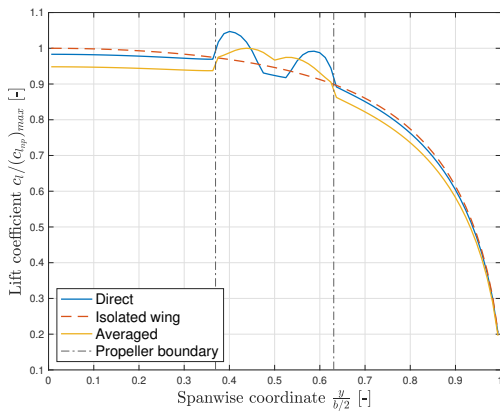
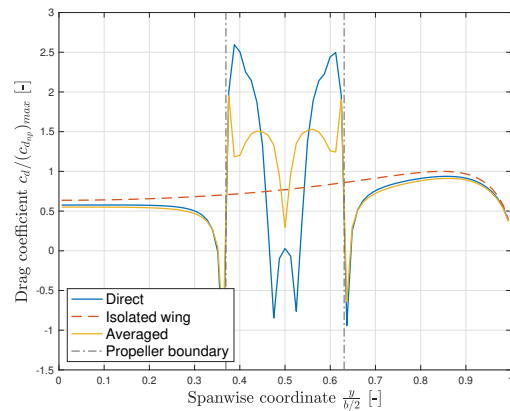


Figure 5.5: Schematic of radial strip i for averaging the axial velocity over the height of the propeller.

Figure 5.6 shows the effect of the averaging of the axial velocity on the lift and drag distributions of a wing with a lift coefficient of 0.35. It is seen that the lift increase near the propeller boundaries is smaller with the direct axial velocity from the slipstream tube model compared to that obtained with the averaged axial velocity. With the averaged axial velocity, the lift is further increased behind the center of the propeller. The spanwise shape of the lift-induced drag changes such that the distribution is also more gradual. In this example, the lift-induced drag of the wing slightly decreases by 0.8% by averaging the axial velocity over the height of the propeller slipstream.



(a) Spanwise lift distributions



(b) Spanwise drag distributions

Figure 5.6: Spanwise coefficients for the direct and averaged axial velocities of a propeller at OP 1 at $y_p = 0.5b/2$ with radius $r_p = 0.13b/2$.

The same averaging of the tangential velocities is investigated. However, it is decided not to use the averaging of the tangential velocities over the height of the slipstream domain. A detailed explanation of this method and the effects following from a possible averaging of the tangential velocities is provided in Appendix C.

5.2. Wing Model

The wing model consists of multiple modules. First, the VLM with horseshoe vortex elements is formulated in Section 5.2.1. This method uses a correction matrix for the finite size of the propeller slipstream, which is covered in Section 5.2.2. Hereafter, a detailed description of how the lift-induced drag and swirl recovery of the wing are obtained is provided in Sections 5.2.3 and 5.2.4. The relations between the various modules with relevant parameters are visualized in Figure 5.7.

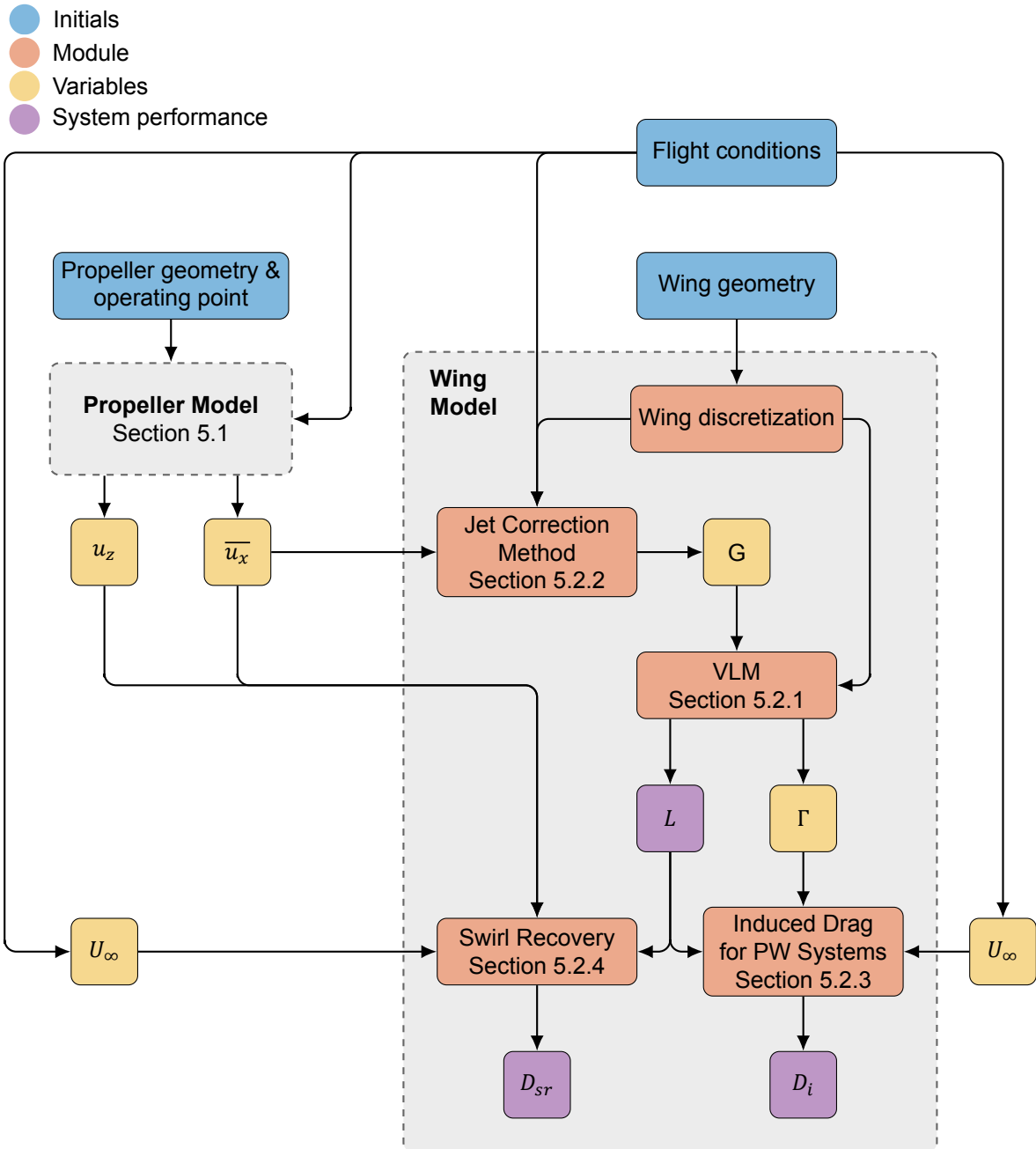


Figure 5.7: Overview of the numerical model with details of the wing model.

5.2.1. VLM Formulation for Propeller-Wing Systems

The VLM used in this thesis, is a modified version of the one presented by Katz and Plotkin [11] such that the propeller-induced velocities are taken into account. In Figure 5.8, a schematic top view of the VLM is shown. In the numerical model, the wing has one panel in the chordwise direction of the wing as this has been proven sufficient for the accuracy of the model [33]. Ten panels are visualized in the spanwise direction of the wing, but during the analyses this number can be increased to any n number of panels. All of the panels are located within the xz -plane. Each of the panels contains a horseshoe vortex with a bound vortex with strength Γ at its quarter-chord line and trailing vortices with the same strength over the side of the panel extending toward infinity. A control point is located on the spanwise center of each panel at the three-quarter chord line. A single panel with a corresponding horseshoe vortex is visualized in Figure 5.9. In this figure, the relevant dimensions of the panel are indicated. Again, the bound vortex and control points are visualized at $c/4$ and $3c/4$ from the leading edge of the panel, respectively. Furthermore, the span of the panel is denoted by Δb . At the control point, the normal vector, \mathbf{n} , is visualized, which is dependent on the slope of the camber line at that chordwise location, $\partial g/\partial x$, the local wing twist, and geometric angle of attack of the wing.

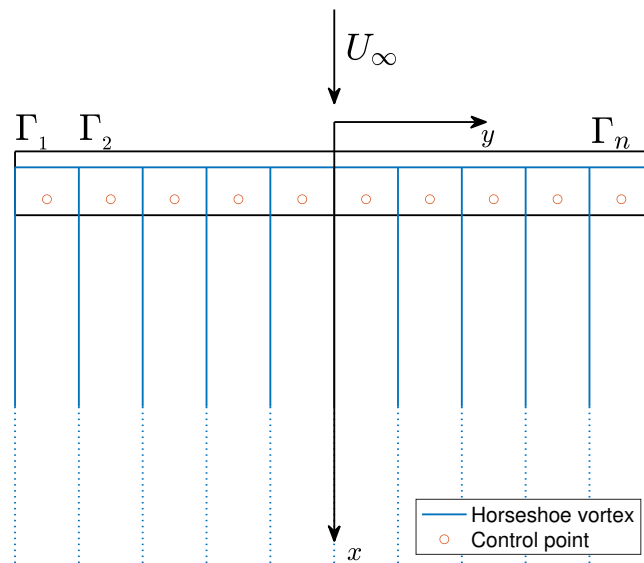


Figure 5.8: Top view of the VLM with horseshoe vortices.

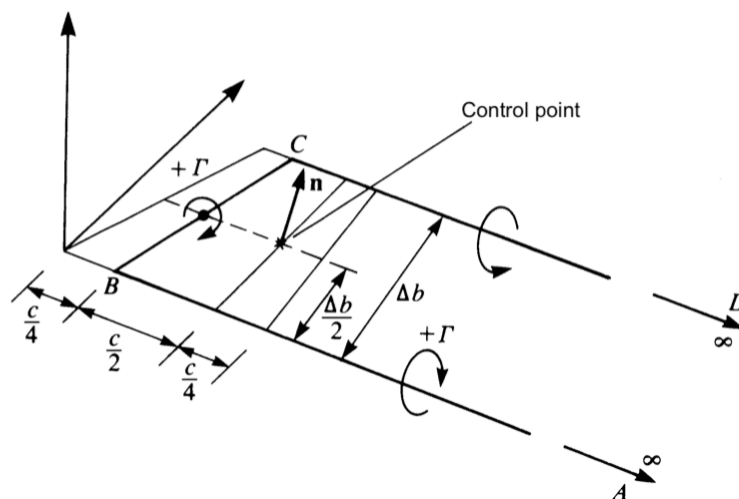


Figure 5.9: Definition of a single panel used in the VLM model [11].

The VLM aims to obtain the circulation strength of each horseshoe vortex. For a propeller-wing system, this is done by constructing a system of equations of the velocity field around the wing with a boundary condition. The boundary condition is formulated such that no velocity is present in the direction of the normal vector at the control point. Equation 5.11 shows the relation between the velocity at the control points located at each panel in the direction of the normal vector, \mathbf{U}_n . From this equation, three parts are identified influencing the velocity at the control point. The first component consists of the freestream velocity, U_∞ , and axial propeller-induced velocity, \mathbf{u}_x , both in the direction of the x -axis. The second velocity component contains the tangential propeller-induced velocity, \mathbf{u}_z . The last component includes the induced velocities of the horseshoe vortices of the panels, with yet unknown strength, on the control points. \mathbf{F} represents the matrix containing the aerodynamic influence coefficients (AIC) of each horseshoe vortex on each control point. Matrix \mathbf{G} is the correction matrix, which corrects for the finite size of the a propeller slipstream. This is further elaborated on in Section 5.2.2. With the previously mentioned boundary condition, the system can be solved such that the unknown circulation strength of all the individual horseshoe vortices is obtained [11]. The simplified system of equations is presented in Equation 5.12.

$$\mathbf{U}_n = (U_\infty + \mathbf{u}_x) \sin\left(\frac{\partial g}{\partial x} - \alpha\right) - \mathbf{u}_z \cos\left(\frac{\partial g}{\partial x} - \alpha\right) - (\mathbf{F} + \mathbf{G}) \Gamma \quad (5.11)$$

$$(\mathbf{F} + \mathbf{G}) \Gamma = \mathbf{U}_n \quad (5.12)$$

The spanwise lift distribution per unit span follows from the Kutta-Joukowski theorem and the circulation strength of each panel. This relation is given in Equation 5.13, where Γ is the circulation at a spanwise location of the wing. The effective velocity, U_{eff} , is the summation of the freestream velocity and the axial propeller-induced velocity. The total lift of the wing follows from the integration of the spanwise lift distribution over the span of the wing. The system lift coefficient of the propeller-wing system is obtained by the evaluation of Equation 5.14, where S is the surface area of the wing. The spanwise lift distribution is directly obtained with Equation 5.15, where c is the local chord of the wing. In these equations, the velocity within the propeller slipstream, U_{eff} is dependent on the spanwise coordinate of the wing.

$$l = \rho_\infty U_{eff} \Gamma \quad (5.13)$$

$$c_L = \int_{-b/2}^{b/2} \frac{l dy}{\frac{1}{2} \rho_\infty U_\infty^2 S} \quad (5.14)$$

$$c_l = \frac{2 \Gamma U_{eff}}{U_\infty^2 c} \quad (5.15)$$

The lift-induced drag of the isolated wing is obtained by a similar method [11]. First, the downwash from the horseshoe vortices on each bound vortex is obtained by Equation 5.16. From this equation, it becomes clear that the downwash is induced by the generation of lift of the wing, which is the circulation of the horseshoe vortices in the potential flow theory. Therefore, the subscript li is used to indicate the force or velocity that follows from the generation of lift by the wing. \mathbf{F}_w is the influence matrix of the components that induce downwash on the bound vortex of the horseshoe vortices of the panels. The coefficients are obtained similarly to those in \mathbf{F} . Singularities should be avoided, but it is noted that they can appear when the wing has sweep or taper. The spanwise lift-induced drag per unit span follows from Equation 5.17. The system lift-induced drag coefficient and spanwise lift-induced drag coefficients are obtained by evaluating Equations 5.18 and 5.19. An alternative method to obtain the lift-induced drag is a Trefftz-plane analysis. This analysis method is further explained in Appendix A and is used to make a comparison between the lift-induced drag obtained by the lifting-line theory and the previously explained VLM.

$$\mathbf{w}_{li} = \mathbf{F}_w \Gamma \quad (5.16)$$

$$d_{li} = \rho_\infty w_{li} \Gamma \quad (5.17)$$

$$C_{D_{ii}} = \int_{-b/2}^{b/2} \frac{d_{ii} dy}{\frac{1}{2} \rho_{\infty} U_{\infty}^2 S} \quad (5.18)$$

$$c_{d_{ii}} = \frac{2 \Gamma w_{ii}}{U_{\infty}^2 c} \quad (5.19)$$

Discontinuities in the spanwise lift distribution arise when this method is used for propeller-wing systems, by the contribution of correction matrix, \mathbf{G} . When this method is applied, an overestimation of the lift-induced drag will result as this performance parameter is dependent on the spanwise lift distribution. The local velocity is a reference value of the local circulation of the wing. This approach is changed in Section 5.2.2 such that a continuous spanwise lift distribution is obtained, followed by a more realistic lift-induced drag of the propeller-wing system.

All assumptions that come with the potential flow theory apply to the VLM. As no separation is possible in the model, the angle of attack of the wing should remain small to obtain realistic performance characteristics of the wing. Furthermore, the thin-airfoil theory is used as the panels are treated as two-dimensional sections [11].

5.2.2. Jet Correction

The original VLM only considers the freestream velocity, which is assumed to be uniform and extends to infinity around the wing. The propeller-induced velocities in Equation 5.11 are added to the system of equations as if they also extend to infinity for each spanwise section of the wing. By comparison with experimental data, Rethorst [34] showed that this leads to an overprediction of the lift of the wing within the propeller slipstream. Nederlof [10] further investigated this problem by comparing the VLM solution to the results from CFD analyses. A correction method is developed to account for the finite size of the propeller slipstream. First, the original correction by Rethorst is presented for a circular jet located at the center of the wing. Hereafter the method is adapted to be able to correct for propellers that are not located in the center of the wing. This correction method is successfully implemented in a parameter sensitivity study by Willemsen [19].

Rethorst Correction

A wing geometry with center-located jet velocity is schematically visualized in Figure 5.10 and is used to define the correction method. The circular jet has a radius, r_j , and a uniform jet velocity, U_j . The freestream velocity outside the jet is defined by U_{∞} . The correction method is based on two additional boundary conditions in addition to the VLM without propeller slipstream. The first boundary condition is based on pressure continuity over the slipstream boundary. The second is based on slipstream continuity, which ensures that velocities on both sides of the jet are in the same direction [10]. These boundary conditions are satisfied by introducing images of horseshoe vortices. Their strength is a function of the ratio between freestream and jet velocities, $\mu = U_{\infty}/U_j$. The solution for the system of equations from which the circulation distribution follows now consists of three parts. The first part is the regular circulation of the horseshoe vortices as previously described in Section 5.2.1. The other two parts make up for the corrections of the finite jet size. These two parts, each having a strength of $\Gamma/2$, are the even and odd parts of a horseshoe vortex. Together, they make a complete horseshoe vortex. The even part satisfies the pressure continuity boundary condition, and the odd part does so for the slipstream boundary condition [34].

The correction is implemented in the wing model the correction matrix \mathbf{G} and is added to the original AIC, \mathbf{F} , as stated in Equation 5.12. The correction matrix is the addition of the even and odd corrections: $\mathbf{G} = \mathbf{G}_e + \mathbf{G}_o$. The influence coefficients of the correction matrix follow from the position of the control point and the horseshoe vortex with respect to the slipstream of the propeller. There are four possibilities for the correction which are visualized in Table 5.1. The spanwise locations are nondimensionalized by $\eta = y/r_j$. The subscripts in the figures have two letters. j and o denote whether the control point or horseshoe vortex is located inside or outside the jet, respectively. For the full equations of the correction, the reader is referred to the work of Rethorst [34]. Nederlof [10] conducted a sensitivity study on the numerical solution of the correction method. The conclusions made in this sensitivity study are used for the evaluation of the correction within the numerical model of this thesis.

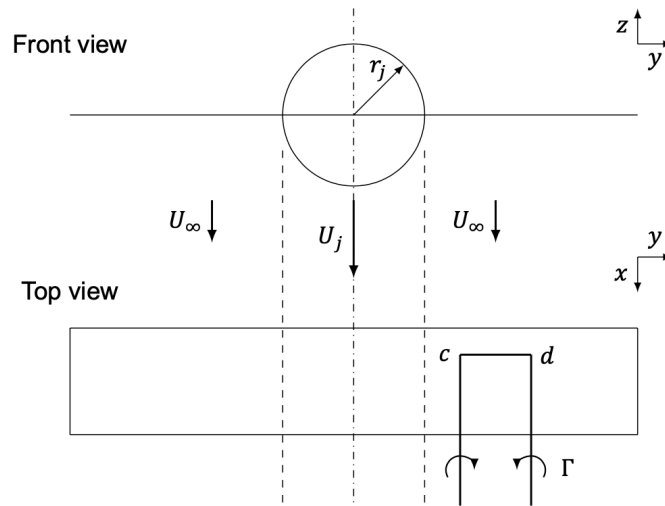


Figure 5.10: Propeller-wing system geometry used for the correction method [19].

Equally Divided Correction

As described previously, the original correction method from Rethorst [34] is developed for circular, uniform jets located at the center of a wing. For the correction to work, the jet centerline must coincide with the center of the wing. As there is interest in the influence of the propeller on various spanwise positions, Nederlof [10] has modified the correction method to be able to vary the spanwise position of the jet. This is done by adding a virtual wing extension to the side of the actual wing such that the jet centerline coincides with the center of the wing with virtual extension, as seen in Figure 5.11.

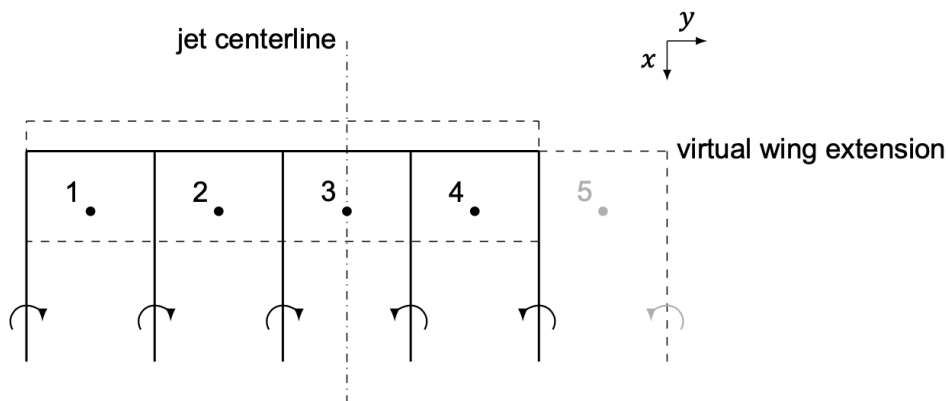
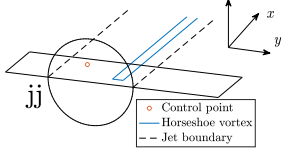
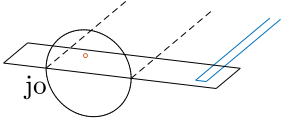
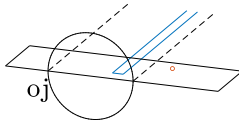
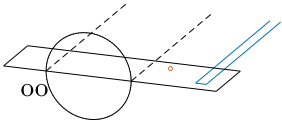


Figure 5.11: Wing with virtual wing extension for the correction of non-center located propeller slipstreams [19].

The equally divided correction method has been validated by Willemsen [19]. The results from the correction from Willemsen and from the implemented method are compared with CFD results from Willemsen as is presented in Figure 5.12. In this figure, a single axial velocity jump of $U_j = 1.5U_\infty$ is used at a spanwise location of $y_p = 0.5b/2$. The radius of the axial velocity increase is $r_j/b = 0.1$. The wing has an angle of attack of two degrees. This verifies the implementation of the correction in the numerical model. The slight deviations between the numerical model are allocated to a different amount of panels used during the analysis.

Table 5.1: Subscript notation for jet correction.

		Horseshoe vortex location	
		Inside jet $ \eta < 1$	Outside jet $ \eta > 1$
Control point location	Inside jet $ \eta > 1$		
	Outside jet $ \eta > 1$		

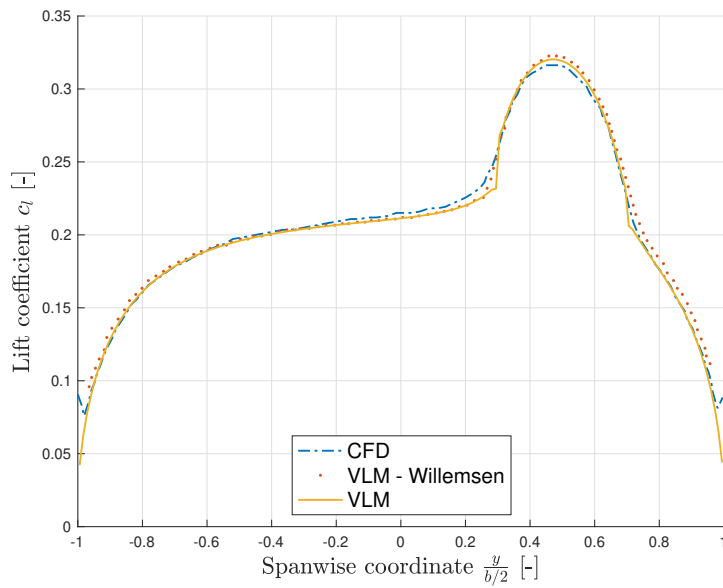


Figure 5.12: Comparison of the lift distribution for a wing with jet with $r_j/b = 0.1$ at $y/b = 0.25$ [19].

Mirror Propeller Influence

In Figure 5.12, only one propeller slipstream influences the wing. Two propellers would be placed on both wing sides to balance the thrust force. Therefore, the correction of the propeller is also applied to the propeller on the mirrored side of the wing. It is assumed that these propeller slipstreams do not interfere with each other. Equation 5.20 shows the final AIC that the VLM uses, where \mathbf{l}_p and \mathbf{r}_p denote the left and right propellers, respectively.

$$\mathbf{F}_{full} = \mathbf{F} + \mathbf{G}_{lp} + \mathbf{G}_{rp} \tag{5.20}$$

The largest effect of the correction is on the lift within and just outside the propeller slipstream. When the propellers are located close to the root of the wing, the correction of the right propeller influences the spanwise lift distribution on the left wing and vice versa. In Figure 5.13, the effect of the correction of the mirrored propeller is visualized. The influence of the correction of the propeller slipstream, which is not visible in this section of the wing span, results in a maximum deviation of 1.0%. This deviation decreases when the propellers are positioned closer to the tip of the wing.

The discontinuity of the spanwise lift distribution over the propeller boundary seen in the spanwise lift distribution follows from the presented correction method for a non-uniform axial velocity profile. A single value for the total axial propeller-induced velocity is used for the velocity ratio, μ , which is used in the correction. This value is the mean value of the average axial velocity over the full propeller slipstream. As the velocity near the propeller boundary is lower than this average velocity, the lift near the propeller boundary is over-corrected, resulting in a discontinuity. Important to note is that this discontinuity is different from the discontinuity discussed in the next section. This discontinuity in the spanwise lift distribution does not result in a problem when evaluating the lift-induced drag of the wing, as the discontinuity is small. Only minor deviations in the spanwise drag distributions follow, which do not dominate the conclusions in the analysis. Prabhu [32] presented a method for correcting a non-uniform axial propeller-induced velocity over a wing, which is further explained in Appendix D. The jet correction is applied for multiple velocities to correct the non-uniform axial flow. As the computational expense of the jet correction is high compared to all other modules of the numerical model, and multiple propeller-wing system configurations have to be evaluated, it is decided not to include this method of implementing the jet correction.

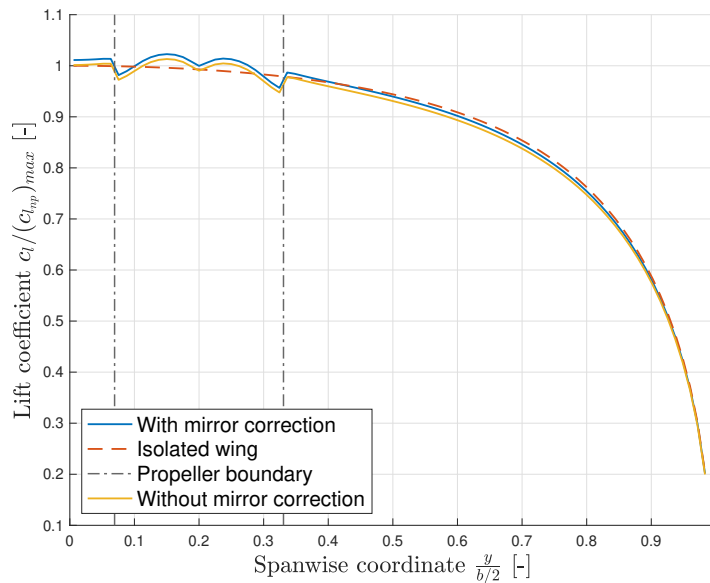
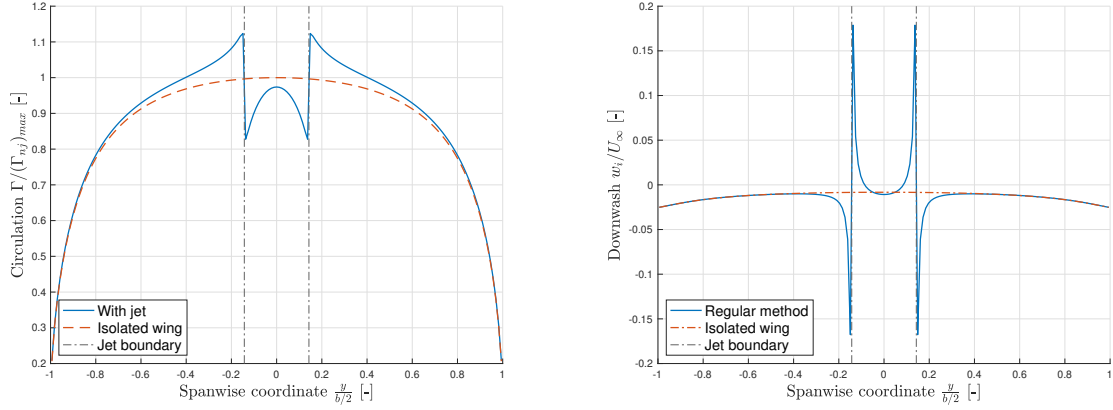


Figure 5.13: Influence of the correction of the mirror propeller at OP 1 located at $y_p = 0.2b/2$ with radius $r_p = 0.2b/2$ with only the axial propeller-induced velocities.

5.2.3. Modeling of Lift-Induced Drag for Propeller-Wing Systems

As is introduced in Section 5.2.1, the solution of the VLM for propeller-wing systems is discontinuous over the boundaries of the propeller. Such a discontinuous circulation distribution is visualized in Figure 5.14a. In this situation, a jet with a radius $R/b/2 = 0.143$ is located at the center of a straight rectangular wing with an aspect ratio of 9.33. A uniform jet with a velocity ratio of $\mu = 0.667$ is used for simplicity. The wing has a symmetric airfoil at an angle of attack of 4 degrees. When the downwash distribution is obtained with Equation 5.16, a strong trailing vortex induces downwash outside of the slipstream, and upwash inside, as seen in Figure 5.14b. In reality, however, the trailing vortices would be in the opposite direction, giving upwash outside of the slipstream and an increased downwash on

the inside of the slipstream as is schematically visualized in Figure 5.15, where a schematic representation of the actual lift throughout the wing can be seen. The steps, due to the increase in lift by the jet velocity, induce trailing vortices in the same direction as the steps at the wing tips. The arrows below the trailing vortices indicate the downwash at the section of the wing span. A different approach needs to be used to find the actual downwash of the wing with jet velocity, which is further elaborated on in this section.



(a) Discontinuous circulation distribution obtained with the Rethorst correction.

(b) Incorrect downwash obtained with the discontinuous circulation distribution.

Figure 5.14: Results directly following from the Rethorst correction with $R/b/2 = 0.143$ and $\mu = 0.667$.

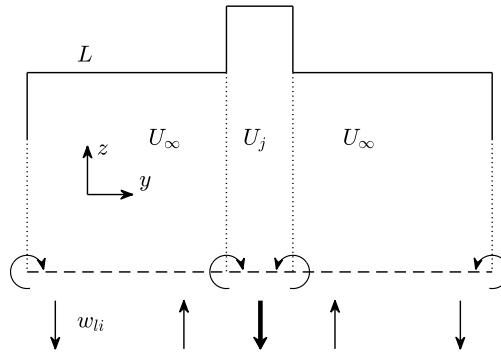


Figure 5.15: Schematic of the downwash by the trailing vortices from a wing in a jet.

The circulation of the bound vortex of each panel is related to the local velocity at that panel, as shown by the relation in Equation 4.1. Therefore, a higher lift is obtained within the jet with a relatively lower circulation compared to the wing section only experiencing the freestream velocity. According to Anderson [12], the circulation theory is an alternative way of thinking about the generation of lift of an aerodynamic body. Therefore, an alternative approach is taken toward defining the spanwise circulation for the propeller-wing system to obtain a realistic spanwise downwash distribution. This approach obtains the spanwise lift distribution from the discontinuous circulation distribution with Equation 5.21. Hereafter, the continuous circulation distribution, based on only the freestream velocity, Γ_F , is obtained with Equation 5.22. From this circulation distribution, the downwash is obtained with the original method from the VLM for an isolated wing as presented in Equation 5.16. The resulting downwash distribution from this method is seen in Figure 5.16.

$$l = \rho_\infty \Gamma U_{eff} \quad (5.21)$$

$$\Gamma_F = \frac{l}{\rho_\infty U_\infty} \quad (5.22)$$

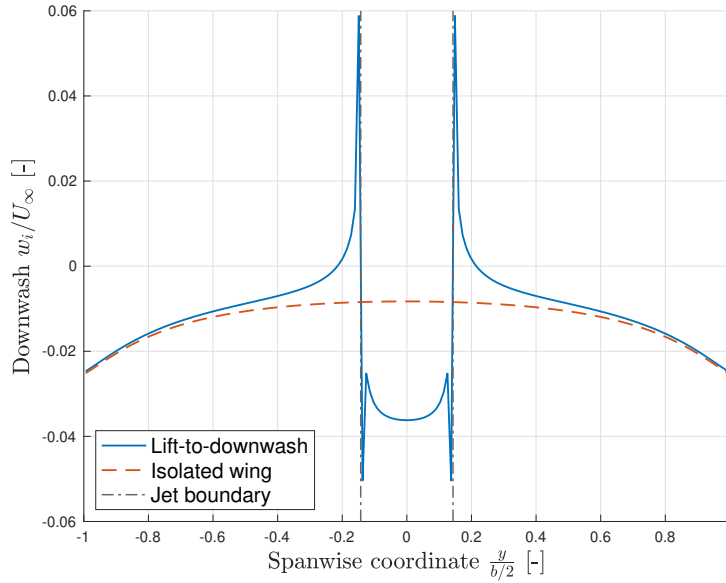


Figure 5.16: Downwash of the centered located jet by the circulation based on only the freestream velocity.

Subsequently, the spanwise lift-induced drag distribution is obtained by Equation 5.23, as the downwash is obtained with the circulation based on the freestream velocity only. In Figure 5.17, the lift-induced drag of the previously described propeller-wing system and isolated wing are seen. As expected from the spanwise downwash distribution, the lift-induced drag outside of the jet decreases, whereas the lift-induced drag within the jet increases significantly compared to the isolated wing with the same conditions without the presence of the jet. The drag coefficient is nondimensionalized with the freestream velocity, similar to the lift coefficient from the previous section.

$$c_{d_{ii}} = \frac{w_{li}}{U_{\infty}} c_l \tag{5.23}$$

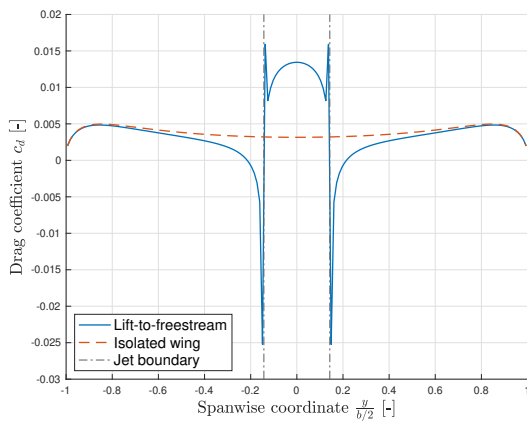


Figure 5.17: Lift-induced drag of a wing with a center located jet with $\mu = 0.667$.

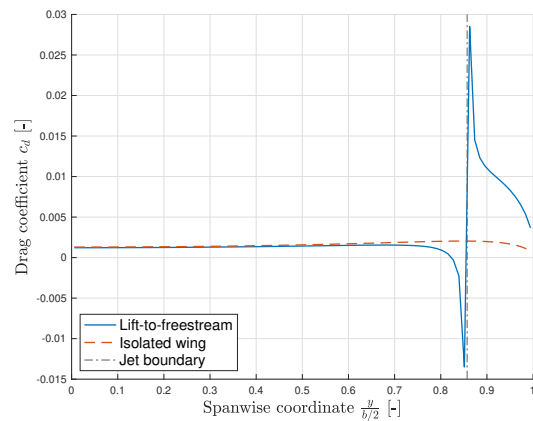


Figure 5.18: Lift-induced drag distribution with a tip located jet with $\mu = 0.667$.

Finally, the described method is used to obtain the lift-induced drag distribution of a jet stream located at the tip. The spanwise lift-induced drag distribution is visualized in Figure 5.18. It is seen that the lift-induced drag is reduced over the whole span outside the jet and significantly increased inside the jet. This increase is much higher than the centered located jet, which can be clarified by the circulation distributions presented in Figure 5.19. Both the centered and tip jet cause an increase in circulation.

For the centered jet, the vortex shedding over the slipstream boundary is significantly less compared to the shedding of a tip jet. This is because the circulation has to go to zero at the tip of the wing, whereas the circulation of the centered jet remains high. Therefore, the increased strength of the trailing vortices by the tip jet increases the lift-induced drag significantly.

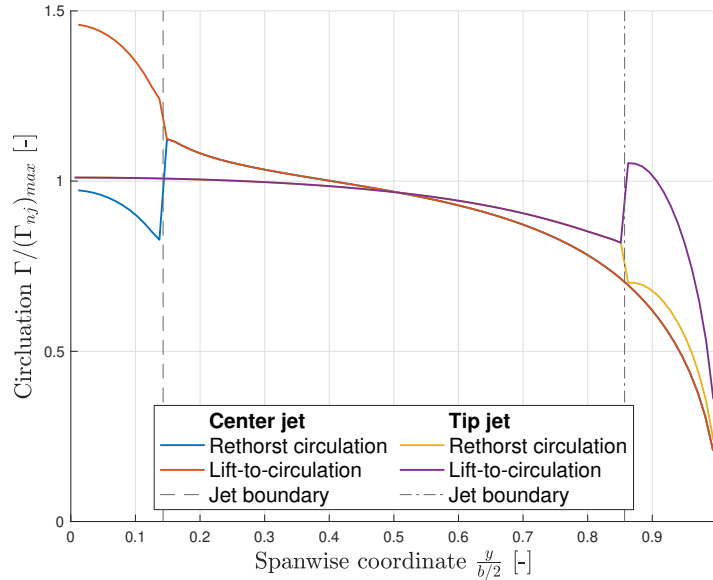


Figure 5.19: Circulations with local and freestream velocities as reference for the center and tip jet with $\mu = 0.667$.

Another method to obtain a realistic downwash distribution of a propeller-wing system is presented by Prabhu [32]. This method is only used for a center-located jet, and it was not possible to apply the correction for a jet where one of its boundaries is located outside the span of the wing, making it unsuitable for this thesis to use. A more detailed explanation of the correction is given in Appendix B.

5.2.4. Modeling of Swirl Recovery

In literature [9, 10, 19], it was shown that the tangential propeller-induced velocities could be taken into account by the change in the local angle of attack. Swirl recovery follows from this change in angle of attack behind the two sides of the propeller, as has been explained in more detail in Section 3.2.3. The coefficient for the swirl recovery, $c_{d_{sr}}$, is a drag coefficient, as this will be most convenient during the analyses of propeller-wing systems. It is related to the change in the angle of attack and the lift coefficient as is seen in Equation 5.24, where u_z is the propeller-induced tangential velocity. A negative value of this coefficient indicates a thrust contribution, and a positive value indicates a drag contribution. The relation between the velocities at the wing and the change in the local angle of attack is seen in Equation 5.25.

$$c_{d_{sr}} = \frac{u_z}{U_{eff}} c_l \quad (5.24)$$

$$\alpha_p = \text{atan} \left(\frac{u_z}{U_\infty + u_x} \right) \quad (5.25)$$

This method of modeling the contribution of the tangential propeller-induced is relatively simple compared to how the axial velocity from the propeller is implemented in the system. The axial propeller-induced velocity is averaged over the height of the propeller, and a correction method is applied for the finite height of the propeller slipstream. No similar correction method to the lift of the wing is found in the literature for the finite height of the propeller slipstream from a tangential propeller-induced velocity perspective. The averaging of the tangential velocity over the height of the propeller can be done in the

same manner as is done with the averaging of the axial propeller velocity. This method is described in Appendix C, whereafter it is applied to a propeller-wing system. As no reliable validation method can be used for the method of averaging the tangential velocity, it is decided not to implement this averaging.

5.3. Propeller & Wing Model Integration

The parts of the numerical model are presented in the previous sections of this chapter. Yet, they can be used together in various ways. Therefore, additional details of the integration of the parts are presented such that they can be used for the analysis of the propeller-wing systems.

A schematic visualization of the side view of the propeller-wing system is given in Figure 5.20. The propeller orientation remains perpendicular to the direction of the freestream. Behind the propeller, the propeller-induced velocities obtained by the slipstream tube model are indicated by u_x and u_z . The velocity experienced by the wing is decomposed into the axial velocity, which is an addition of the freestream and axial propeller-induced velocities and the tangential propeller-induced velocity. It should be noted that the propeller-induced velocities are used to analyze the propeller-wing system but that the thrust of the propeller is left out of consideration. The control points of the panels remain on the same vertical height as the longitudinal axis of the propeller slipstream. This is important as the jet correction assumes that the wing is located in the center of the jet with respect to its height. The orientation of the wing changes with the angle of attack, which should remain small for three reasons. First, the small-angle approximation is used throughout the model, and second, to realistically represent propeller-wing systems, the angle between the propeller and wing should remain small. Third, increasing the angle of attack of the wing too much would, in reality, result in flow separation, which is not included in the numerical model based on the potential flow theory. Furthermore, x_v indicates the distance between the propeller plane and the control point of the wing. This variable is also visualized in Figure 5.21, where a schematic top view of the propeller-wing system is shown. In this figure, it is seen that the boundaries of the propeller intersect with the trailing vortices of the horseshoe vortices of the VLM and that the propeller center is located in front of a control point.

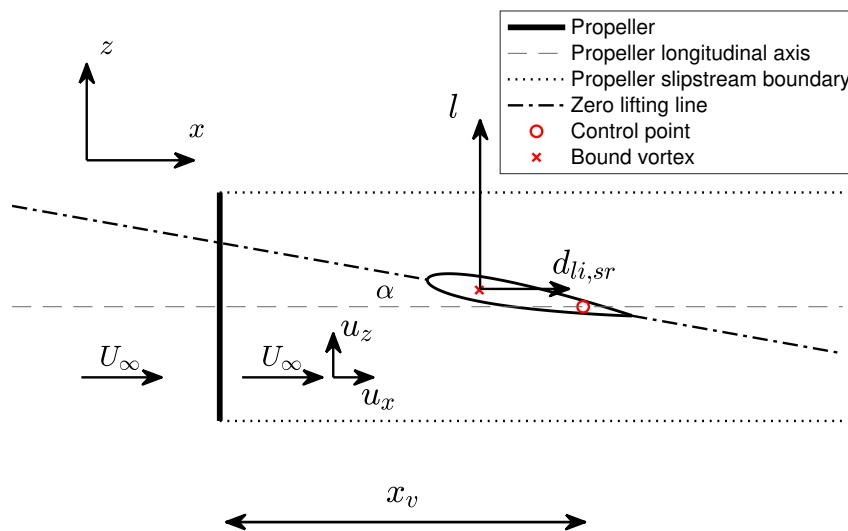


Figure 5.20: Side view of the propeller-wing system configuration within the propeller slipstream for the analysis in Part III.

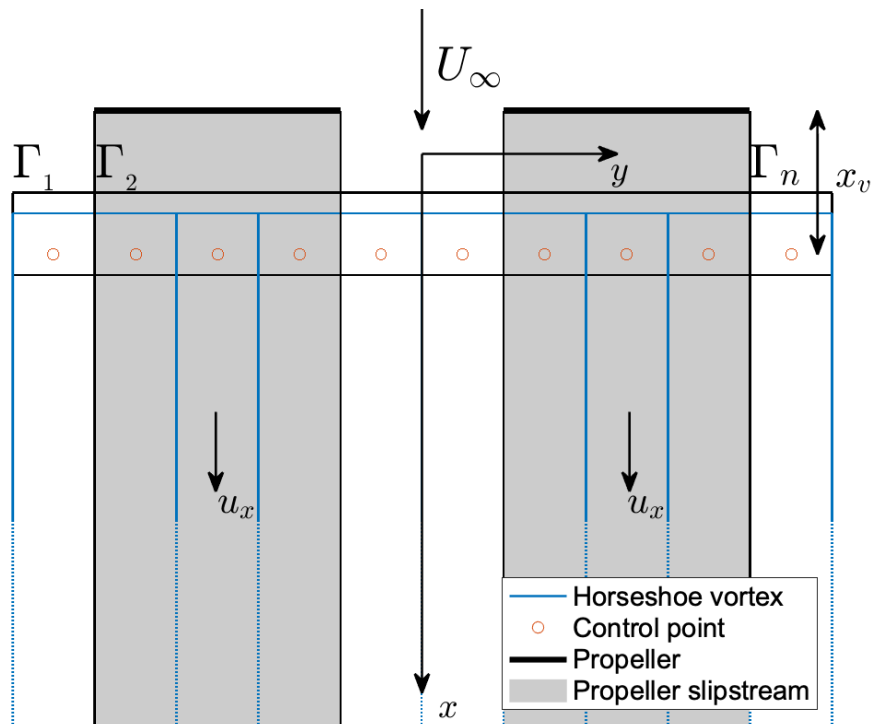


Figure 5.21: Top view of the propeller-wing system configuration for the analysis in Part III.

Another assumption of the Rethorst correction as described in Section 5.2.2 is the uniform jet velocity throughout the propeller slipstream. The velocity ratio, μ , used for the equations in the correction can only take one value for the jet velocity. During the analysis, the mean value of the averaged axial velocities over the radius of the propeller slipstream is used for the correction. The method of correcting for a non-uniform axial propeller-induced velocity profile is given in Appendix D. This additional correction would, however, increase the computational expense of the model significantly, making it not suitable for the analyses of multiple propeller-wing system configurations.

The components of the numerical model have been fully covered in the past chapters. The ability of the numerical model to analyze the relative contribution of the lift-induced drag and swirl recovery drag makes it unique. Before the numerical model is used for the analysis of propeller-wing systems, validation of the numerical model is conducted to evaluate its accuracy. This is done by the comparison with results from wind tunnel experiments and is presented in the following chapter.

6

Validation of the Numerical Model

The validation of the numerical model is conducted in parts. First, the isolated propeller is validated in Section 6.1. The isolated wing is validated hereafter in Section 6.2. In the last section of this chapter, the interaction between the propeller and wing in the numerical model is validated, as this is essential for the analyses within this research.

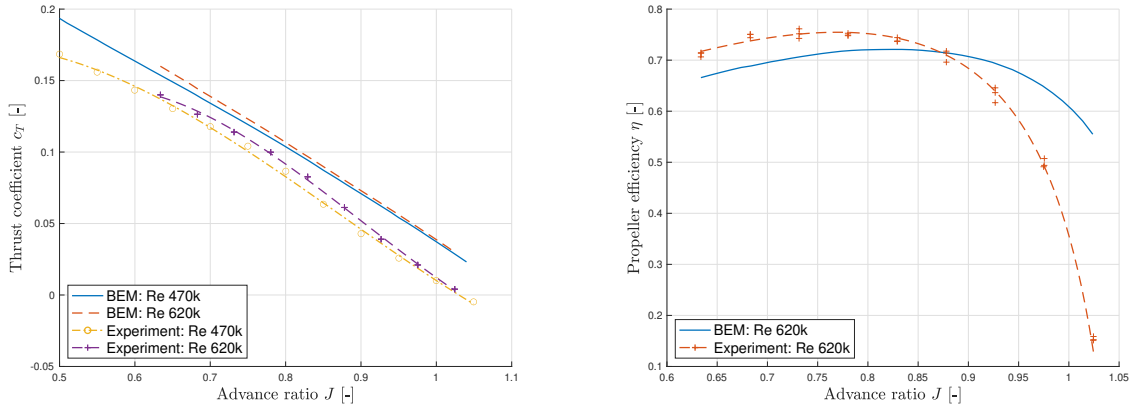
6.1. Isolated Propeller Model

The validation of the isolated propeller consists of two parts. The BEM method is validated with results from a wind tunnel experimental in Section 6.1.1. The circulation distribution over the propeller blades obtained by the BEM method is used as input by the slipstream tube model, which is the second module of the propeller model. The induced velocities from the slipstream tube model are validated in Section 6.1.2. The BEM model is validated with experimental data from the wind tunnel experiment carried out by Sinnige et al. [21]. The experiments are carried out in the Low-Turbulence Tunnel at the Delft University of Technology. The slipstream tube model is verified by with induced velocities from the BEM model, whereafter it is validated with results from a CFD analysis from Sinnige et al. [35]. The propeller used in both experiments has four blades and a radius of 0.237 meters. The blade pitch defined at 75% of the radius is set to 23.9 degrees.

6.1.1. BEM Model

In Figure 6.1, experimental results from Sinnige et al. [21] and from the BEM model are presented. The isolated propeller was mounted to a sting with a spacing of 1.5 times the radius of the propeller between the propeller plane and the sting. This distance was determined to be sufficient to prevent an upstream effect of the sting on the propeller performance. Blades-off measurements were made to take the forces of the sting into account. The change in forces on the nacelle by the influence of the propeller slipstream is not taken into account. The data points of the experiment are included in the figures. The experimental data was captured at an angle of attack of -0.2 degrees at a Reynolds number based on the propeller diameter of 470,000 and 620,000. The results from the BEM model are obtained at an angle of attack of zero degrees. A third-order polynomial is used through the experimental data, as this results in the best fit through the data [21].

The results from the BEM method follow the same trend as those from the experimental for both Reynolds numbers in Figure 6.1a. The amount of thrust, however, is overestimated by the BEM method. According to Willemsen [19], the offset could be caused by a simple geometry modeling error or by the low Reynolds number at which the propeller is operating. For lower Reynolds numbers, it becomes harder to predict the airfoil performance by the increase in the viscous effects. More likely would be the additional effects that follow from the rotation of the propeller blades, which the BEM method does not model, as the airfoil polars are obtained without these rotational effects. Decambering is one of these effects for propellers, referring to the fact that the induction from the free vortices in the wake by the airfoil of the propeller is seen as a negative cambering of the chord line [36]. This effect is mainly present near the tip of the propeller and is not considered in the BEM formulation. According



(a) Thrust coefficient for advance ratios obtained from the BEM method and by experiments with the isolated propeller.

(b) Propeller efficiency for advance ratios obtained from the BEM method and by experiments with the isolated propeller.

Figure 6.1: Validation of the BEM model with data from the isolated propeller in the experiment of Sinnige et al. [21].

to Benini [37], the prediction of the incidence angles by the BEM method is poor, which leads to errors in the prediction of the BEM method. The prediction is best for the design advance ratio when three-dimensional effects are of secondary importance. Since the thrust coefficient increases more than the power coefficient as a function of the advance ratio, the efficiency tends to be more over-predicted for higher advance ratios. This is visualized in Figure 6.1b, where the predicted efficiency of the BEM method is significantly larger for advance ratios higher than 0.9 compared to those of the experiment. The same figure shows a design advance ratio of approximately 0.8 in the experimental data, as the efficiency reaches a maximum. At this design ratio, it is seen that the performance prediction of the BEM method comes closest to the experimental results. To use the most reliable outcome from the BEM method, predictions of the propellers should be used such that they operate at or near the design advance ratio. The design advance ratio is dependent on the pitch setting of the propeller. In Section 7.1.1, the operating point of the propeller is determined such that the propeller efficiency is maximal.

6.1.2. Slipstream Tube Model

The results from the slipstream tube model are first verified by the induced velocities from the BEM. Hereafter, the induced velocities from the slipstream tube model are compared to the results from a CFD analysis.

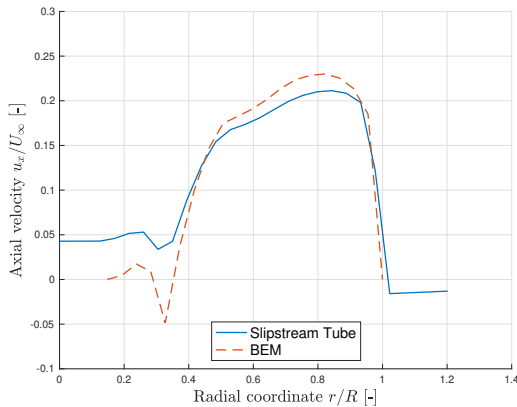
BEM verification

For the validation of the slipstream tube model, the propeller-induced velocities obtained by the slipstream tube model are compared to those from the BEM method for an advance ratio of 0.8. First, the axial and tangential velocities of the slipstream tube model and BEM are compared at a streamwise position of $x = R$ behind the propeller, whereafter the same is done for a position infinitely far behind the propeller.

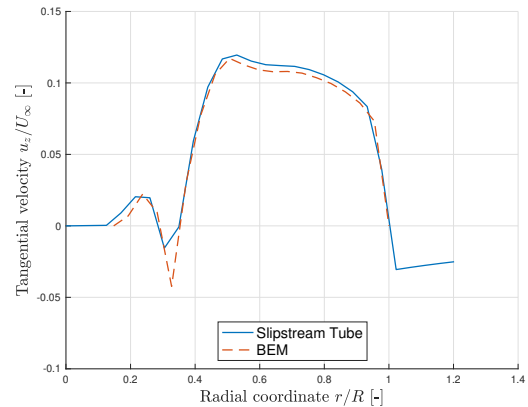
From literature [38], it is known that the axial velocity behind the propeller increases gradually. A theoretical approximation of this velocity increase with respect to the distance behind the propeller, x , is given by Equation 6.1. u_{a_0} is the axial induced velocity at the propeller disk, known from the BEM method. With this equation, the axial induced velocities by the BEM method can be translated to any distance behind the propeller. The tangential velocity in front of the propeller is zero, one time the induced velocity at the location of the propeller. Behind the propeller the tangential velocity remains constant at two times the induced velocity [9].

$$u_a = u_{a_0} \left(1 + \frac{x}{\sqrt{x^2 + R^2}} \right) \quad (6.1)$$

In Figure 6.2, the estimation of the induced velocities from the propeller is seen at $x = R$. It is noted that the shape of both radial velocity distributions follow the same trend over the radial positions of the propeller. Although both methods provide induced velocity distributions following the same trend, three important aspects are mentioned about the results. Firstly, the axial velocities near the center of the propeller are predicted to be higher by the slipstream tube model compared to those from the BEM method. This subsequently results in lower axial velocities over the middle of the blade. The same reasoning can follow for the tangential velocities. In this case, however, the tangential velocities from the slipstream tube model are slightly lower than those of the BEM method. Second, the discontinuous results following the discretization of the propeller into sections should be taken into account. These irregularities flatten out by the viscous effects in the slipstream of the propeller [39]. Finally, outside the propeller slipstream tube, where $r > R$, the axial and tangential velocities are negative. These velocities are small and do not have a significant influence on the performance of the propeller-wing system compared to the influence of the velocities within the slipstream. The velocities outside of the slipstream are kept at zero during the analyses.



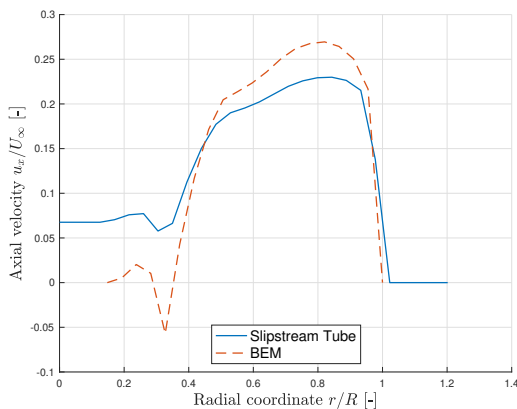
(a) Radial distribution of the axial velocity.



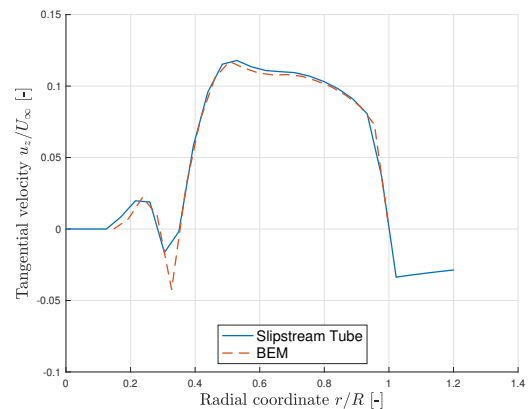
(b) Radial distribution of the tangential velocity.

Figure 6.2: Induced velocities by the BEM method and slipstream tube model at $x = R$ for $J = 0.8$.

Equation 6.1 can also be used to find the propeller-induced axial velocity infinitely far away from the propeller such that $x \rightarrow \infty$. The axial velocity obtained by the BEM method has slightly increased compared to the first location. The velocities obtained by the slipstream tube model are slightly flattened out compared to those from the BEM method. It is increased over the center of the propeller and decreased closer to the boundary of the propeller slipstream. The swirl remains constant over the whole slipstream domain of the propeller, which is confirmed when Figures 6.2b and 6.3b are compared. Only small deviations are present, which are allocated to numerical errors.



(a) Radial distribution of the axial velocity.



(b) Radial distribution of the tangential velocity.

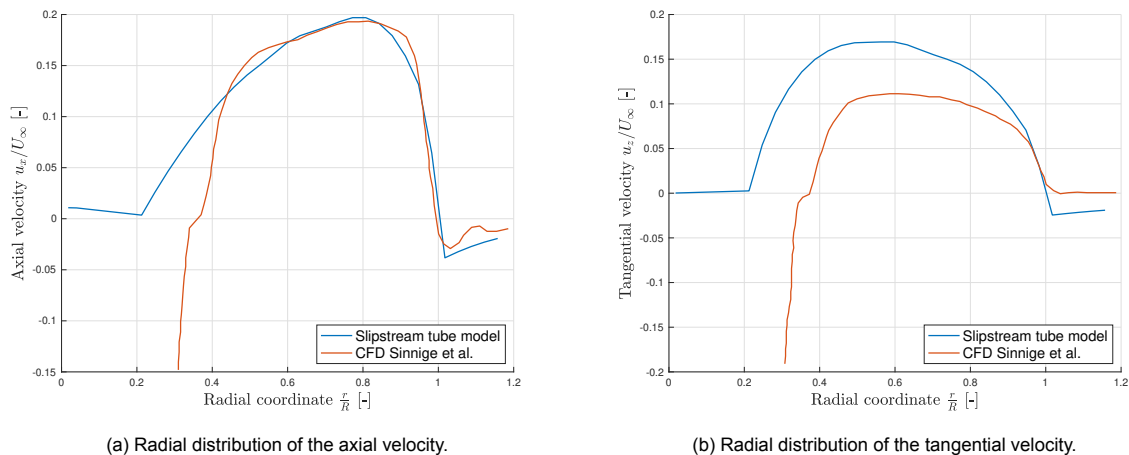
Figure 6.3: Induced velocities by the BEM method and slipstream tube model at $x \rightarrow \infty$ for $J = 0.8$.

CFD validation

The slipstream tube model is validated with the induced velocities from the CFD analysis from Sinnige et al. [35]. In this study, various advance ratios were analyzed. The advance ratio of 0.8 was found to be the only suitable one to validate the slipstream tube model. The other operating points with higher advance ratios are used to analyze the propeller in energy harvesting mode, such that the thrust is near zero or negative.

The propeller-induced velocities obtained by the slipstream tube model and CFD analysis are presented in Figure 6.4. Although there are discrepancies between the results, the agreement between the results is reasonable, and most importantly, the distributions of the velocity profiles are similar. First, it is seen that the axial and tangential velocities from both methods near the center of the propeller deviate strongly from each other. In the CFD analysis, the influence of the propeller nacelle is taken into account, which is not done in the numerical model of this thesis. Behind the center of the propeller, a wake results from the propeller nacelle such that the induced velocities are low. Furthermore, it is seen that the axial velocity distribution is similar for a large part of the propeller slipstream. In Figure 6.4b, it is seen that the induced velocities by the slipstream tube model are overestimated compared to those from the CFD analysis. This difference is also related to the influence of the nacelle of the propeller, as the differences are larger near the center of the propeller slipstream than those near the slipstream boundary. Sinnige et al. [35] also indicate the flow separation at the propeller blade at the advance ratio of 0.8. This flow separation is not taken into account by the BEM model and the slipstream tube model, leading to discrepancies.

Especially from the tangential velocity distribution, it is seen that a difference between the velocities outside the radius of the propeller is present, which cannot be clarified. For this reason, the velocities obtained from the slipstream tube model are only used within the slipstream of the propeller, such that the wing outside the slipstream only experiences the freestream velocity.



(a) Radial distribution of the axial velocity.

(b) Radial distribution of the tangential velocity.

Figure 6.4: Induced velocities by the slipstream tube model and the CFD analysis at $x = 0.19R$ from Sinnige et al. [35].

6.2. Isolated Wing Model

The validation of the VLM without propeller-induced velocities is done in twofold. First, the results from the numerical model are compared with the results from *XFLR5*, which is an open-source tool for the analysis of airfoils, wings, and planes¹. Secondly, the results are compared with the experimental data from Sinnige et al. [21], so deviations with real flow phenomena can be considered when using the VLM.

¹Retrieved from <http://www.xflr5.tech/xflr5.htm> on 21/7/2022.

6.2.1. XFLR5 Verification

The arbitrary wing for the validation with *XFLR5* has a symmetric airfoil and an aspect ratio of 12. The angle of attack and freestream velocity are set to 4 degrees and 40 m/s, respectively. In Figure 6.5, the results from *XFLR5* are compared with the VLM. It is seen that the results from the *XFLR5* and the VLM are almost identical. The maximum difference between the lift coefficients for the flight angle of attack is less than 0.5%. This verifies that the VLM is working properly and can be used for further validation with experimental results.

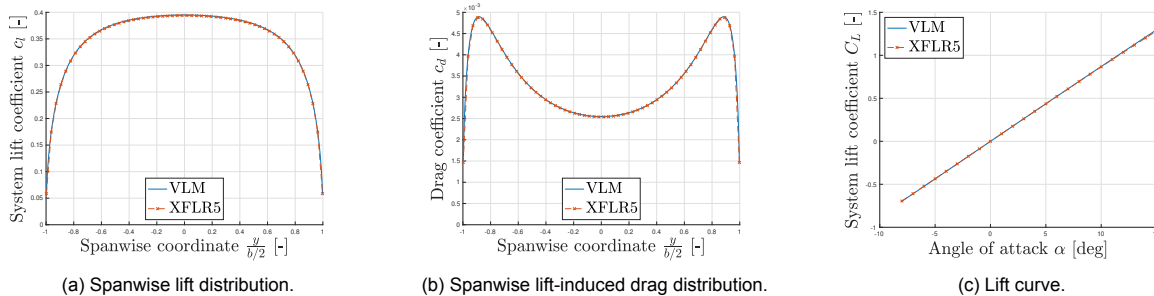


Figure 6.5: Validation of the VLM with *XFLR5*.

6.2.2. Experimental Validation

The second part of the isolated wing validation is with the experimental wind tunnel data from Sinnige et al. [21]. A schematic view of the wing is seen in Figure 6.6. For the experimental data in this section, the wingtip-mounted configuration is used without the propeller blades attached. The nacelle of the propeller remains attached.

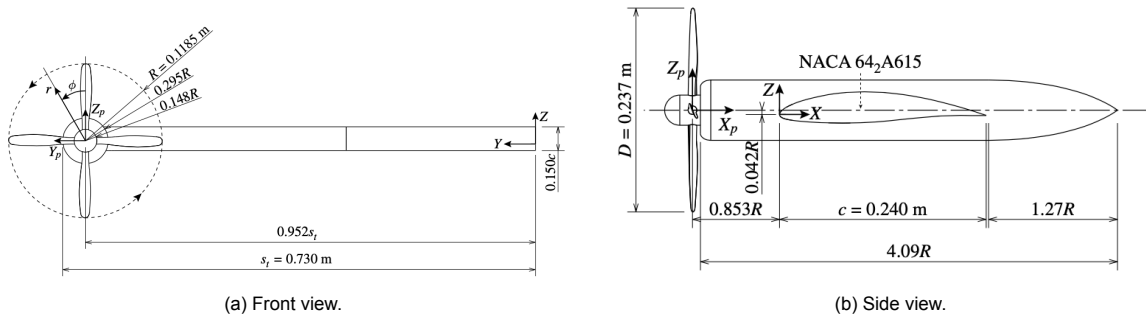


Figure 6.6: Model 2 of the wind tunnel experiment from Sinnige et al. [21] where the propeller is located at the wingtip.

In Figure 6.7, the results from the VLM are compared with those of the wind tunnel experiment. The lift curves are almost identical, except from an angle of attack of approximately eight degrees, where viscous effects start to influence the results of the experiment. Flow separation is not taken into account in the numerical model as this is a viscous effect, and the VLM is based on the potential flow theory, which assumes the flow to be inviscid. To compare the drag of the VLM with those from the wind tunnel experiment, the viscous drag is removed from the total drag of the wing in the experiment. This is done by approximating that the viscous drag, $c_{D_{min}}$, is equal to the minimum drag coefficient of the wing when zero lift is produced. The result is seen in Figure 6.7b. Close to zero drag, it is seen that the prediction of the lift by the VLM is slightly underestimated. This could be due to the definition of the boundary condition that has been set in the VLM, which is based on the gradient of the camber line, and not on the actual surface of the wing. The gradient of the actual surface of the wing is larger with respect to the gradient of the camber line at the same chordwise position. The amount of circulation would be higher when the gradient at the location of the control point is increased. When the angle of attack increases, the effect of this underestimation of the gradient of the airfoil shape becomes less pronounced, resulting in a better estimation of lift and drag by the VLM. When the angle of attack further increases, another viscous effect, pressure drag, further increases the drag leading to deviations

between the VLM and the experimental data [25]. Furthermore, in this wind tunnel experiment, the blades of the propeller were removed, but the nacelle remained present at the location of the tip. The nacelle increases the amount of drag of the wing by the increase in the wetted area of the wing and by the increase in pressure drag.

From the comparison between the results of the VLM and the experiment, it is concluded that the lift and lift-induced drag are properly predicted by the VLM, especially when the angle of attack remains small such that no additional viscous effects increase the drag. During the analysis by means of the numerical model, the angle of attack of the wing should remain under eight degrees to avoid discrepancies with reality where flow separation would influence the system performance.

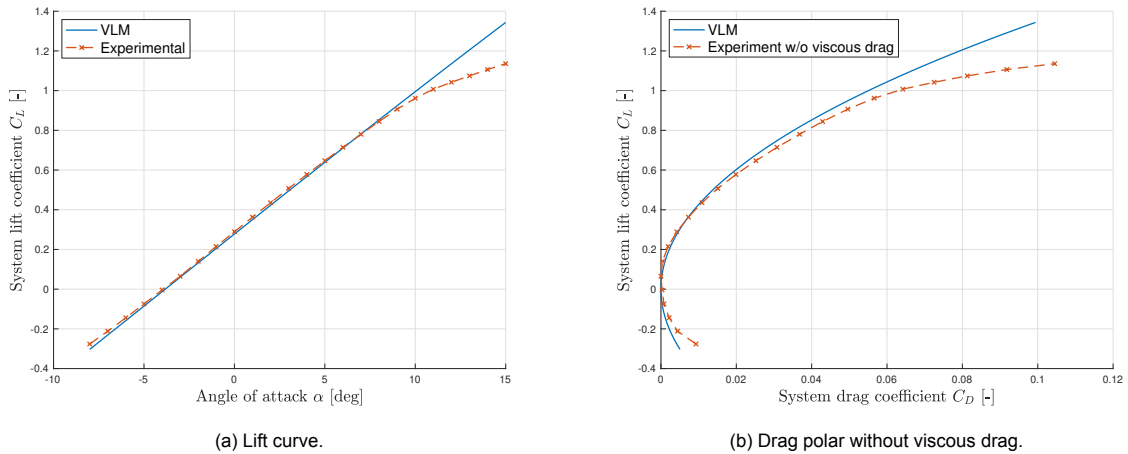


Figure 6.7: Validation of the VLM with experimental data from Sinnige et al. [21].

6.3. Propeller-Wing System

The propeller-wing system is validated by the wind tunnel experiment conducted by Sinnige et al. [21]. One substantial difference between the numerical model and the model used during the wind tunnel experiment should be addressed before the validation. In the analysis of this thesis, the propeller is fixed with an orientation such that it remains perpendicular to the freestream. The experimental data was obtained for a propeller-wing system, where the angle of attack of the propeller plane increases when the angle of attack of the system increases. The results from the numerical model and the wind tunnel experiment cannot be properly compared when the numerical model is not changed. Therefore, during this validation, the numerical model is altered such that the propeller rotates with the angle of attack of the propeller-wing system. With this alteration, the results from the numerical model will be better comparable to those from the wind tunnel experiment. The influence of the angle of attack of the propeller plane with respect to the freestream is not taken into account by the numerical model. The isolated propeller performance shows that the propeller thrust increases with the angle of attack, especially for lightly loaded propellers. For this reason, the predicted thrust of the system by the numerical model is lower than it is in the wind tunnel experiment. The experimental data consists of forces, which are measured by the external balance to which the propeller-wing system is attached. These measured forces consist not only of the lift, lift-induced drag, and swirl recovery of the system but also of the viscous drag and the thrust by the propeller. The last two forces are not included in the results of the numerical model. To compare the numerical model with the experiment, an approximation of these two forces of the system has to be made. The friction drag from the propeller-off configuration is included in all configurations analyzed with the numerical model. For higher disk loadings and higher angles of attack, this friction drag is an underestimation of the actual friction drag [40]. The thrust of the isolated propeller is added to the numerical model to better approximate the total forces of the system in the direction of the freestream. As discussed in Chapter 3, the static pressure increase in front of the wing increases the thrust of the propeller. This effect is not included in the numerical model and should therefore be considered during the validation.

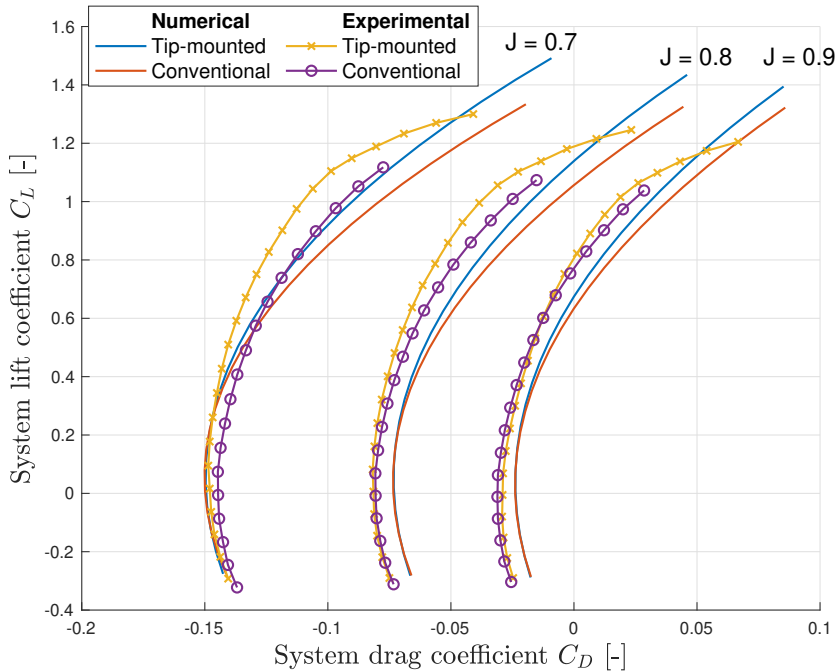


Figure 6.9: Drag polar of the propeller-wing system for a conventional and tip-mounted inboard-up rotating propeller.

stall of the propeller-wing system. The thrust of the propeller is included in the numerical model as if the propeller is isolated from the wing and does not have an angle of attack with respect to the freestream. The experimental data shows that the thrust increases with the angle of attack of the propeller, especially for propellers with low disk loadings, as is the case for an advance ratio of 0.9. This results in a deviation in Figure 6.9, where at higher lift coefficients, more thrust is present in reality, shifting the polar from the experimental data more towards the negative drag values. This effect is significantly less for a higher disk loading of the propeller, where the prediction of the numerical model is better at these higher lift coefficients. Another reason for the under-prediction of thrust by the numerical model is the fact that the model is a SIM. The induced velocities of the wingtip vortex decrease the effective advance ratio of the inboard-up rotating propeller such that the thrust of the propeller is increased. The strength of the wingtip vortex increases with the lift coefficient, resulting in an even higher thrust of the propeller at higher angles of attack, as is explained in Section 3.1. The numerical model does not take the effect of the wing on the propeller into account. Therefore, it should be kept in mind that, in reality, the thrust of the propeller is higher for an inboard-up rotating propeller, especially those located near the wingtip at higher angles of attack. The same reasoning is made with the phenomenon of blockage, as has been explained in Section 3.1. The effective advance ratio decreases with the increased static pressure in front of the wing. This subsequently increases the thrust of the propeller, which is not taken into account by the numerical model. The viscous drag of the wing increases with the increased dynamic pressure by the slipstream of the propeller [41]. This effect is not included in the numerical model. The increase of the viscous drag by the propeller slipstream is seen at the region where the lift coefficient is low, and contribution of the viscous forces to the total drag of the system is larger. Comparing the polars obtained with the different advance ratios, it is seen that this effect starts to dominate for higher advance ratios as the numerical model under-predicts the drag for the advance ratio of 0.7. As this under-prediction is not the case at a higher advance ratio, it is expected that this effect does not dominate at these advance ratios. The amount of this drag is seen when comparing experimental results from the tip-mounted and conventional configuration at zero lift. The drag of the tip-mounted configuration is slightly lower as only half of the propeller slipstream goes over the wing surface compared to the conventional configuration. This amount of drag by the propeller slipstream is proportional to the drag contribution missing for the numerical model at zero lift.

Although the thrust of the system is under-predicted, it should be mentioned that the swirl recovery of the system could be over-predicted. Nederlof [10] has shown the over-prediction of the estimation of lift by using the change in the local angle of attack as is explained in Section 5.2.4. As the swirl recovery depends on the amount of lift of the wing behind the propeller, the swirl recovery could be over-predicted. This over-prediction is hard to quantify as the balance system from the experiment only measures a single drag force. It could be that the previously described under-prediction of thrust is even higher than visually present in the figures from the validation, as the over-prediction of lift leads to an over-prediction of the swirl recovery thrust. These two modeling errors could cancel each other out and should therefore be taken into account in the discussion of the results.

6.3.2. Rotational Direction of the Propeller

Another essential characteristic of the propeller-wing system having a significant impact on its performance is the rotational direction of the propeller. The influence of this characteristic is therefore validated with another model from Sinnige et al. [21], which is seen in Figure 6.10. Again the drag coefficient is the summation of the thrust and drag of the propeller-wing system. This model has a shorter span than the previous validation model. The propeller is located at the wingtip for both configurations. The straight wing has a symmetric airfoil with an integrated flap from $y_p/b/2 = 0.163$ to $y_p/b/2 = 0.729$. The experimental results are obtained with a flap deflection of 10 degrees. The flap is taken into account in the VLM by adding a twist to the wing located within this section. The amount of twist results from the angle between the chord line of the original airfoil without flap deflection and the chord line of the airfoil with flap deflected, which is the line from the leading edge to deflected trailing edge of the flap.

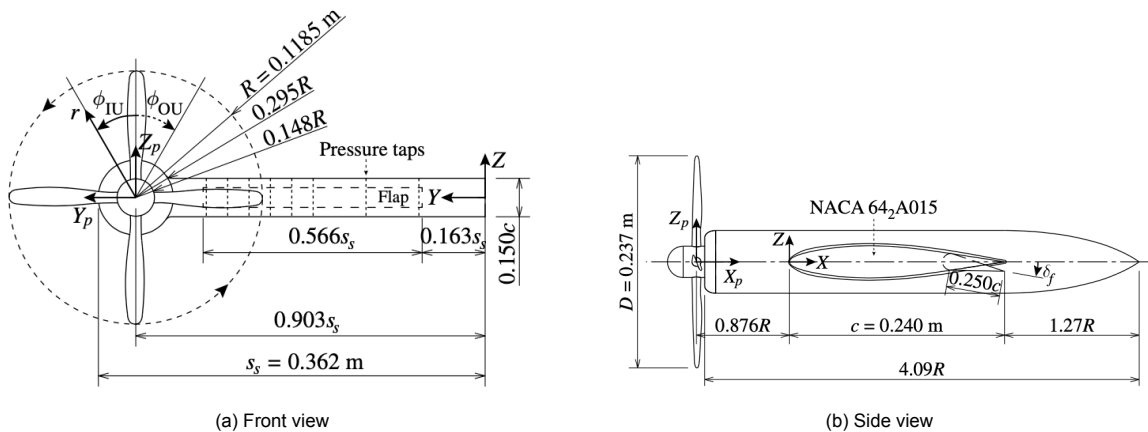


Figure 6.10: Technical drawing of model 1 from the experiment from Sinnige et al. [21].

The results from the numerical model and experiment for the three different propeller cases are presented in Figure 6.11. Comparing the results from this model to those of the previous section, it is seen that the predictions of the numerical model have a larger discrepancy with the experimental results. Again, the influence of the rotational direction of the propeller is distinguished in the results of the numerical model. First, in Figure 6.11a, it is seen that when the wing is producing positive lift, the system with an inboard-up configuration has a lower drag than the inboard-down configuration. The contrary happens when the wing produces a negative lift and the wingtip vortex changes direction. In this case, the benefits are with the inboard-down rotating propeller, as it rotates in the opposite direction with respect to the wingtip vortex. Secondly, the effects of the interactions between the propeller and wing increase with higher disk loadings of the propeller, which is included in the results of the numerical model as the difference between the curves increases by approximately the same rate as for the experimental results. Furthermore, the lift augmentation by the inboard-up configuration is seen in Figure 6.11b as the lift of the inboard-up configuration is higher than that of the inboard-down configuration for the same angle of attack. Furthermore, the accuracy of the lift curve slope of the numerical model is high when the viscous effects do not dominate.

Two points can be made on the discrepancies between the numerical model with the experimental results. The first one is the simplistic way of how the flap was modeled [42]. Second, the increase in viscous drag due to the propeller slipstream can also be seen in the results of this experiment. In this experiment, the contribution of the viscous force is more significant compared to the model from the previous section, as the slipstream from the propeller covers a larger section of the wing. For the same reason, the discrepancies are larger in this validation than in the previous section.

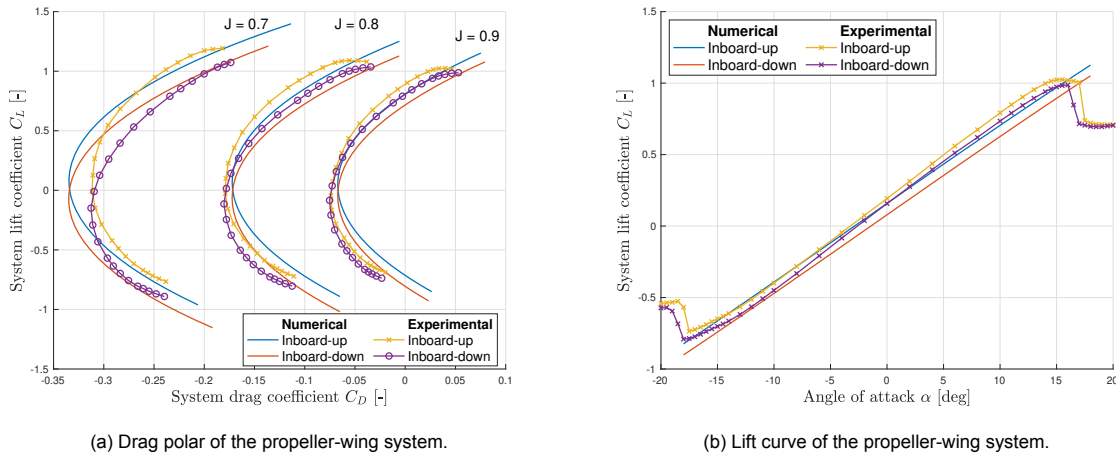


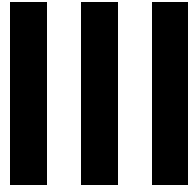
Figure 6.11: Validation of the numerical model with the experimental results from model 1 from Sinnige et al. with a flap deflection of 10 degrees [21].

6.4. Limitations of the Numerical Model

From the validation, it is concluded that the numerical model can be used to analyze the propeller-wing system as the propeller-wing interaction effects from the spanwise position, rotational direction, and disk loading are properly included. There are, however, discrepancies with the wind tunnel experiment. Therefore, some notes are made that should be taken into account when using the numerical model.

First of all, the viscous effects are not taken into account by the numerical model. Therefore, the model cannot predict the stall behavior of the propeller-wing system, discommending it to use the model near the stall of the wing. This is unfortunate as the propeller can postpone the stall of the wing, and the interaction between the propeller and wingtip vortex can be more pronounced [43]. This is, however, not one of the research objectives of this thesis. The increase in viscous drag due to the increased dynamic pressures within the propeller slipstream is also recognized. This should be considered, especially when higher disk loadings of the propeller are considered for different spanwise positions of the propeller. Secondly, the numerical model is based on a SIM, so the propeller is not affected by the wing. This makes the numerical model unsuitable for propeller-wing optimizations but very suitable for this thesis as the computational time of the numerical model is low since no iterations between propeller and wing influences on each other have to be evaluated. Thirdly, as stated previously, no correction for the finite height of the tangential velocities from the propeller, u_z , on the VLM has been implemented. Nederlof [10] has shown that the lack of this correction leads to discrepancies in the lift distribution. This could lead to over-prediction of the amount of swirl recovery thrust by the wing. Furthermore, the effects of the nacelle and thickness of the wing on the performance of the wing are not included in the numerical model. In reality, the nacelle of the propeller significantly influences the performance of the system as it results in a distortion in the wake, for example [44]. Finally, the model does not consider the unsteady behavior of the propeller-wing system. Although the unsteady behavior does result in fluctuations in the lift and drag forces on the wing [45], it is thought that they are more important for studies focusing on the structural aspects of the propeller-wing systems.

The advantage of the numerical model, on the other hand, is highlighted by the fact that the lift, lift-induced drag, and swirl recovery can be analyzed separately for multiple propeller-wing system configurations. The following part uses the numerical model to perform a parametric study. Instead of having a single system lift and drag force, as is the result of the balance measurements in wind tunnel experiments, the induced drag can be decoupled. By this decoupling for different propeller-wing system configurations in the parametric study, a better understanding can be obtained of the coupling and relation between the induced drag components of the wing.



Results & Conclusions

The final part of the thesis first covers the analysis of the propeller-wing system by means of the developed numerical model. A parametric study is performed to understand the coupling and relation between the induced drag components of the propeller-wing system. The results from the analysis are presented in Chapter 7. Hereafter, conclusions from the analyses are given in Chapter 8. From this chapter, it is determined whether the research objective is obtained. Finally, recommendations are made for future research on the aerodynamic interaction between the propeller and wing.

7

Results of a Parametric Study on Propeller-Wing Systems

The numerical model presented in the previous part is used to analyze the aerodynamic performance of propeller-wing system configurations. First, in Section 7.1, a description is given of the characteristics of the propeller and wing that are used in the parametric study. Also, a short explanation is provided of how the results are presented. Then, two important characteristics of the propeller-wing system are analyzed at the start of the chapter. First, the lift-induced drag and swirl recovery of the system are decoupled for multiple spanwise propeller positions in Section 7.2. Hereafter, this is done for the rotational direction of the propeller in Section 7.3. At the end of this section, the spanwise propeller position and rotational direction are varied simultaneously to analyze their combined influence. From these two analyses, another analysis follows in Section 7.4, where the lift distribution of the isolated wing is changed to have a closer look at the influence of the gradient of the spanwise lift distribution. Subsequently, in Section 7.5, the contribution of and interaction between the lift-induced drag and swirl recovery of the wing are considered by increasing the propeller-induced velocities by the velocity multiplication factor (VMF). The last two analyses are on the influence of two important wing planform characteristics. In Sections 7.6 and 7.7, the aspect ratio and taper ratio of the wing are varied to analyze their effect on the lift-induced drag and swirl recovery of the propeller-wing system. Finally, in Section 7.8 the presented results are discussed.

7.1. Setup of the Parametric Study

Before the results of the parametric study on the propeller-wing system are discussed, the setup is defined. The propeller and wing can vary in geometry and can operate at numerous conditions. In Section 7.1.1, the geometry of the propeller and its operating points that are used are presented. The characteristics of the wing that are used in most of the analysis are elaborated on in Section 7.1.2. In Section 7.1.3, an explanation is provided on how the results of the parametric study are presented.

7.1.1. Propeller Operating Point

Willemsen [19] investigated the influence of various operating points of the propeller on the system performance by decreasing and increasing the swirl with a swirl multiplication factor (SMF). This analysis concluded that the net positive swirl recovery increases with the increase of the swirl in the propeller slipstream. The performance of the wing increases with this increase in tangential velocities, but it is shown that the propeller performance decreases as the efficiency of the propeller reduces when more swirl is generated by the propeller, which does not contribute to the production of thrust by the propeller. When the system performance is evaluated by the increase in wing performance and decrease in propeller performance, it was concluded that the swirl increase of the propeller leads to a decrease in the system performance. Therefore, during the analysis, the propeller is operated at the point of maximum efficiency, such that realistic ratios between propeller axial and tangential velocities are obtained within the propeller slipstream.

The XPROP propeller geometry [21] is used for the parametric study. The operating points are chosen such that the BEM model reaches maximum efficiency. This eventually also results in the desired ratio between axial and tangential velocity. In Figure 7.1, the propeller operating points are visualized for five different pitch settings and are stated once more in Table 7.1. The operating points (OP) are numbered from 1 to 5. For each analysis in this chapter, the number of the operating point is stated. Furthermore, the propeller radius is adapted to the radius of the Fokker F-27, which is 1.83 meters [46]. The thrust of OP 1 results in approximately 88% of the thrust needed during the cruise phase of the Fokker F-27. The propeller-induced velocities that follow from the OPs do give a clear representation of the influence of the propeller on the wing. In Section 7.5, the propeller-induced velocities are increased, which mimics higher disk loadings of the propeller, such that the influence of the thrust setting of the propeller can be discussed at the end of the chapter.

Table 7.1: Propeller operating points (OP) for during the analysis.

Operating Point	J [-]	T_c [-]	η [-]	β_{07} [deg]
1	0.9874	0.0710	0.8462	25
2	1.2133	0.0538	0.8655	30
3	1.4643	0.0419	0.8779	35
4	1.7538	0.0328	0.8862	40
5	2.0899	0.0260	0.8914	45

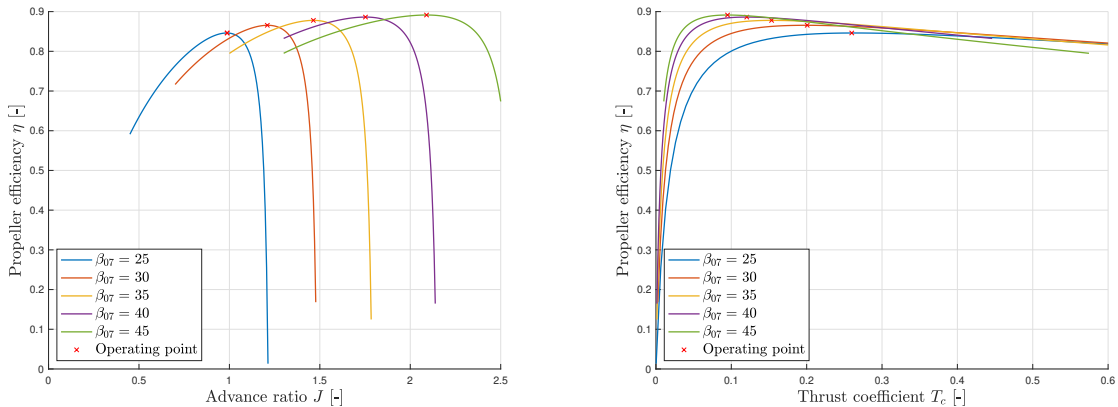
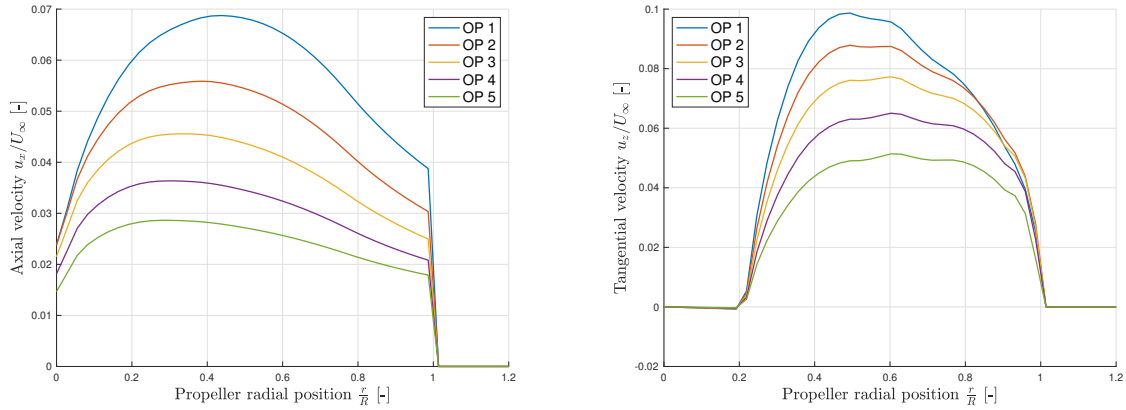


Figure 7.1: Propeller operating points at maximum efficiency in the BEM model.

The propeller-induced velocities following from the slipstream tube model are presented in Figure 7.2. In these figures, results from only one propeller side are visualized. The axial propeller-induced velocities are averaged over the height as is explained in Section 5.1.3. The shape of axial propeller-induced velocity distribution is symmetric over the vertical center of the propeller. In contrast, the tangential velocity distribution is symmetric with respect to the center point of the propeller such that the velocities are negative on the other side of the propeller. The change in the angle of attack of the wing by the propeller-induced velocities is an important characteristic of the slipstream, as it directly influences the amount of swirl recovery of the wing. From these figures, it is seen how the propeller-induced velocities increase with the increase in disk loading. Furthermore, it is noted that the shape of the velocity distributions over the radius of the propeller remains fairly similar.

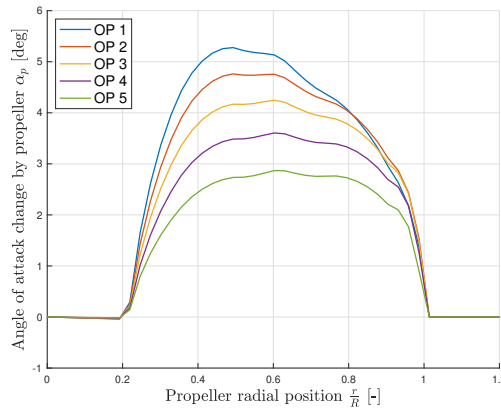
7.1.2. Wing Properties

Unless stated otherwise, a straight wing with a constant chord and an aspect ratio of 9.33 is used in the analysis. This is slightly smaller compared to the aspect ratio of the tapered wing of the Fokker F-27 [46]. Furthermore, a symmetric airfoil is used over the full span of the wing. The distance between the propeller plane and the leading edge of the wing is set to 1.06 meters. The conventional spanwise position of the propeller of the Fokker F-27 is approximately $0.257 b/2$. In some analyses, the configuration with this spanwise propeller position is used as a reference value indicated with the subscript *base*. This is further elaborated on in the next section.



(a) Axial propeller-induced velocities for different operating points.

(b) Tangential propeller-induced velocities for different operating points.



(c) Angle of attack change by the propeller-induced velocities.

Figure 7.2: Propeller-induced velocities and their resulting angle of attack change over the propeller radius.

The propeller slipstream influences the lift and drag of the propeller-wing system. How these parameters are changed depends on the location and rotational direction of the propeller with respect to the wing. The system lift coefficient of the propeller-wing system is fixed at 0.35 during the analysis, such that better insight is obtained into the drag components of the wing during the cruise phase of the aircraft, making the analysis more relevant for aircraft design purposes. The lift coefficient is chosen such that the angle of attack would remain within the range for which the numerical model can be used. The desired system lift coefficient is obtained by changing the angle of attack of the wing. To obtain a lift coefficient of 0.35 for the previously described isolated wing representing the lift of the aircraft during the cruise phase, an angle of attack of 4.22 degrees is needed. During the analysis, it was experienced that with the influence of the propeller slipstream, the angle of attack will not exceed limits such that the numerical model cannot be used anymore.

7.1.3. Presentation of the Results

The definition of the swirl recovery is again highlighted due to its importance during the analyses of the propeller-wing systems in this chapter. As explained in Section 3.2.3, the net swirl recovery is the difference between the thrust resulting from the rotation of the resultant force vector at the wing section behind the up-rotating side of the propeller and the drag of the wing section behind the down-rotating side of the propeller that results by the rotation of the resultant force in the other direction. Swirl recovery is considered a thrust force within this thesis as it is shown that for a wing with an infinite span, it contributes to the thrust of the system by the difference in the lift of the wing sections behind the two propeller sides. The coefficients indicating the contribution of the swirl recovery to the system are $c_{d_{sr}}$

and $C_{D_{sr}}$, which are drag coefficients. Using these drag coefficients instead of thrust coefficients gives the possibility to see the contribution of the lift-induced drag and swirl recovery of the wing to its combined induced drag. Negative drag coefficients below the x -axis contribute to the thrust of the system, and the positive drag coefficients contribute to the drag of the system. However, the net swirl recovery of the system is still considered to contribute to the thrust of the system. Therefore, when it is stated that the net positive swirl recovery of the system increases, the drag of the system decreases, and the negative swirl recovery coefficient increases in magnitude. When the net negative swirl recovery increases, the drag of the system increases, and the swirl recovery coefficient becomes positive. The lift-induced drag is considered a contributor to the drag of the system. The summation of the lift-induced drag and swirl recovery is the induced drag. Therefore, when it is stated that when the lift-induced drag of the wing increases, the combined drag of the system increases. In the remainder of this chapter, this is referred to as combined drag, as the term total drag could lead to misconceptions as other drag contributions are neglected, and the term induced drag could be mixed up with lift-induced drag. Furthermore, the induced drag is referred to as combined drag.

The results from the analyses are scaled by relevant parameters of the propeller-wing system. When the spanwise wing lift distribution of a propeller-wing system is considered, the lift is scaled by the maximum sectional wing lift of the wing without the influence of the propeller slipstream, referred to as the isolated wing. In this case, the isolated wing has the same system lift coefficient as the propeller-wing system. A difference between the angle of attack of the isolated wing and the propeller-wing system achieves this similar system lift coefficient. The spanwise lift and drag coefficients used for the scaling are indicated by the subscript np as 'no propeller' is present for the isolated wing, and max as the maximum value over the span is used. Furthermore, when the lift and drag of the system are considered, the parameters are scaled by the value of the isolated wing, again indicated by the subscript np . Finally, for the analyses in Sections 7.3 and Section 7.6, the system parameters are scaled by those of base configuration indicated with the subscript $base$, which is with the propeller and wing characteristics given in previous sections with an inboard-up rotating propeller.

During the analysis of the propeller-wing system configurations, various spanwise sections are indicated for different sections on the semi-span of the wing. Within this chapter, only the results of the semi-span are presented. The three situations resulting from different spanwise propeller positions are visualized in Figure 7.3. Above each section, a roman number is used to indicate the spanwise section of the wing. In these figures, the lift distribution is shown, but it should be noted that the same indicators are used for the spanwise drag distributions of the wing. Finally, when the gradient of the spanwise lift distribution, dc_l/dy , is mentioned, it is always considered from the root toward the tip of the wing. A decreasing lift from root to tip has a negative gradient of the spanwise lift distribution.

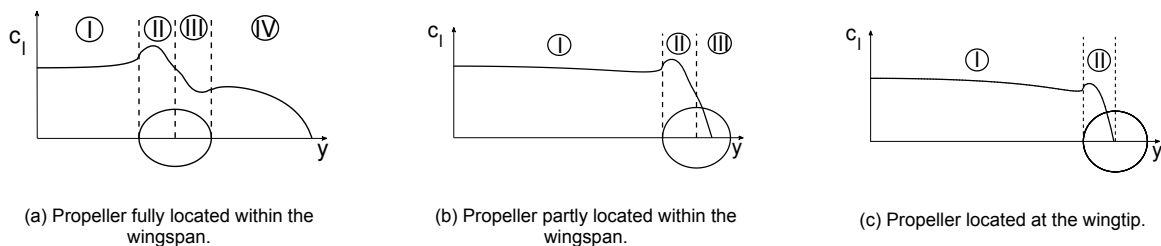


Figure 7.3: Definition of the wing sections for different spanwise propeller positions for the propeller-wing system.

7.2. Drag Decomposition for Spanwise Propeller Positions

In the literature, it is seen that the spanwise position of the propeller has a significant impact on the performance of the propeller-wing system. Within this section, the lift-induced drag and swirl recovery of the wing are decoupled for various spanwise positions of the propeller. This analysis is separated into two parts. First, two different spanwise propeller positions are analyzed to compare the spanwise distribution of lift and drag components. Hereafter, an analysis is presented where the propeller position is varied along the span of the wing, and the change in integral lift and drag is quantified. The section is called system performance, which should not be misunderstood. In this section, the total lift and drag coefficients of the wing are analyzed by the influence of the propeller-induced velocities. The performance of the performance of the propeller is not further looked into.

7.2.1. Spanwise Performance

In Figure 7.4, the lift and decoupled drag components from a propeller-wing system with a propeller at OP 1 located at $y_p = 0.5b/2$ are visualized. The rotational direction of the propeller is such that the inboard side of the propeller is rotating up. This is recognized by the increased spanwise lift coefficient in section II and the decreased lift coefficient in section III. It is seen that peaks are present in the distribution of the lift-induced drag. This follows from single Rethorst correction that has been applied to the non-uniform axial velocity distribution of the propeller, as explained in Section 5.2.2. This discrepancy in the results is recognized but is not further looked into as this does not affect the conclusions that will be made.

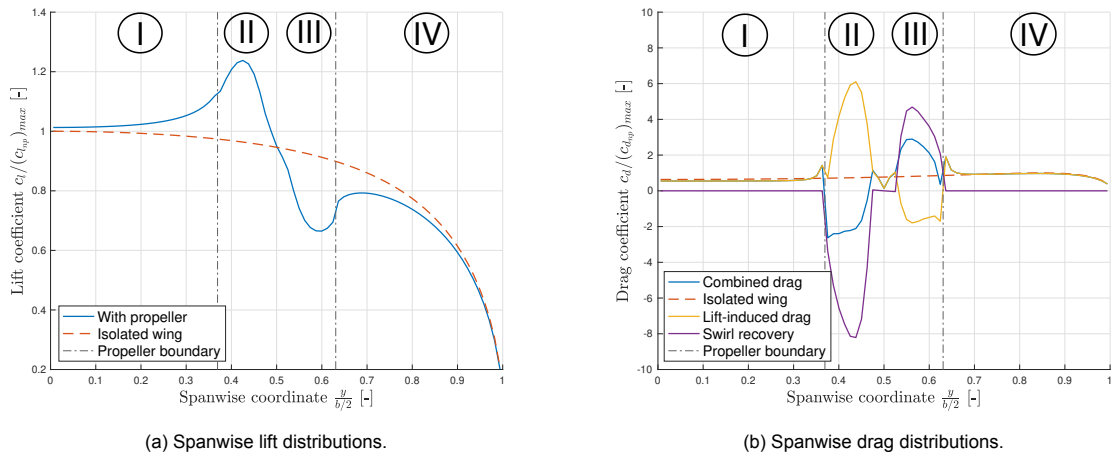


Figure 7.4: Spanwise coefficients for an inboard-up rotating propeller at OP 1 located at $y_p = 0.5b/2$.

In Figure 7.4a, the isolated wing lift distribution is seen by the dashed line. From root to tip, the gradient of the spanwise wing lift distribution, dc_l/dy , over the semi-span of the wing is negative. Within section I and partly within section II, the gradient of the spanwise lift distribution is positive by the influence of the propeller slipstream. Due to this positive gradient, an upwash is experienced over the inboard-wing section, resulting in a reduction of the lift-induced drag compared to the isolated wing as seen in Figure 7.4b. Within section III, local upwash results in a reduction of the lift-induced drag of the system. The local lift-induced drag contribution within section III contributes to the thrust of the system as the lift vector is rotated into the direction of flight. In section IV, it is seen that the opposite happens with a slight increase in the local downwash, such that the local lift-induced drag increases. The strong vortex shedding due to the high gradient of the spanwise lift distribution in the middle behind the propeller causes a downwash in section II and an upwash in section III, resulting in an increase and decrease in lift-induced drag, respectively. It is noted that the contribution of the swirl recovery is only present within the propeller slipstream boundaries. In section II, where the propeller blades rotate upward, the resultant force vector rotates forward, resulting in a negative drag or positive thrust. The opposite happens in section III, where the propeller blades rotate downward. The resultant force vector rotates backward, increasing the local drag of the wing. Furthermore, a significant difference in

the magnitude of the swirl recovery between the two sides is seen. The positive swirl recovery within section II is larger than the negative swirl recovery in section III as they depend on the amount of lift at the respective section, which is explained in Section 3.2.3. The difference in the lift behind the two propeller sides is an important aspect of the propeller wing system due to its influence on the induced drag components of the wing, which is highlighted again further in this section. The combined drag over the span of the wing is an addition of the local lift-induced drag and the swirl recovery. It is noted that viscous effects are left out of consideration during the analysis such that a better understanding can be obtained of the induced drag components of the wing. Within sections I and IV, the combined drag is only determined by the lift-induced drag. In sections II and III, however, the influence of the swirl recovery has a significant influence on the combined drag. The lift-induced drag and swirl recovery are opposite in direction. Still, as the magnitude of the swirl recovery is larger, the combined drag remains largely negative in section II and is increased within section III compared to the isolated wing. The system performance parameters are given in Table 7.2. The drag values of the system are scaled by the drag of the isolated wing, which is its lift-induced drag.

The performance of the previous propeller-wing configuration is compared with those from another configuration where the propeller is mounted at the tip of the wing, i.e., $y_p = b/2$. Since the used model is a SIM, there is no dependency on the propeller position on its performance. Therefore, the propeller-induced velocities in the propeller slipstream, which influence the wing performance, are also unaltered. In Figure 7.5, the spanwise lift and drag coefficients for the propeller-wing system with a tip-mounted propeller are visualized. An increase in sectional lift is present in section II due to the local tangential propeller-induced tangential velocities. As the system lift coefficient is fixed, the lift within section I becomes lower to obtain the design lift coefficient. By this reduction, it is seen that the gradient of spanwise lift distribution over section I has decreased, which results in a lower lift-induced drag at this section. The increased gradient of the spanwise lift distribution within section II, on the other hand, results in increased lift-induced drag. In this propeller-wing configuration, the down-rotating side of the propeller is located outside of the span of the wing. This significantly impacts the net amount of positive swirl recovery to the system as the propeller side where the negative swirl recovery, increasing the drag of the system, is outside the wing span. This increases the net positive swirl recovery of the wing such that the drag of the system decreases. The system performance values of this configuration are compared with those of the previously discussed configuration in Table 7.2. These results show that the lift-induced drag of the configuration with a tip-mounted propeller increases further than that of the center-mounted propeller. The drag decrease by the net increase of positive swirl recovery is larger for the tip-mounted configuration. The lift-induced drag of the center and tip-mounted propellers are increased by 14.5% and 19.7% relative to the drag of the isolated wing, respectively. The drag decrease for the same configurations due to the net positive swirl recovery are -33.8% and 54.9%. Following these differences, two statements are made. First, both configurations benefit from a propeller configured such that the blades on the inboard side are rotating up. The result of this configuration is a reduction in induced drag from the net positive increase in swirl recovery. As this increase of the positive swirl recovery is larger than the increase in the lift-induced drag of both configurations, the combined drag is reduced by the influence of the inboard-up rotating propeller. Second, as the induced drag reduction by the increase in net positive swirl recovery is larger for the tip-mounted propeller, the combined drag of the tip-mounted configuration is lower compared to the configuration with the center-mounted propeller, although the lift-induced drag increase of the system is higher than the center-mounted configuration.

Table 7.2: Propeller-wing system performance results for two different propeller positions.

		Center-mounted	Tip-mounted
Spanwise propeller position	y_p	$0.5b/2$	$b/2$
Lift	$C_L/(C_L)_{np}$	1.00	1.00
Lift-induced drag	$C_{D_{li}}/(C_D)_{np}$	1.145	1.197
Swirl recovery	$C_{D_{sr}}/(C_D)_{np}$	-0.338	-0.549
Combined drag	$C_D/(C_D)_{np}$	0.807	0.648

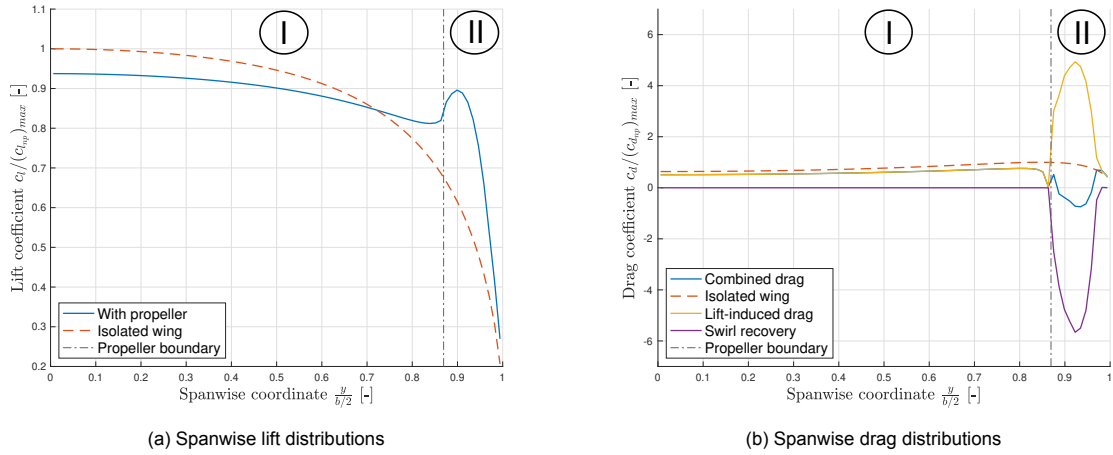


Figure 7.5: Spanwise coefficients for an inboard-up rotating propeller at OP 1 located at $y_p = b/2$.

7.2.2. System Performance

In the previous section, better insight is obtained into the spanwise performance of the wing by the influence of the propeller-induced velocities. With this insight, a more global analysis of the propeller-wing system is conducted by analyzing the system performance for multiple spanwise propeller positions. In Figure 7.6, the decomposition of the combined drag of the propeller-wing system into the lift-induced drag and swirl recovery of the system is presented. First, the results with the propeller at OP 1 in Figure 7.6a are discussed, whereafter they are compared with the same analysis with the propeller at OP 5, which are visualized in Figure 7.6b. The combined drag reduces when the propeller is moved toward the tip of the wing, which is also found in literature as explained in Chapter 3. The net positive swirl recovery increases when the inboard-up rotating propeller is moved toward the tip of the wing. This is clarified by the difference in lift of the wing behind the two sides of the propeller. As is seen in Figure 7.5a, the magnitude of the gradient of the spanwise lift distribution of the isolated wing increases towards the wingtip, and therefore, the difference between the magnitude of swirl recovery at the wing sections behind the two propeller sides increases, thus the net positive swirl recovery increases. The addition of the two drag components results in a decreasing combined drag for a wing where the propeller with inboard-up rotational direction is moved towards the tip because the net positive swirl recovery increases more relative to the lift-induced drag.

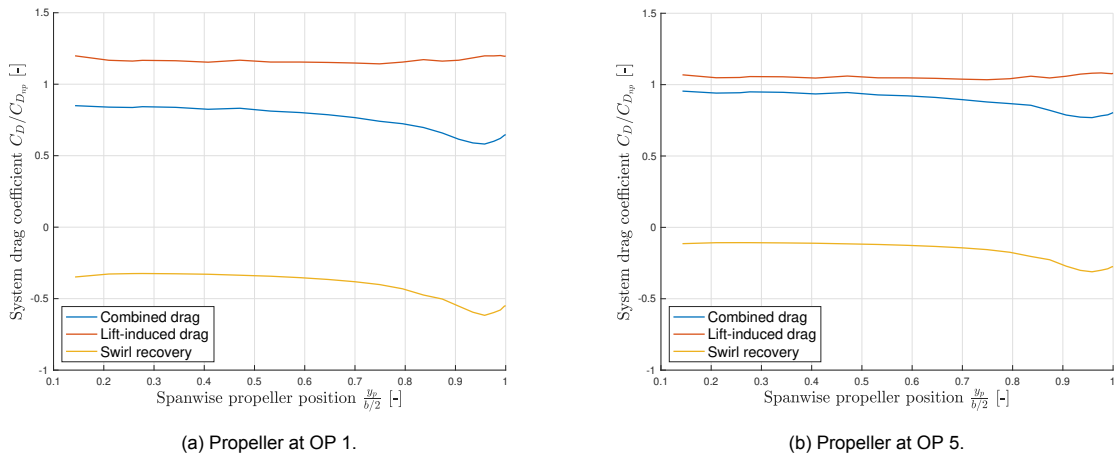


Figure 7.6: Drag decomposition for spanwise positions of an inboard-up rotating propeller.

The increase in net positive swirl recovery in Figure 7.6a does not continue all the way towards the tip of the wing, but a maximum net positive swirl recovery is obtained for a spanwise propeller position of approximately $y_p = 0.95b/2$. This is clarified by taking a closer look at Figure 7.4b, where the

drag contributions of the wing behind the propeller sides are seen. A division between the up- and down-rotating propeller sides is seen, which is the location of the propeller nacelle where the tangential velocity of the propeller is small such that it almost has no influence on the spanwise lift distribution. At the spanwise position where the net positive swirl recovery is highest, not only the influence of the propeller side where the blades are rotating down is outside the span of the wing, but also the propeller side where the blades are rotating up is located more towards the root of the wing, where the lift of the wing is higher. When the propeller is located exactly at the tip, the down-rotating propeller is also outside the span of the wing, but the amount of lift of the wing influencing the net positive swirl recovery of the wing is smaller.

The importance of the gradient of the lift distribution on the net contribution of the swirl recovery thrust of the propeller-wing system is highlighted once more with Figure 7.6a. Comparing the difference of the net positive swirl recovery contributions for propeller positions near the inboard and outboard propeller positions, it is seen that this difference is relatively low for the inboard propeller positions. This has to do with the gradient of the lift distribution of the isolated wing, which is low on the inboard section of the wing compared to the outboard section.

The results obtained with the propeller at OP 1 in Figure 7.6a are compared to Figure 7.6b, where the propeller is set to OP 5, such that the disk loading of the propeller is decreased and the propeller-induced velocities are lower. It is seen that the results take similar shapes, i.e., the induced drag of the system reduces for inboard-up rotating propellers located near the tip of the wing as the contribution of the net positive swirl recovery increases more than the increase of the lift-induced drag of the system. However, the amount of drag reduction with the propeller at OP 5 is significantly less compared to those where the disk loading of the propeller is higher, and thus the induced velocities are higher. The maximum drag reduction by the influence of the propeller with respect to the isolated wing at OP 1 is 41.9%, whereas this reduction is 23.1% with the propeller at OP 5. The maximum drag reductions of the wing by the influence of the propeller-induced velocities for all OPs are given in Table 7.3. The drag reduction of the wing increases when the disk loading of the propeller is higher. This is reasoned by the fact that the higher disk loading results in higher tangential velocity in the propeller slipstream, such that the net positive swirl recovery is more significant. The drag reduction with respect to the propeller thrust is provided in the same table. In this case, the propeller thrust is the thrust by the two propellers influencing the performance of the wing. In this column, a different trend is recognized as the drag reduction is more prominent when the thrust of the propeller is lower. The differences in the relative drag reduction are much lower for the different OPs. These results are in line with the conclusion from Willemsen [19]. The propeller efficiency is lower for the OPs with higher disk loading, as seen in Figure 7.1. Therefore, more swirl is present relative to the amount of thrust produced by the propeller for higher disk loadings. However, this energy loss in the swirl of the propeller is not fully recovered by a net positive swirl recovery of the wing.

Table 7.3: Maximum drag reduction obtained with the inboard-up rotating propeller for different OPs.

Operating point	Drag reduction	
	w.r.t. isolated wing C_{Dnp} [%]	w.r.t. propeller thrust T [%]
1	41.9	3.97
2	39.4	4.92
3	35.3	5.66
4	30.0	6.16
5	23.1	5.98

Furthermore, in the literature on propeller-wing systems, optimized wing lift distributions have been shown for inboard-up rotating propellers at the tip. Miranda and Brennan [22] presented results for various lift distributions, as seen in Figure 3.5. The optimized spanwise wing lift distribution has an increased loading at the tip compared to an elliptic lift distribution. With the previously shown decoupling of the lift-induced drag and swirl recovery, it is possible to reason why better performance follows from this spanwise lift distribution with increased tip loading. The optimized spanwise lift distribution shows

an increased gradient of the spanwise lift distribution at the tip. This increased gradient of the spanwise lift distribution increases the net positive swirl recovery, which is dominant over the increase of the lift-induced drag of the wing by this change in spanwise lift distribution.

7.3. Drag Decomposition for Propeller Rotational Directions

Another influential characteristic of the propeller-wing system is the rotational direction of the propeller. As seen from the previous section, the influence of the propeller is the largest when it is placed near the tip of the wing. For this reason, the influence of the rotational direction on the spanwise lift-induced drag and swirl recovery distributions is analyzed for a tip-mounted propeller configuration. The section has a similar buildup to the previous one. First, the influence of the rotational directions is seen on the spanwise distribution of the aerodynamic characteristics, whereafter the system characteristics for multiple spanwise positions analyze the influence of the rotational direction.

7.3.1. Spanwise Performance

In Figure 7.7, the spanwise lift and drag distributions of the wing are visualized for a tip-mounted propeller at OP 2. Comparing the previous analysis with a lower disk loading gives the possibility to check whether the swirl recovery still dominates over the lift-induced drag. The left figure shows the difference between the lift distributions of the inboard-up and inboard-down rotating propellers. The integral of each of these lift distributions results in a system lift coefficient of 0.35. The difference in lift is obtained by varying the angle of attack of the wing. By the increase in lift within section II due to the inboard-up propeller configuration, the lift within section I is lower and flattened out. The opposite happens for the inboard-down configuration.

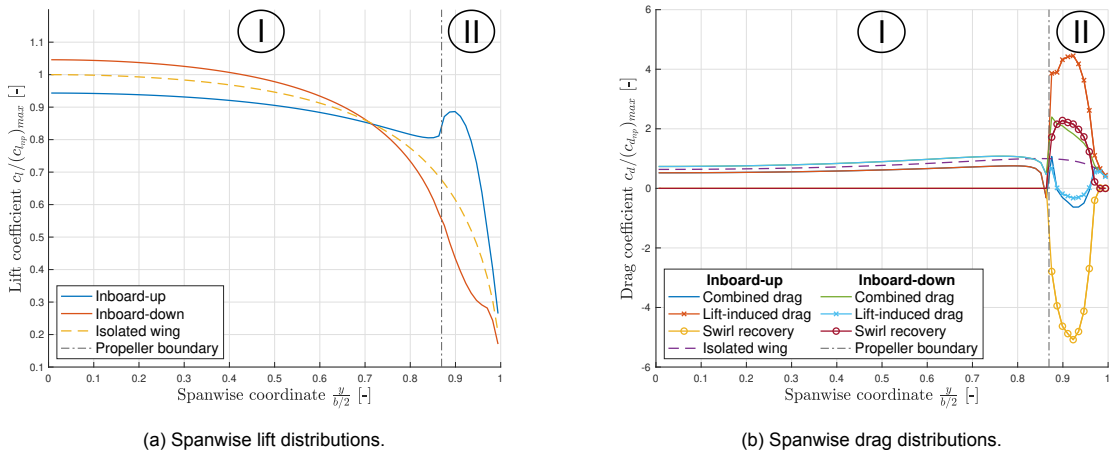


Figure 7.7: Spanwise coefficients for a propeller at OP 2 located at $y_p = b/2$.

The lift-induced drag within section I is directly related to the lift distributions. The decreased gradient of the lift distribution over section I by the inboard-up propeller configuration results in a lower lift-induced drag compared to the isolated wing. The gradient of the spanwise wing lift distribution has increased in magnitude for the inboard-down configuration, such that the lift-induced drag is increased compared to the isolated wing. In literature [7], it is stated that the wingtip vortex has moved inboard as the high gradient of the spanwise wing lift distribution has moved inboard. Without the consideration of section II, the reduction of the effective aspect ratio of the wing is seen as the lift-induced drag has increased within section I. Within section II, it is seen that the contribution of the lift-induced drag and swirl recovery to the combined drag are positive and negative, respectively. These forces are inverted for the inboard-down propeller configuration, such that the lift-induced drag reduces the combined drag and the positive swirl recovery increases it. Another difference between the two configurations is recognized in the magnitude of the lift-induced drag and swirl recovery. The lift-induced drag from the configuration with an inboard-down rotating propeller becomes almost zero within section II. As the contribution of the negative swirl recovery is increasing the drag for this configuration, the combined drag within section II becomes positive. For the configuration with an inboard-up rotating propeller, however, the contribution

of the lift-induced drag has increased with respect to that of the isolated wing. The net swirl recovery, which is a negative, such that the drag of the system increases, is larger in this case as the lift at section II is larger compared to the configuration where the propeller is rotating inboard-down. Although the absolute magnitude of the swirl recovery reduces when the propeller has an inboard-down configuration by the reduction of lift at the wing section behind the propeller where the blades are rotating down, the lift-induced drag remains high as there remains vorticity in the wake due to the production of lift. This is further clarified using the system performance values presented in Table 7.4. The lift-induced drag of the inboard-down configuration decreased by 34.9% relative to the drag of the isolated wing, whereas it increased by 23.3% for the inboard-up configuration. As seen in the previous analysis, the influence of swirl recovery is dominant on the combined drag of the system. The net contribution of the negative swirl recovery of the inboard-down configuration contributes to the combined drag as is seen by the contribution of 23.3%. The net contribution of the positive swirl recovery of the inboard-up configuration reduces the combined drag of the system as seen by the -55.8% relative to the drag of the isolated wing. It is noted that the net positive swirl recovery of the inboard-up configuration is over twice as high compared net negative swirl recovery of the inboard-down configuration. This can be clarified by the increased and decreased lift within section II of the wing by the influence of the rotational direction of the propeller.

Table 7.4: System performance of inboard-up and inboard-down rotating propellers mounted at the tip of the wing.

		Inboard-down	Inboard-up
Spanwise propeller position	y_p	$b/2$	$b/2$
Lift	$C_L/(C_L)_{np}$	1.00	1.00
Lift-induced drag	$C_{D_{li}}/(C_D)_{np}$	0.994	1.186
Swirl recovery	$C_{D_{sr}}/(C_D)_{np}$	0.233	-0.558
Combined drag	$C_D/(C_D)_{np}$	1.233	0.651

7.3.2. System Performance

As more insight is obtained into the influence of the spanwise position and rotational direction of the propeller, an analysis with both of these characteristics is performed. In Figure 7.8, the spanwise position and rotational direction of the propeller are varied, such that their influence on the combined drag of the system can be analyzed. On the left, the system parameters of the wing with inboard-down propellers are visualized. On the other side, the inboard-up configurations are visualized. Furthermore, this is done for three different OPs as they result in different velocity profiles within the propeller slipstream. On the vertical axis, the lift-to-drag ratio, L/D , is taken relative to the baseline configuration. In this baseline configuration, the propeller is rotating inboard-up and is located at $y_p/b/2 = 0.2$. The configurations with different OPs are scaled by the configuration with the same OP at the spanwise position of the baseline configuration. This is seen in the figure on the inboard-up side as all three lines go through the point of the spanwise baseline propeller position and one for the scaled lift-to-drag ratio.

The previously discussed effects from the rotational direction of the propeller on the propeller-wing system configuration are expanded with higher propeller loadings, as higher axial and tangential velocities are induced by the propeller. This is seen by the peak values of the lift-to-drag ratio in Figure 7.8. Comparing the configurations with the propeller at OP 1, it is seen that the peak for the inboard-up configuration reaches 1.44 times the base value, and the inboard-down configuration comes down to a fraction of 0.65. The difference between the inboard-up maximum and the inboard-down minimum is 0.79 times the base value. The same is done for the configurations with the propeller at OP 5, which results in a difference between the maximum and minimum values of 0.43 times the base value. These differences obtained by variation of rotational direction and OPs are clarified by means of a decomposition of the lift-induced drag and swirl recovery. In Figure 7.9, the decomposition of drag components for the OPs 1 and 5 is seen. In this figure, the drag values are scaled by the combined drag of the inboard-up configuration at the base position of $y_p = 0.2b/2$. By taking a closer look towards the inboard-down configurations on the left of the figure, it is seen that the values of the drag components move towards each other when the propeller is moved towards the tip, whereas the inboard-up configurations approximately keep the same difference between drag components for the spanwise locations

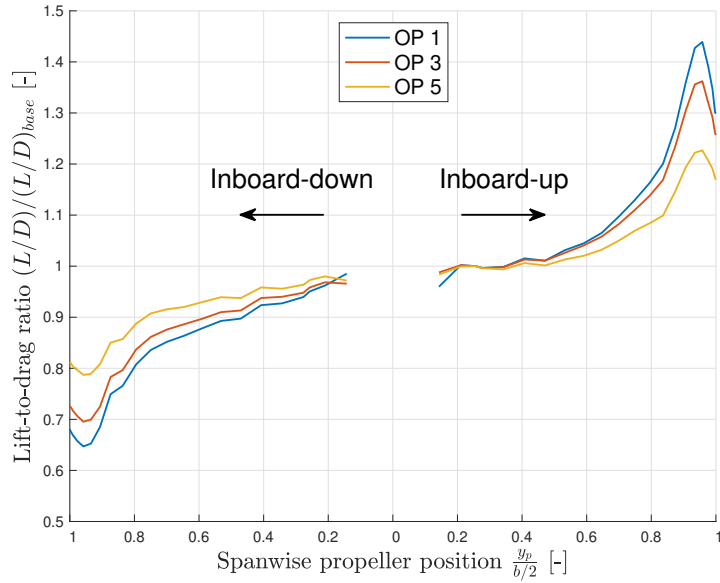


Figure 7.8: Lift-to-drag ratios with respect to the baseline configuration with different operating points.

of the propeller. This difference is clarified by recalling the difference between the lift distributions of the two configurations as visualized in Figure 7.10. Comparing lift distributions of the inboard-up and down configurations with different operating points, it is seen that the difference between the lift in section II is larger for the inboard-up configuration. The swirl recovery is directly related to the lift within section II for tip-mounted propellers. For the inboard-down configuration, the lift at the section is low such that the swirl recovery does not have a significant influence on the combined drag of the system anymore. This is compared to the inboard-up propeller configuration. The lift within section II increases proportionally to the increase of the thrust production of the propeller. With this increased lift, the contribution of the net positive swirl recovery remains large as well.

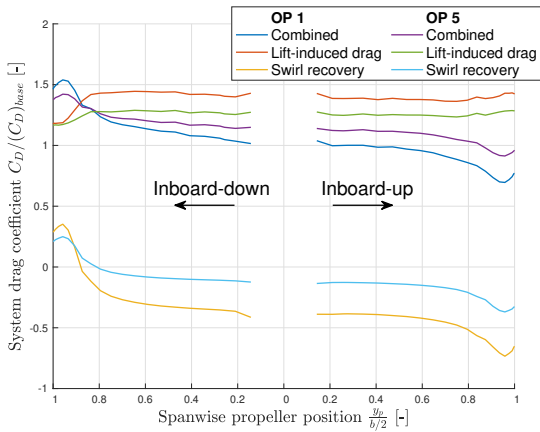


Figure 7.9: Drag decomposition for inboard-down and inboard-up rotating propellers at various spanwise positions at OPs 1 and 5.

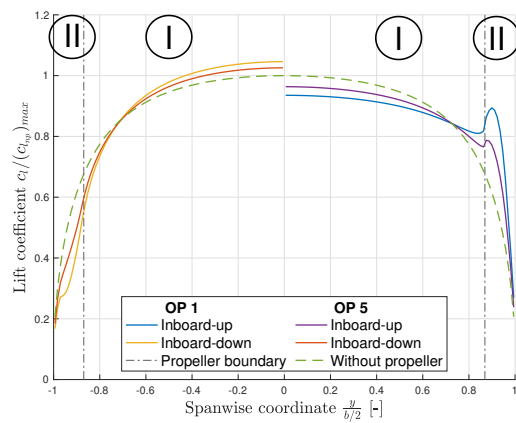


Figure 7.10: Lift distributions for inboard-up and inboard-down rotating propellers at the tip for OPs 1 and 5.

7.4. Variation of the Spanwise Lift Distribution

To emphasize the importance of the spanwise lift distribution of the isolated wing for propeller-wing systems, the wing twist is changed to obtain new lift distribution. Over the semi-span of the wing, the wing is twisted with $\theta(y) = 5 \sin(2\pi y/b)$, such that the maximum of 5 degrees twist is obtained halfway through the wing. With this twist, a lift distribution is obtained where the gradient of the spanwise lift distribution is roughly equal in magnitude but opposite in sign on both sides of the wing with semi-span. The increase in spanwise lift over the wing section near the root of the wing could follow from the presence of a fuselage [47]. Furthermore, with this twist, the angle of attack of the propeller-wing systems does not become higher than six degrees in order to obtain a system lift coefficient of 0.35.

The spanwise lift distributions of the isolated wing and wing with inboard-down and inboard-up rotating propellers located at $y_p = 0.25b/2$ are presented in Figure 7.11a. Important to note is the increase in lift from the root toward the center of the isolated wing, resulting in a positive gradient of the spanwise lift distribution. At the outboard side of the isolated wing, the gradient of the spanwise lift distribution is negative, which is similar to the lift distributions of the previous wings. The wing section with the negative gradient of the spanwise lift distribution of the isolated wing is indicated by a gray color. Furthermore, it is seen that the inboard side of the propeller is located in front of a wing section with a lower sectional lift than the outboard side. The corresponding drag distributions to the lift distributions are presented in Figure 7.11b. The system coefficients are seen in Table 7.5 and are scaled with the drag coefficient of the isolated wing. From the results provided by the table, two things can be noted. First, it is recognized that the combined drag of both of the systems is reduced with respect to the isolated wing. Furthermore, it is seen that both configurations have a net positive swirl recovery such that the combined drag of the wing is reduced. The inboard-down configuration has a higher net swirl recovery thrust when compared to the inboard-up configuration. This is clarified by the gradient of the lift distribution of the isolated wing. The gradient at the location of the propeller is positive, such that behind the inboard side of the propeller, the lift of the wing is less compared to the lift behind the outboard side of the propeller. At this propeller location, this difference in lift of the wing behind the two propeller sides is further increased by the inboard-down configuration. The difference in lift between these two sections directly relates to the net swirl recovery force of the wing as is explained in Section 3.2.3. For this reason, the contribution of the net positive swirl recovery to the reduction of combined drag is larger for the inboard-down configuration. The difference in the lift of the wing behind the two propeller sides in the inboard-up configuration is less, such that the net swirl recovery is lower compared to the inboard-down configuration. The lift-induced drag of the inboard-up configuration, on the other hand, is reduced compared to the inboard-down configuration. This can be clarified by the increased gradient of the spanwise lift over the inboard wing section, which is directly related to the amount of lift-induced drag. From these results, it can be concluded that for the design of propeller-wing systems, the difference in lift of the wing sections behind the two propeller sides must not only be maximized to obtain a high net swirl recovery thrust. When the difference in lift becomes too large, the lift-induced drag resulting from the increased gradient of the spanwise wing lift distribution becomes larger than the net contribution of the swirl recovery thrust by the wing. Therefore, the dominance of the contribution of the net swirl recovery thrust is dependent on the swirl within the propeller slipstream.

Table 7.5: System performance of a twisted wing with inboard-up and inboard-down rotating propellers mounted at $y_p = 0.25b/2$.

		Inboard-down	Inboard-up
Spanwise propeller position	y_p	$0.25b/2$	$0.25b/2$
Lift	$C_L/(C_L)_{np}$	1.00	1.00
Lift-induced drag	$C_{D_{ii}}/(C_D)_{np}$	1.286	1.020
Swirl recovery drag	$C_{D_{sr}}/(C_D)_{np}$	-0.388	-0.163
Combined drag	$C_D/(C_D)_{np}$	0.898	0.878

The same analysis is conducted for all the spanwise positions of the inboard-up and inboard-down propellers. Also, the same isolated wing lift distribution is used, with the positive gradient of the spanwise lift distribution on the inboard, and the negative gradient on the outboard. The system drag coefficients for all spanwise positions of the propeller are presented in Figure 7.12. The wing section with the neg-

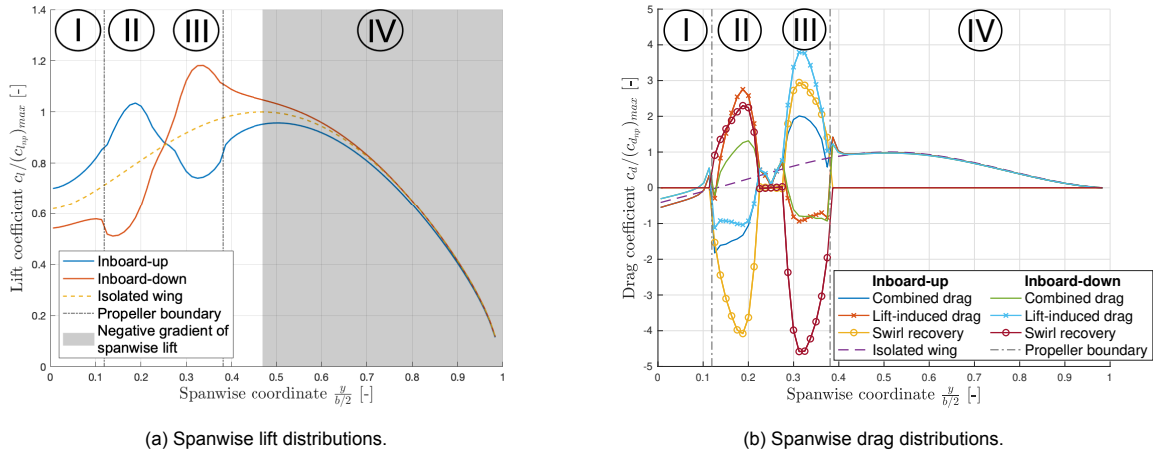


Figure 7.11: Spanwise performance of the wing with twist with propellers at OP 1 at $y_p = 0.25b/2$.

ative spanwise wing lift distribution from root to tip is again indicated by the gray area. The combined drag distributions for both configurations show very similar trends to those from Section 7.3 due to the previously described influence of the lift-induced drag. The amount of swirl recovery is the most interesting part of this figure. Within the white area, where the lift is increasing from root to tip, the net positive swirl recovery of the inboard-down configuration is higher compared to the the net positive swirl recovery of the inboard-up configuration. The gradient of the isolated wing lift distribution influences the amount of swirl recovery that is obtained by the wing. A closer look is taken toward the propeller position located exactly at the peak of the lift distribution of the isolated wing such that $y_p = 0.47b/2$. This location is the intersection of the white and gray areas. At these boundaries, the net positive contribution of swirl recovery to the reduction of the combined drag is the same. For this specific propeller position, the amount of lift of the wing sections behind both sides of the propeller is similar, such that it does not matter in which direction the propeller rotates to obtain the same amount of net positive swirl recovery.

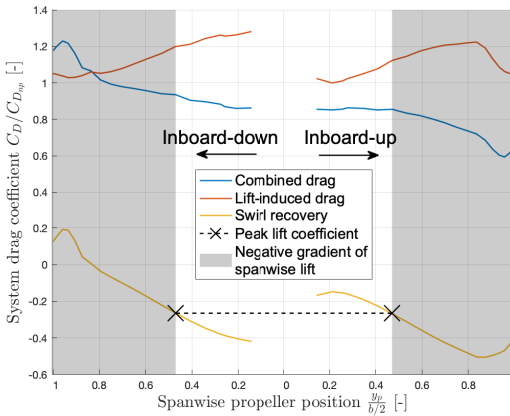


Figure 7.12: System drag decomposition for inboard-up and inboard-down rotating propellers at OP 1.

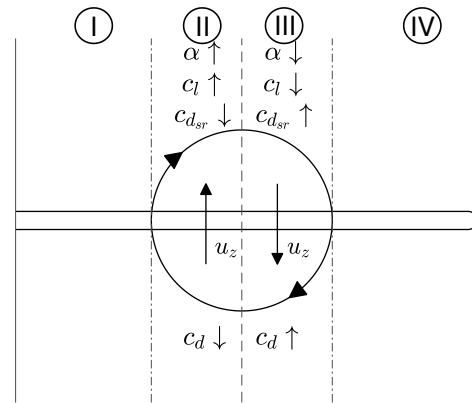


Figure 7.13: Local change of angle of attack influencing the local spanwise coefficients.

From Figure 7.12, another aspect of the contribution of the net positive swirl recovery is highlighted. At the boundary between the positive and negative gradient of the isolated wing lift distribution, both configurations have a net positive swirl recovery reducing the combined drag of the system. This follows from the fact that the lift is increased on the side where the propeller is moving up, and on the other side, the lift is decreased. The swirl recovery directly depends on the amount of lift behind the propeller side. This is schematically visualized in Figure 7.13. On the left side, the propeller is rotating up, increasing

the angle of attack and therefore increasing the lift. This decoupled effect is previously discussed by literature and seen in Figure 3.2b. By the increase in the angle of attack, the lift vector rotates forward, decreasing the negative net contribution of the swirl recovery such that the combined drag reduces. The opposite result is present on the side where the propeller is rotating down. Hypothetically speaking, when a wing would have a constant spanwise lift with an infinitely strong wingtip vortex, a conventionally located propeller would always result in net positive swirl recovery as the forward-rotated lift vector is larger compared to the backward-rotated lift vector. Furthermore, the amount of net positive swirl recovery would be independent of the rotational direction as the lift gradient of the isolated wing lift distribution is zero.

Part I has presented various literature on propeller-wing systems. Many studies conclude the benefits of placing the inboard-up rotating propeller at the wingtip. The previous analysis shows that this does not necessarily have to result in the configuration with the best aerodynamic properties. From an aerodynamic point of view, the placement of the propeller resulting in the best performance of the propeller-wing system is heavily dependent on the gradient of the spanwise lift distribution of the isolated wing as this determines the amount of net contribution of the swirl recovery that can be obtained by the wing.

7.5. Dominating Induced Drag Component

In the previous analysis, the influence of the difference between the lift of the wing sections behind the propeller is analyzed. The lift-induced drag of the wing increases by increasing this lift difference between the two wing sections. The net positive swirl recovery contribution, however, has increased by the same difference in lift of the wing sections behind the propeller. In all previous sections, it is recognized that the contribution of the swirl recovery dominates the combined induced drag of the system. Therefore, another analysis is conducted on the propeller-wing system to investigate the dominance of the net positive swirl recovery contribution to the induced drag of the wing.

In this analysis, an arbitrary propeller slipstream is used. The axial propeller-induced velocity within the slipstream remains zero, and the swirl of the propeller is varied. A simplified swirl, as has also been used by Nederlof [10] to show the contribution of the swirl to the increase in sectional lift, is used to investigate the dominance between the induced drag components of the wing. Within the propeller slipstream, tangential propeller-induced velocities are determined by Equation 7.1 such that at the inboard side, the tangential velocity is positive, representing an inboard-up rotating propeller configuration. An example of the tangential velocity distribution with the maximum velocity of $u_{z_{amp}} = 0.25U_{\infty}$ over the semi-span of the wing is visualized in Figure 7.14a. Furthermore, the spanwise wing lift distribution following from these tangential velocities in the propeller slipstream is visualized in Figure 7.14b. Comparing this spanwise lift distribution with the spanwise lift distribution following from the induced velocities from the propeller at OP 1 as is visualized in Figure 7.4a, it is noted that the difference in the lift of the wing sections behind the two propeller sides is already increased by the change in the tangential velocities within the propeller slipstream. This lift difference increases further by increasing $u_{z_{amp}}$.

$$u_z = -u_{z_{amp}} \sin\left(\frac{2\pi r}{2R}\right) \quad (7.1)$$

Figure 7.15 presents the change in induced drag from the variation of the amplitude of the tangential velocity in the propeller slipstream. The amount of lift-induced drag and net positive swirl recovery contribution are changed by the increase of the tangential velocity within the slipstream. Important to note is the different trends of the contributors to the induced drag of the system. The increase of lift-induced drag of the system increases by an exponential trend, whereas, for the contribution of the net positive swirl recovery, this is only the case for the very low tangential velocities. In this analysis, the amount of net positive swirl recovery contribution increases linearly with the tangential velocities within the propeller slipstream. The effect of these trends on the combined induced drag of the system is that for some amount of tangential velocity, the combined induced drag reaches a minimum, as visualized by the red cross in the figure. At this point, the maximum swirl is 1.36 times the freestream velocity. This amount of swirl in the propeller slipstream may be unrealistically high, making it impossible to reach the point where the lift-induced drag starts to dominate the combined induced drag, which is

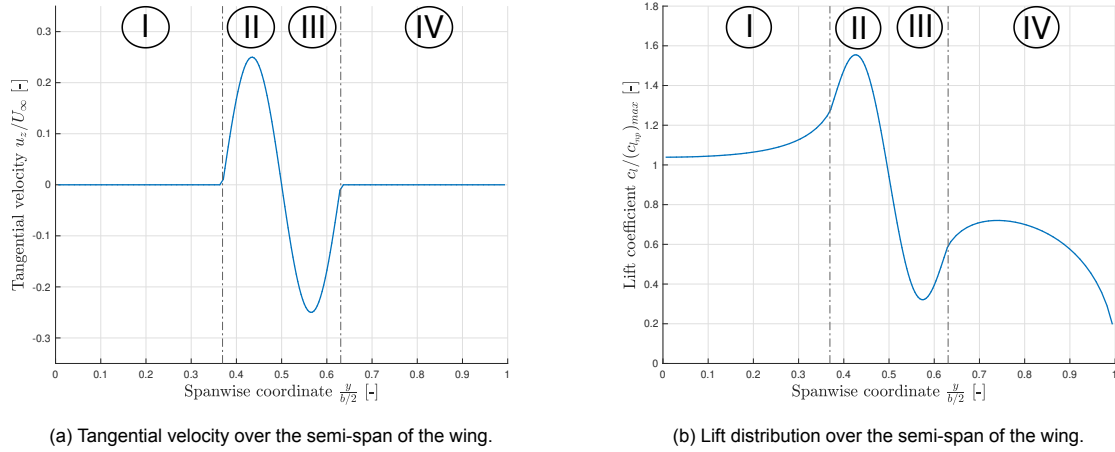


Figure 7.14: Spanwise velocity and lift by the arbitrary tangential velocity with $u_{z_{amp}} = 0.25U_{\infty}$.

when the combined drag of the propeller-wing systems becomes larger than the lift-induced drag of the isolated wing as the wing does not benefit from the propeller-induced velocities anymore. Furthermore, it is seen that the fraction of the drag components increases to very large numbers. This could result from the sine function used to construct the tangential velocity within the propeller slipstream. For this reason, a similar analysis is conducted where more realistic propeller slipstreams are used. For this reason, another similar analysis is conducted where the axial propeller-induced velocity is included.

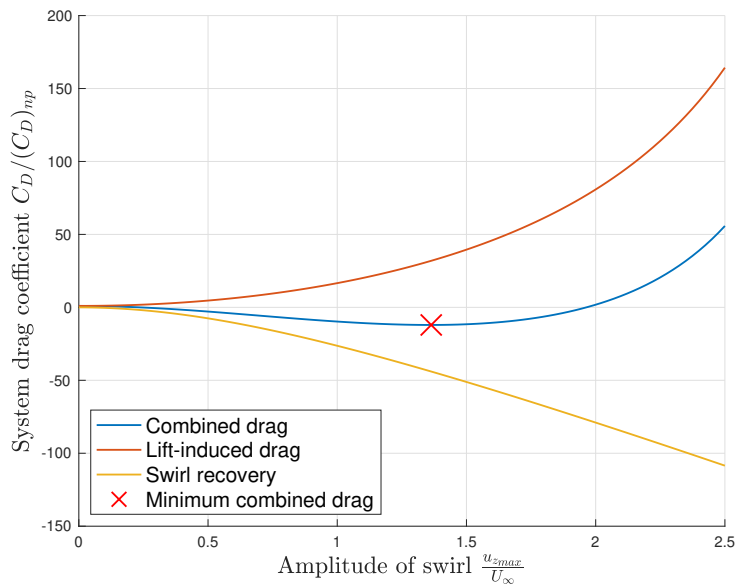


Figure 7.15: System drag decomposition by the arbitrary tangential velocity.

As described at the beginning of the section, the axial propeller-induced velocity is set to zero in the previous analysis. However, the influence of this velocity component within the propeller slipstream is known as it has been explained by Figure 3.2a. Including axial velocity within the slipstream results in a higher difference in net positive swirl recovery of the wing sections behind the two propeller sides for lower tangential velocities. The results of similar analyses are visualized in Figure 7.16. The axial and tangential induced velocities from the propeller at OP 1 are multiplied by the velocity multiplication factor (VMF). As seen in Figure 7.2, the axial and tangential velocities behave proportionally to the disk loading. Higher disk loadings could be mimicked by applying the VMF to the propeller-induced velocities. In Figures 7.16a and b, the breakdowns for different VMFs are visualized for a center and tip-mounted propeller, respectively. The combined induced drag of both configurations is compared in Figure 7.16c.

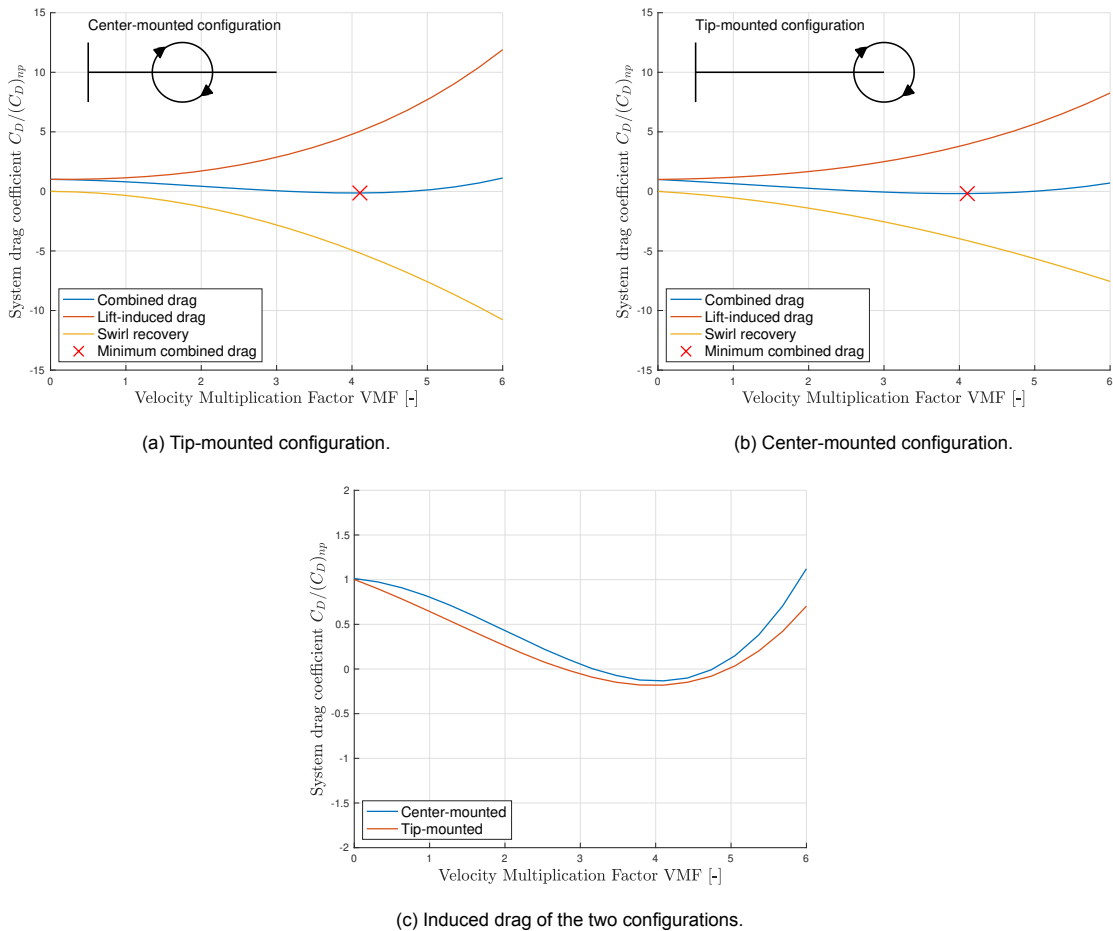


Figure 7.16: System drag decompositions for the systems with propeller-induced velocities increased by the velocity multiplication factor (VMF).

From these results, two points should be highlighted for each figure. First, it is seen that for higher disk loadings, the lift-induced drag starts to dominate the combined induced drag of the system. This point is where the combined induced drag of the propeller-wing system becomes larger than the lift-induced drag of the isolated wing. For the center-mounted propeller, this is with a VMF of 5.9, and for the tip-mounted propeller this is with a VMF of 6.2. For these disk loadings, the performance of the wing does not increase by the influence of the propeller. Second, the situations where the propeller-induced velocities are such that a minimum combined induced drag is obtained should also be highlighted. At this point, which is similar for both configurations, the VMF is 4.1. The spanwise wing lift distribution is such that an optimum is achieved between the gradient of the spanwise wing lift distribution, increasing the lift-induced drag, and the difference in lift between the two wing sections behind the two propeller sides, increasing the net positive swirl recovery contribution. Figure 7.16c shows the combined induced drag for both configurations. Following the literature on propeller-wing systems, the combined induced drag of the tip-mounted configuration is lower. It should be noted that the VMF could result in unrealistically high propeller-induced velocities. As the objective of the thesis is mainly the investigation of the relative contribution of the lift-induced drag and swirl recovery, these velocities are not further looked into.

Finally, it is concluded that both axial and tangential propeller-induced velocities significantly impact the net positive swirl recovery contribution to the system. Also, the importance of the Rethorst correction within the numerical model is underlined by this statement, as the correction reduces the gradient of the spanwise wing lift distribution by the influence of the axial propeller-induced velocities in the propeller slipstream. Additionally, the results are of value for aircraft design as this analysis method could provide a way to obtain the minimum combined induced drag of the propeller-wing system. The results show

the relative contribution of the lift-induced drag and swirl recovery to the induced drag of the propeller-wing system. The VMF on the x-axis of the figure can be seen as the thrust setting of the propeller. The spanwise wing lift distribution should be designed such that, in combination with the thrust setting of the aircraft during the cruise phase, it results in the minimum induced drag.

7.6. Variation of the Aspect Ratio of the Wing

In Section 3.2.2, the influence of the aspect ratio of the isolated wing on the lift-induced drag is emphasized. In this section, an analysis is presented to obtain better insight into the influence of the aspect ratio on the lift-induced drag and swirl recovery of the propeller-wing system, whereafter the behavior of the combined drag is clarified. Within this analysis, the size of the inboard-up rotating propeller is kept the same for every aspect ratio, meaning that for larger aspect ratios, less of the span of the wing is located within the slipstream of the propeller. The chord and span of the wing are changed such that the surface area of the wing is kept constant.

Figure 7.17 shows the drag decomposition for wing platforms with increasing aspect ratio. As expected from the relation between the lift-induced drag and the aspect ratio of the isolated wing, the lift-induced drag of the propeller-wing system also reduces with increasing aspect ratio. The net positive swirl recovery contribution also reduces with the increasing aspect ratio but at a much lower rate than the lift-induced drag rate. To clarify these trends, a closer look is taken towards the lift distributions of the wing for aspect ratios of 9.33 and 18.67, which are visualized in Figure 7.18a. The system lift coefficients of the two propeller-wing systems are again kept the same at 0.35.

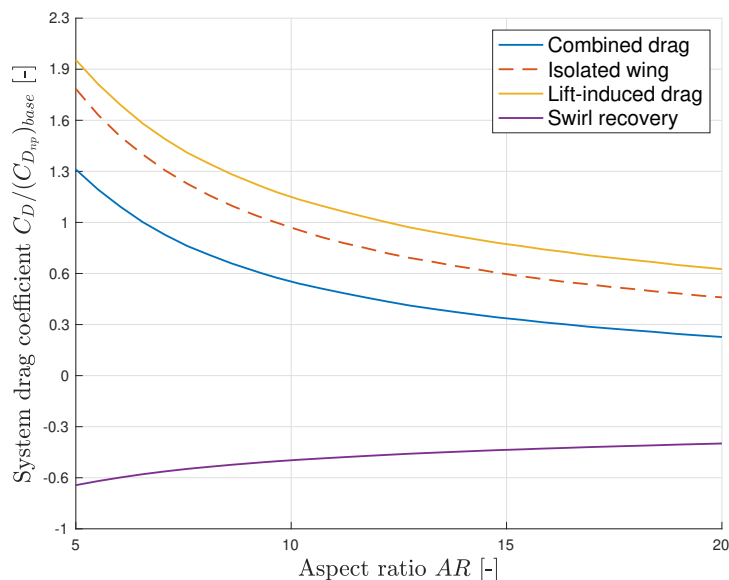


Figure 7.17: System drag decomposition for aspect ratios of the wing with a tip-mounted propeller at OP 1.

Comparing the spanwise lift distributions of the two propeller-wing systems, it is seen that for a higher aspect ratio, the difference between lift within sections I and II is relatively high compared to the lift for a lower aspect ratio. The larger difference in lift between sections I and II comes with an increased gradient in the wing lift distribution near the tip, such that a small increase in lift-induced drag is observed. The increased lift within section II for the larger aspect ratio also influences the net positive swirl recovery obtained within this section. As is seen in Figure 7.18b, the swirl recovery increases by a larger amount compared to the lift-induced drag. For this reason, it is seen that in Figure 7.17, the net positive swirl recovery contribution is moving more gradually towards the asymptote zero compared to the lift-induced drag of the wing. For the increasing aspect ratio, the influence of the contribution of the net positive swirl recovery is dominant over that of the lift-induced drag on the induced drag of the wing. Following the conclusions made in the previous section, it should be noted that the dominance of the contribution of the net positive swirl recovery is also dependent on the disk loading of the propeller.

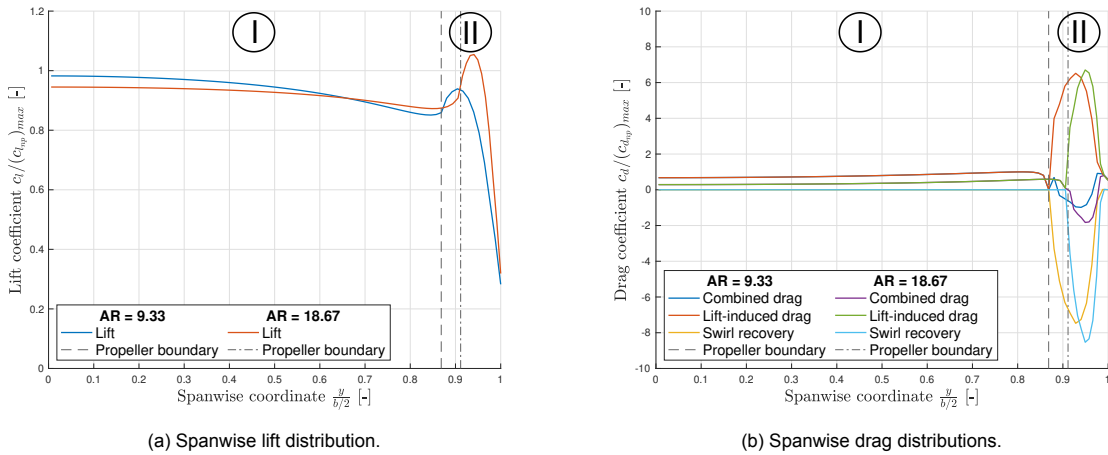


Figure 7.18: Spanwise coefficients scaled by the maximum values of the isolated wing with AR of 9.33 for a tip-mounted propeller at OP 1 for wings with aspect ratios of 9.33 and 18.67.

7.7. Variation of the Taper Ratio of the Wing

In this section, an analysis of the influence of the taper ratio on the lift-induced drag and swirl recovery of the wing is conducted. The taper of the wing is included such that the surface area and span of the wing remain the same as those described in Section 7.1.2. Furthermore, the wing remains straight, so the sweep of the leading and trailing edges is equal and opposite. A taper ratio, λ , of 1.0 and 0.2 are compared within the analysis. This taper ratio is high compared to the ratio from the Fokker F27. The large ratio is used to see better the difference in the effect of taper on the lift-induced drag and swirl recovery. As the taper ratio results in a variable chord over the span of the wing, the spanwise lift coefficient is not used for the lift distribution. Instead, the lift distribution is based on the lift per unit span as seen in Figure 7.19a. It is seen that the spanwise gradient of the lift distribution is higher when a taper ratio is applied to the wing. With this difference in mind, the propeller slipstream is added to the system.

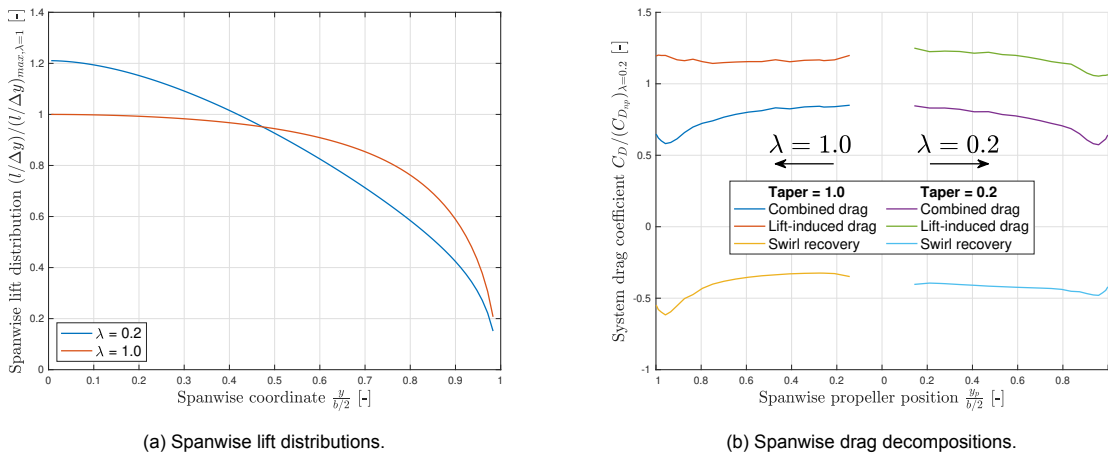


Figure 7.19: Lift distributions and drag decompositions of the wing with taper ratios of 1.0 and 0.2 with propeller at OP 1.

In Figure 7.19b, the drag decomposition for various spanwise propeller positions with inboard-up configuration is presented. All values are scaled by the drag coefficient of the isolated wing with a taper ratio of 0.2. The shape of the drag decomposition of the wing without taper is the same as the one presented in Figure 7.6a. Comparing the combined drag of both propeller-wing system configurations, a similar outcome is seen for the various spanwise propeller positions. More variation between the two configurations is seen when the lift-induced drag and net swirl recovery are compared. First, it is seen

that the net positive swirl recovery contribution of the tapered wing is more constant with respect to the untapered wing. The shape of the spanwise lift distribution clarifies this. The gradient of the spanwise lift distribution of the tapered wing is more constant with respect to the gradient of the spanwise lift distribution of the untapered wing. Therefore, for propellers with an inboard-up configuration located near the root of the tapered wing, more lift is present at the wing section behind the inboard side of the propeller, resulting in a larger difference in lift between the wing sections behind the two propeller sides, and therefore a larger net positive swirl recovery. Near the tip of the wing, the gradient of the spanwise lift distribution of the untapered wing is larger compared to that of the tapered wing. Therefore, the net positive swirl recovery of the untapered wing is larger for inboard-up rotating propellers near the tip of the wing. The lift-induced drag of the system slightly reduces for the tapered wing when the propeller is located more towards the tip of the wing than inboard positions of the propeller. This is clarified by the fact that in section I, the lift gradient of the spanwise lift distribution becomes more constant by the influence of the propeller-induced velocities such that the lift-induced drag reduces.

The taper ratio of the wing increases the gradient of the spanwise lift distribution of the wing. This increases the net positive swirl recovery contribution for propeller-wing systems where the propeller has an inboard-up configuration located near the root of the wing. From this comparison, it is concluded that the increase in the net positive swirl recovery contribution to the combined drag of the system is lower when the wing has a taper ratio. For this reason, there could be possible that the propeller is placed closer to the root of the wing to obtain a similar amount of net positive swirl recovery. When combined with a wing planform that results in a low lift-induced drag with the influence of the inboard-mounted propeller, the combined drag could be reduced with the structural benefits of an inboard-mounted propeller.

7.8. Discussion

The numerical model has been used to decompose the induced drag components of the wing to investigate the influence and interaction of lift-induced drag and swirl recovery on the performance of propeller-wing systems. Although the numerical model is validated and was used to show the contribution of the swirl recovery to the induced drag of the propeller wing system, some remarks are made about the results concerning the fact that the numerical model shows discrepancies with the data from wind tunnel experiments.

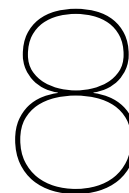
The contribution of swirl recovery to the induced drag of the system is shown. When a propeller-wing system is designed correctly, part of the lost energy in the form of swirl in the propeller slipstream is recovered in the form of thrust. As mentioned in Section 6.3.1, Nederlof has shown the overprediction of lift by the way the tangential velocity is taken into account in the numerical model. With this knowledge, it is admitted that the lift by the change in the local angle of attack effect visualized in Figure 3.2b is overpredicted. This would reduce the net swirl recovery contribution in the presented analyses. The lift-induced drag of the system would also decrease as the gradient of the spanwise lift distribution decreases. As has been shown in the results from the analyses, the contribution of the net swirl recovery is larger for the used propeller OPs. A correction is applied for axial velocity within the propeller slipstream by averaging it over the height of the propeller. This decreases the amount of lift-induced drag of the propeller wing system as the gradient of the spanwise wing lift distribution decreases near and within the propeller slipstream. Furthermore, the Rethorst correction is applied within the numerical model. This correction reduces the local lift within the propeller slipstream by the influence of the axial velocity. This again reduces both lift-induced drag more compared to the swirl recovery by the previous reasoning.

As presented in Section 7.1.1, the thrust by the propellers is estimated only to produce 88% of the thrust needed for the Fokker F-27 during the cruise phase. By implementing higher thrust-producing propellers, the axial and tangential velocities within the propeller slipstream increase, which results in higher lift-induced drag and net positive swirl recovery contributions. The use of the VMF estimates this effect. However, it is not sure whether the usage of this factor results in realistic velocities within the propeller slipstream.

As the numerical model is a SIM, the influence of the wing on the propeller is not taken into account. This influence could lead to a non-symmetric velocity profile within the propeller slipstream, as explained in Section 3.1. A result of a non-symmetric velocity profile within the propeller slipstream could be increased differences in wing lift behind the two propeller sides. This could influence the amount of net swirl recovery and lift-induced drag. Also, the overall performance of the propeller is changed by the influence of the wing, such that the slipstream characteristics are changed, and the induced drag components are changed.

The numerical model does not consider the influence of the nacelle of the propeller. The drag of the propeller-wing system is significantly reduced by leaving out the presence of the nacelle. The influence of the nacelle on the performance of the wing is most pronounced for propellers located fully within the span of the wing, as it influences the wing on both sides. The nacelle creates a local increase in the angle of attack [9, 21]. This increases the local lift at the wing sections next to the nacelle. These differences could increase the net contribution of the lift-induced drag as the gradient of the spanwise lift distribution is changed. The net swirl recovery is possibly not changed as the increase in lift at both sides would be the same for a conventional-mounted propeller. For a tip-mounted propeller, the net positive swirl recovery of the wing can increase as only the lift of the wing behind one propeller side increases. The lift drop at the location of the nacelle, however, is expected to influence the lift-induced drag significantly by the increased gradient of the spanwise wing lift distribution.

Finally, the aerodynamics of the propeller-wing system are highly turbulent and unsteady. As the numerical model is based on the potential flow theory, the full complexity of the flow is simplified. These simplifications lead to discrepancies with reality, but as is shown in the validation of the numerical model, it should be capable of providing a reasonable estimation of the lift and induced drag of the system. Although some aspects of the propeller-wing system are modeled such that discrepancies appear or are not taken into account, the results from the previous sections show a valid conclusion for propeller-wing systems. The contribution of the net swirl recovery to the induced drag of the system is significant and does reduce the total induced drag of the system when properly designed.



Conclusions

In the final chapter of this thesis, the main findings of the previous chapter on the contribution and interaction of the lift-induced drag and swirl recovery to the induced drag of propeller-wing systems are stated in the conclusions in Section 8.1. Hereafter, recommendations for future research based on the results and conclusions from this thesis are provided in Section 8.2.

8.1. Conclusions

This thesis dealt with research on the contribution of swirl recovery to the induced drag of propeller-wing systems. A numerical model was developed to decouple the induced drag components of the wing in a parametric study such that the relative contribution of the lift-induced drag and swirl recovery drag could be investigated. First, the gradient of the spanwise wing lift distribution was found to be an influential parameter on the amount of net swirl recovery that could be obtained by the wing. When the propeller is placed in front of the wing where the gradient of the spanwise lift distribution is high, the amount of net positive swirl recovery to the induced drag could be increased. With this propeller placement, the propeller side where the blades are rotating in the upward direction is placed in front of the wing section where the isolated wing lift is higher compared to the side where the blades are moving down. This situation increases the net positive swirl recovery of the wing. In literature, conclusions are made on the reduction of induced drag for inboard-up configured propellers in propeller-wing systems. These conclusions are valid, when the gradient of the isolated spanwise wing lift distribution is negative from root to tip, but can be incorrect when the propeller is placed in front of a section where the gradient of the isolated spanwise wing lift distribution is positive from root to tip. The induced drag of the system is influenced by the gradient of the spanwise wing lift distribution and the difference in the lift at the wing sections behind the two propeller sides, resulting in the lift-induced drag and net swirl recovery thrust, respectively.

Furthermore, it is found that the disk loading, or the amount of thrust produced by the propeller, influences the amount of net swirl recovery of the wing in the propeller-wing system. With a higher disk loading, the propeller-induced velocities increase. Subsequently, this increases the difference in the lift of the wing sections behind the two sides of the propeller, such that the net swirl recovery is changed. The difference in the lift should, however, not increase too much as this increases the gradient of the spanwise wing lift distribution such that the lift-induced drag starts to dominate the amount of induced drag.

The rotational direction of the propeller influences the difference in the amount of lift at the wing sections behind the propeller sides. It is shown that when the rotational direction of the propeller is such that it further increases the difference in the lift at the wing sections behind the two propeller sides, the amount of lift-induced drag and the amount of net swirl recovery of the wing increases. The beneficial effect of the increase in the difference in the lift of the wing sections behind the two propeller sides is found to be larger compared to the detrimental effects of rotating the propeller into the other direction as the amount of net the swirl recovery is determined on the difference in the lift of the wing behind the

two propeller sides. The amount of net swirl recovery that the wing can obtain is not influenced by the rotational direction of the propeller when the gradient of the isolated wing lift distribution is zero behind the center of the propeller. In this specific case, the lift of the sections behind the two propeller sides is equal to each other.

The aspect ratio of the wing influences not only the lift-induced drag of the wing but also the amount of net swirl recovery of the wing. In the presented analysis, the net positive swirl recovery dominates over the lift-induced drag of the system. Changing the disk loading of the propeller changes the propeller-induced velocities within the propeller slipstream. This changes the amount of lift of the wing sections behind the propeller such that the amount of net positive swirl recovery is changed, and changes the gradient of the spanwise wing lift distribution such that the lift-induced drag is changed.

In aircraft design, the contribution of the net positive swirl recovery can lead to an increased performance of the propeller-wing system by the reduction of the induced drag of the wing. The difference in the lift of the wing sections behind the two sides of the propeller should be increased to increase the net positive swirl recovery of the wing. In contrast, the gradient of the spanwise wing lift distribution should remain low such that the lift-induced drag of the wing is low. During the design of aircraft with propeller-wing systems, the optimum lift distribution should be achieved by maximizing the amount of net positive swirl recovery by the difference in lift between the two propeller sides, and minimizing the lift-induced drag which is influenced by the gradient of the spanwise wing lift distribution such that a minimum induced drag of the wing results. The design of aircraft, especially aircraft with propeller-wing systems, remains a multidisciplinary design problem. With the conclusions from this thesis, better insight is obtained into the aerodynamic relative contribution of the components of the induced drag of the wing: the lift-induced drag and swirl recovery drag. With this report, design choices can be substantiated such that better performances can be obtained in future propeller-wing system designs.

8.2. Recommendations

It is recognized during the thesis that several recommendations should be considered when future research is conducted on the performance of propeller-wing systems. First, two points are addressed regarding the numerical model:

- The current modeling method of the swirl is simplistic compared to the corrections used for the axial propeller-induced velocities. It is seen that the tangential velocities have a significant impact on the spanwise lift distribution, changing the amount of lift-induced drag and swirl recovery. From past studies, it has been determined that modeling the swirl by the change in the angle of attack overpredicts the local lift of the wing. Therefore, it is recommended that a similar correction method is developed for the influence of the tangential velocities on the lift distribution of the wing as for the axial propeller-induced velocities.
- The determination of the lift-induced drag of the propeller-wing system is complicated due to the axial jet velocity over the wing. A recommendation is made to investigate the modeling of the lift-induced drag of the wing with the influence of a jet. The author recognizes the possibility which could lie in the implementation of the Prabhu correction for the corrected downwash of the propeller-wing system as is presented in Appendix B.

Two more recommendations are made on the research to investigate the contribution of the drag components to the total drag of propeller-wing systems:

- In this thesis, the cruise phase of the aircraft is considered. The lift-induced drag of the propeller is higher during the take-off and landing phases of the aircraft when the angle of attack is large. During the take-off phase, the propeller-induced velocities are higher due to the higher disk loading of the propeller. Therefore, it is recommended to investigate further the contribution of the swirl recovery to the induced drag at these phases of the flight. It is recommended to use a numerical model which can provide representative performance characteristics of the propeller-wing system at higher angles of attack.

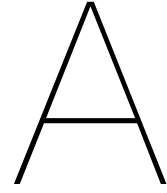
- During the landing phase of the aircraft, the propeller could be used in an energy harvesting mode, changing the velocities in the propeller slipstream. When further research is conducted on this propeller mode, it is also recommended to investigate the influence on the induced drag components of the wing.
- More research is recommended into the height of the propeller with respect to the wing. Studies have shown the benefits of the over-the-wing configuration of propellers. This propeller position, however, reduces the net positive swirl recovery by the wing as the tangential velocities are lower behind lower horizontal sections of the propeller. In this case, using the modified slipstream tube model from Willemsen [19] is recommended, where the tube contracts in the axial direction.

References

- [1] T. C. A. Stokkermans. “Design and Analysis of Swirl Recovery Vanes for an Isolated and a Wing Mounted Tractor Propeller”. MSc. Delft University of Technology, Aug. 2015.
- [2] M. D. Moore and B. Fredericks. “Misconceptions of Electric Aircraft and their Emerging Aviation Markets”. In: *52nd Aerospace Sciences Meeting*. Jan. 2014. DOI: 10.2514/6.2014-0535.
- [3] K. A. Deere et al. “Computational analysis of a wing designed for the X57 distributed electric propulsion aircraft”. In: *AIAA Aviation Forum 2017* (June 2017). DOI: 10.2514/6.2017-3923.
- [4] *ASAB Projects*. Accessed: 9-11-2021. URL: <https://sacd.larc.nasa.gov/x57maxwell/>.
- [5] D. P. Witkowski, A. K. H. Lee, and J. P. Sullivan. “Aerodynamic interaction between propellers and wings”. In: *Journal of Aircraft* 26.9 (Sept. 1989).
- [6] I. Kroo. “Propeller-wing integration for minimum induced loss”. In: *Journal of Aircraft* 23.7 (1986), pp. 561–565. DOI: 10.2514/3.45344.
- [7] M. H. Snyder Jr. and G. W. Zumwalt. “Effects of wingtip-mounted propellers on wing lift and induced drag”. In: *Journal of Aircraft* 6.5 (May 1969), pp. 392–397. DOI: 10.2514/3.44076.
- [8] A. C. Kermode. *Mechanics of Flight*. 11th. New York: Pearson (Education), 2006. ISBN: 978–1–4058–2359–3.
- [9] L. L. M. Veldhuis. “Propeller Wing Aerodynamic Interference”. PhD thesis. Delft University of Technology, June 2005.
- [10] R. Nederlof. “Improved modeling of propeller-wing interactions with a lifting-line approach”. MSc. Delft University of Technology, May 2020.
- [11] J. Katz and A. Plotkin. *Low-Speed Aerodynamics*. 2nd ed. Cambridge Aerospace Series. Cambridge University Press, 2001. DOI: 10.1017/CBO9780511810329.
- [12] J. D. Anderson. *Fundamentals of Aerodynamics*. 5th. New York: McGraw-Hill, 2011. ISBN: 978-0-07-339810-5.
- [13] I. Kroo. *Nonplanar Wing Concepts for Increased Aircraft Efficiency*. VKI lecture series on Innovative Configurations and Advanced Concepts for Future Civil Aircraft. June 2005.
- [14] J. D. Anderson. *Aircraft Performance & Design*. McGraw-Hill international editions. McGraw-Hill Education, 1999. ISBN: 9780070019713.
- [15] Jr. H. H. Hurt. *Aerodynamics for Naval Aviators*. Office of the Chief of Naval Operations, Aviation Training Division, Jan. 1965.
- [16] M. Voskuil, J. van Bogaert, and A. G. Rao. “Analysis and design of hybrid electric regional turboprop aircraft”. In: *CEAS Aeronautical Journal* 9 25.15 (Mar. 2018). DOI: 10.1007/s13272-017-0272-1.
- [17] L. J. Heidelberg and R. P. Woodward. “Advanced Turboprop Wing Installation Effects Measured by Unsteady Blade Pressure and Noise”. In: *11th Aeroacoustics Conference* (Oct. 1987). DOI: 10.2514/6.1987-2719.
- [18] N. Van Arnhem et al. “Aerodynamic interaction effects of tip-mounted propellers installed on the horizontal tailplane”. In: *AIAA Aerospace Sciences Meeting (210059 ed.)*. [AIAA 2018-2052] American Institute of Aeronautics and Astronautics Inc. (2018). DOI: 10.2514/6.2018-2052.
- [19] R. Willemsen. “A sensitivity study on the aerodynamic performance of a wingtip-mounted tractor propeller-wing system”. MSc. Delft University of Technology, Nov. 2020.
- [20] L. L. M. Veldhuis. “Review of Propeller-Wing Aerodynamic Interference”. In: *24th International Congress of the Aeronautical Sciences* (2004).

- [21] T. Sinnige et al. "Wingtip-Mounted Propellers: Aerodynamic Analysis of Interaction Effects and Comparison with Conventional Layout". In: *Journal of Aircraft* 56.1 (Nov. 2018), pp. 295–312. DOI: 10.2514/1.C034978.
- [22] L. R. Miranda and J. E. Brennan. "Aerodynamic effects of wingtip-mounted propellers and turbines". In: *AIAA* (June 1986). DOI: 10.2514/6.1986-1802.
- [23] J. A. Cole et al. "Influence of Propeller Location, Diameter, and Rotation Direction on Aerodynamic Efficiency". In: *Journal of Aircraft* 58.1 (Feb. 2021), pp. 63–71. DOI: 10.2514/1.C035917.
- [24] E. A. Ebbens. "Aerodynamic modelling of open rotor-wing-flap interactions with low-fidelity methods". MSc. Delft University of Technology, Sept. 2022.
- [25] J. D. Anderson. *Introduction to Flight*. 7th. New York: McGraw-Hill, 2012. ISBN: 978-007-108605-9.
- [26] E. Branlard. *Wind Turbine Aerodynamics and Vorticity-Based Methods*. Vol. 7. Jan. 2017. ISBN: 978-3-319-55163-0. DOI: 10.1007/978-3-319-55164-7.
- [27] J. A. Cole. "A Higher-Order Free-Wake Method for Aerodynamic Performance Prediction of Propeller-Wing Systems". PhD thesis. Pennsylvania State University, Dec. 2016.
- [28] G. Bramesfeld and M. D. Maughmer. "Relaxed-Wake Vortex-Lattice Method Using Distributed Vorticity Elements". In: *Journal of Aircraft* 45.2 (Apr. 2008), pp. 560–568. DOI: 10.2514/1.31665.
- [29] J. A. Cole et al. "Higher-Order Free-Wake Method for Propeller–Wing Systems". In: *Journal of Aircraft* 56.1 (Feb. 2019), pp. 150–165. DOI: 10.2514/1.C034720.
- [30] M. Drela. "QPROP formulation". In: (June 2006).
- [31] M. Drela and H. Youngren. "XROTOR User Guide". In: (Nov. 2003).
- [32] R. K. Prabhu. "Studies on the Interference of Wings and Propeller Slipstreams". PhD thesis. Old Dominion University, Aug. 1984. DOI: 10.25777/ezag-d204.
- [33] W. F. Phillips and D. O. Snyder. "Modern Adaptation of Prandtl's Classic Lifting-Line Theory". In: *Journal of Aircraft* 37.4 (2000), pp. 662–670. DOI: 10.2514/2.2649.
- [34] S. Rethorst. "Aerodynamic of Nonuniform Flows as Related to an Airfoil Extending Through a Circular Jet". In: *Journal of the Aerospace Sciences* 25.1 (1958), pp. 11–28. DOI: 10.2514/8.7479.
- [35] T. Sinnige et al. "Aerodynamic Performance of a Wingtip-Mounted Tractor Propeller Configuration in Windmilling and Energy-Harvesting Conditions". In: *AIAA Aviation 2019 Forum*. DOI: 10.2514/6.2019-3033.
- [36] J. Sørensen, K. Dag, and N. Ramos-García. "A New Tip Correction Based on the Decambering Approach". In: *Journal of Physics: Conference Series* 524 (June 2014), p. 012097. DOI: 10.1088/1742-6596/524/1/012097.
- [37] E. Benini. "Significance of blade element theory in performance prediction of marine propellers". In: *Ocean Engineering* 31.8 (2004), pp. 957–974. ISSN: 0029-8018. DOI: <https://doi.org/10.1016/j.oceaneng.2003.12.001>.
- [38] B. W. McCormick. *Aerodynamics, Aeronautics, and Flight Mechanics*. John Wiley & Sons, 1994. ISBN: 9780471575061.
- [39] J. G. Leishman. *Principles of helicopter aerodynamics*. 2nd ed. Cambridge University Press, 2006. ISBN: 978-0-521-85860-1.
- [40] K. Biber. "Estimating Propeller Slipstream Drag on Airplane Performance". In: *Journal of Aircraft* 48.6 (2011), pp. 2172–2174. DOI: 10.2514/1.C031458.
- [41] M. Minervino et al. "Drag Reduction by Wingtip-Mounted Propellers in Distributed Propulsion Configurations". In: *Fluids* 7.7 (2022). ISSN: 2311-5521. DOI: 10.3390/fluids7070212. URL: <https://www.mdpi.com/2311-5521/7/7/212>.

- [42] M. Yahyaoui. "Generalized Vortex Lattice Method for Predicting Characteristics of Wings with Flap and Aileron Deflection". In: *International Journal of Aerospace and Mechanical Engineering* 8.10 (2014), pp. 1690–1698. ISSN: 1307-6892. URL: <https://publications.waset.org/vol/94>.
- [43] P. Aref et al. "Computational Study of Propeller–Wing Aerodynamic Interaction". In: *Aerospace* 5.3 (2018). ISSN: 2226-4310. DOI: 10.3390/aerospace5030079. URL: <https://www.mdpi.com/2226-4310/5/3/79>.
- [44] E. A. Marcus et al. "Aerodynamic Investigation of an Over-the-Wing Propeller for Distributed Propulsion". In: *2018 AIAA Aerospace Sciences Meeting*. DOI: 10.2514/6.2018-2053. URL: <https://arc.aiaa.org/doi/abs/10.2514/6.2018-2053>.
- [45] L. Qingxi, W. Yangang, and G. Eitelberg. "An investigation of tip vortices unsteady interaction for Fokker 29 propeller with swirl recovery vane". In: *Chinese Journal of Aeronautics* 29.1 (2016), pp. 117–128. ISSN: 1000-9361. DOI: <https://doi.org/10.1016/j.cja.2015.12.004>.
- [46] W. Green. *The Observers Book of Aircraft*. Frederick Warne & Co. Ltd, 1970. ISBN: 0-7232-0087-4.
- [47] S. Gudmundsson. *General Aviation Aircraft Design: Applied Methods and Procedures*. Elsevier Science, 2013. ISBN: 9780123973290.
- [48] L. L. M. Veldhuis and P. M. Heyma. "Aerodynamic optimisation of wings in multi-engined tractor propeller arrangements". In: *Aircraft Design* 3.3 (2000), pp. 129–149. DOI: 10.1016/S1369-8869(00)00010-0.
- [49] S. C. Smith. *A Computational and Experimental Study of Nonlinear Aspects of Induced Drag*. Ames Research Center, Feb. 1996.
- [50] C. Ferarri. "Propellers and Wing Interaction at Subsonic Speeds". In: *Aerodynamics Component of Aircraft at High Speed*. Ed. by A. F. Donovan and H. C. Lawrence. Princeton, New Jersey: Princeton University Press, 1957. Chap. 3.



Lifting-Line Theory & Vortex Lattice Method Comparison

The vortex lattice method (VLM) follows from the lifting-line (LL) theory. Both methods can be used for a first estimate of the performance of a wing. During the analysis of the lift-induced drag of propeller-wing systems, various methods to obtain the downwash of a wing were explored. One of them, which is used in the analysis of this thesis, is extensively elaborated on in Section 5.2.3. It was investigated whether a sectional approach of the LLT would also work to obtain the lift-induced drag of the propeller-wing system. This, however, was not the case as the lift-induced drag obtained by the two methods differs from each other. The lift-induced drag distributions obtained by the LLT and VLM are elaborated on in Section A.1. The lift for a straight isolated wing comes out to be exactly the same for both methods, which is not further elaborated on in this appendix. In Section A.2, the outcome of the VLM, which is used for the analysis throughout the thesis, is compared to the lift-induced drag obtained with a Trefftz plane analysis.

A.1. Induced Drag by LLT & VLM

For the comparison between the LL theory and the VLM, an isolated wing with elliptic circulation distribution is used. Equation A.1 shows the elliptic circulation distribution, where Γ_0 is the center circulation of the wing.

$$\Gamma(y) = \Gamma_0 \sqrt{1 - \left(\frac{2y}{b}\right)^2} \quad (\text{A.1})$$

The lift-induced drag of the wing can be obtained in twofold. For the LL theory, the lift-induced drag is obtained by a sectional approach. Using this theory, the downwash at each wing section follows from the lift at that section. For a symmetric airfoil obeying the thin-airfoil theory, the induced angle of attack can be calculated with Equation A.2. Hereafter, the lift-induced drag is calculated by Equation A.3. For the VLM, the lift-induced drag results from the usage of an influence matrix of the trailing vortices on the bound vortices of the panels, as is described in detail in Section 5.2.1.

$$\alpha_i(y) = \alpha_g(y) - \frac{c_l(y)}{2\pi} \quad (\text{A.2})$$

$$c_{d_i}(y) = \tan(\alpha_i(y)) c_l(y) \quad (\text{A.3})$$

The lift-induced drag distributions obtained with the LL theory and VLM are presented in Figure A.1. This comparison is made for two different aspect ratios. The lift-induced drag over the span of the wing remains the same for LL theory, whereas the lift-induced drag obtained with the VLM becomes smaller over the span as expected from Section 2.2.1. For this reason, using a simple sectional approach is not recommended to obtain the spanwise downwash distribution of a propeller-wing system.

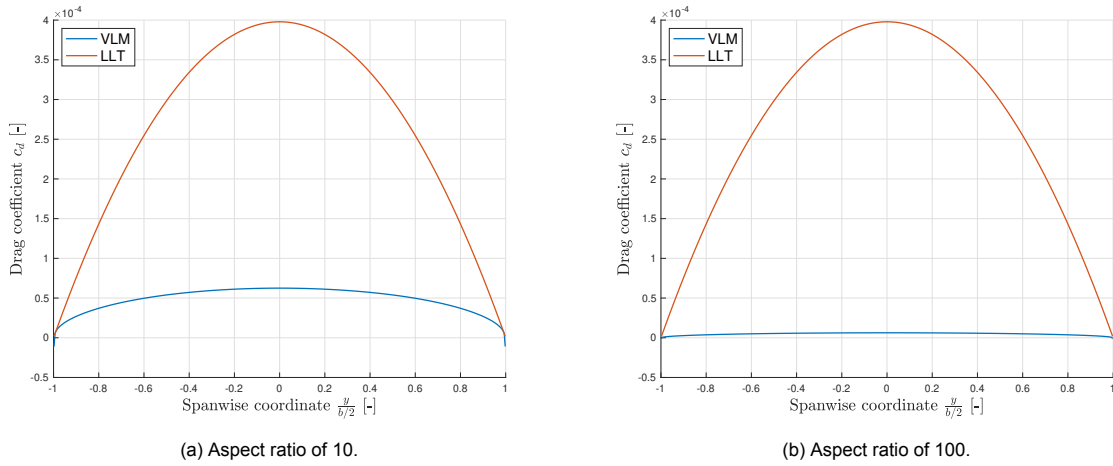


Figure A.1: Lift-induced drag obtained with the LL theory and VLM.

A.2. Trefftz Plane Analysis

The Trefftz plane analysis is used to obtain the drag by considering the momentum balance around an object [48]. Whole propeller-wing systems can be analyzed by this analysis method as the thrust of the propeller is also considered in the balance. The control surface behind the wing, the Trefftz plane, passes through the wake of the wing, as is visualized in Figure A.2. The drag by a Trefftz plane analysis for an isolated wing can be calculated by Equation A.4, where Γ_i is the strength of the bound vortex of panel i , γ_j is the strength of each of the trailing vortices, and y_{b_i} and y_{c_i} are the spanwise locations of the trailing vortices and control points, respectively. Figure A.3 shows the simplified Trefftz plane for an isolated wing [49].

$$D_i = \frac{\rho}{4\pi} \sum_{i=1}^n \sum_{j=1}^{n+1} \Gamma_i \gamma_j \frac{(y_{b_i} - y_{c_i})(y_{b_{i+1}} - y_{b_i})}{(y_{b_j} - y_{c_i})^2} \tag{A.4}$$

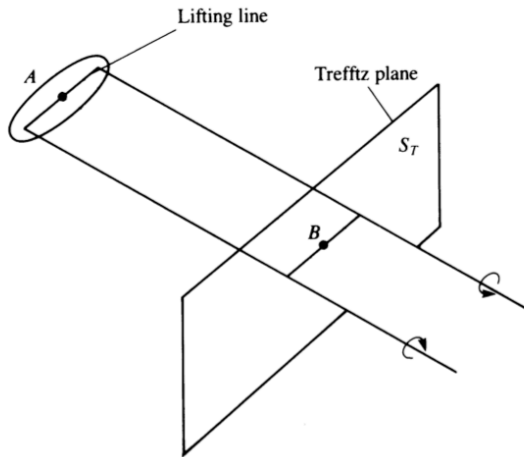


Figure A.2: Trefftz plane for the lift-induced drag calculation [11].

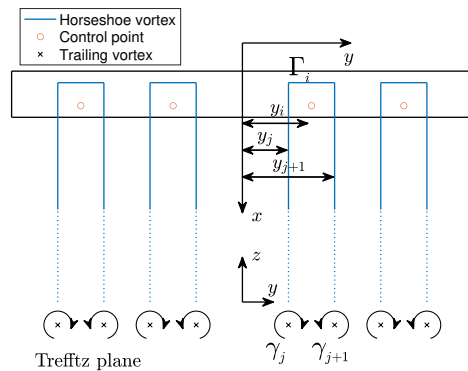


Figure A.3: Schematic of the Trefftz plane analysis for an isolated wing.

Finally, it can be verified with Figure A.4 that the VLM and Trefftz plane analysis obtains the same induced drag distribution. This strengthens the final statement of the previous section, as the sectional approach has less precision than that of the VLM in predicting the lift-induced drag of the wing.

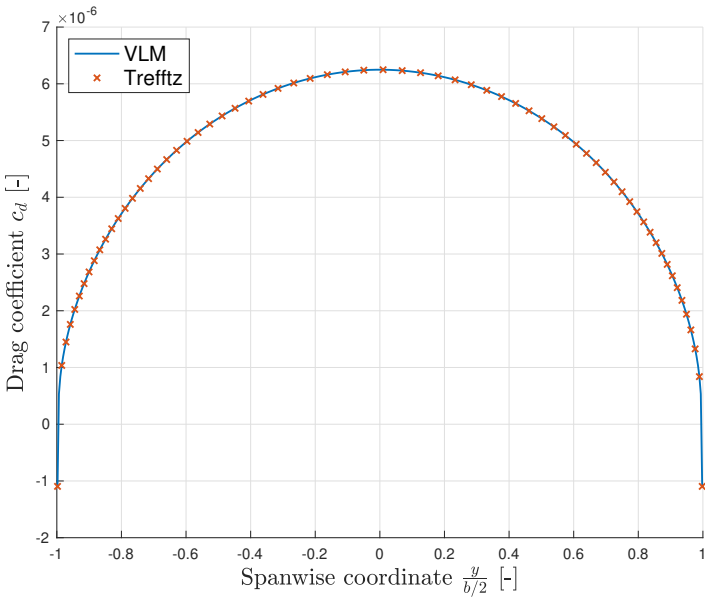


Figure A.4: Lift-induced drag obtained with the VLM and Trefftz plane analysis for a wing with aspect ratio of 10.

B

Prabhu Correction for Downwash of Propeller-Wing Systems

An alternative approach to obtain the downwash distribution of a propeller-wing system was proposed by Ferrari [50] and further elaborated on by Prabhu [32]. The method relies on the assumption that there is a continuous pressure and density over the fluid boundary between the propeller slipstream and freestream. For the derivation of the entire method, the reader is referred to the paper by Ferrari [50]. Within this appendix, the method is applied for the same jet presented in Section 5.2.3 with $R/b/2 = 0.143$ and $\mu = 0.667$.

In Figure B.1, a schematic discontinuous circulation distribution with trailing vortices from a center-located jet is seen. Again, a lower circulation distribution is seen within part 2, where the high jet velocity is present, compared to parts 1 and 3. The latter two only experience the freestream velocity as they lay outside the jet. The downwash from the three parts is considered separately, such that all the circulation, $(\gamma_0)_I$, from part 1 is fully shed into the wake at the trailing vortex located at the boundary between parts 1 and 2. All the circulation from part 2, $-(\gamma_0)_{II}$, is brought to the bound vortex at the same spanwise location. These trailing vortices from parts 1 and 2 are considered fully out and inside the propeller slipstream, respectively. The same separation of trailing vortices is also applied at the other boundary. The vortex shedding is visualized in Figure B.2. Besides the high vortex shedding at the propeller boundary, an increased shedding is seen near the wing tips.

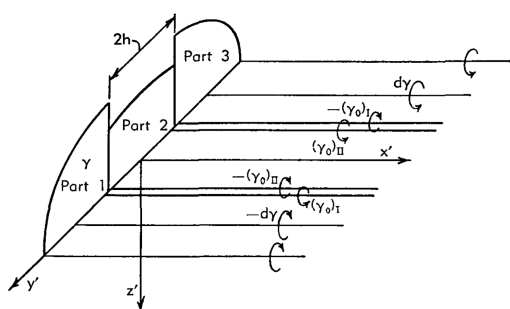


Figure B.1: Circulation distribution divided into parts for the Prabhu downwash correction [50].

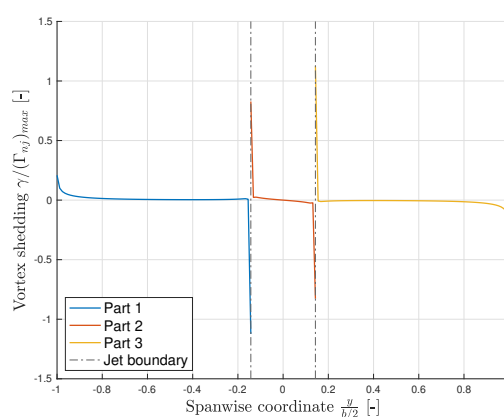


Figure B.2: Vortex shedding into the wake by parts.

With each part of the wing having its own system of trailing vortices, Equations B.1a and B.1b are used to obtain the downwash at spanwise locations, y , inside and outside the slipstream from the trailing

vortices located at η , respectively. The method relies on the velocity ratio $\mu_p = U_j/U_\infty$, from which are used in the variables $\varepsilon_1 = (\mu_p^2 - 1)/(\mu_p^2 + 1)$ and $\varepsilon_2 = (\mu_p - 1)^2/(\mu_p^2 + 1)$. It should be noted, and carefully taken into account that the velocity ratio, μ_p , is the inverse of the velocity ratio, μ , used for the Rethorst correction from Section 5.2.2. In the case of zero jet velocity, the variables ε_1 and ε_2 would go to zero, such that only the first integrals remain in Equation B.1, which is essentially the same as for a Trefftz plane analysis [32] as presented in Appendix A.

$$w_i(y) = \frac{1}{4\pi} \left\{ \int_{-b/2}^{b/2} \frac{d\Gamma(\eta)}{y - \eta} - \varepsilon_2 \left(\int_{-b/2}^R + \int_R^{b/2} \right) \frac{d\Gamma(\eta)}{y - \eta} + \varepsilon_1 \int_{-R}^R \frac{d\Gamma(\eta)}{y - R^2/\eta} \right\} \quad \text{for } |y| < R \quad (\text{B.1a})$$

$$w_i(y) = \frac{1}{4\pi} \left\{ \int_{-b/2}^{b/2} \frac{d\Gamma(\eta)}{y - \eta} - \varepsilon_2 \int_{-R}^R \frac{d\Gamma(\eta)}{y - \eta} - \varepsilon_1 \left(\int_{-b/2}^{-R} + \int_R^{b/2} \right) \frac{d\Gamma(\eta)}{y - R^2/\eta} \right\} \quad \text{for } |y| > R \quad (\text{B.1b})$$

From these equations and the spanwise vortex shedding from Figure B.2, a new spanwise downwash distribution is obtained, which is visualized in Figure B.3. Comparing this with the downwash from a wing without jet velocity, it is seen that the trailing vortices at the propeller slipstream boundary induce an upwash just outside the propeller slipstream and only slightly increase the downwash within the slipstream. This method was validated with experimental results for propellers located fully within the span of the wing by Prabhu [32]. The spanwise induced drag distribution is also compared to the method implemented in the thesis, as is presented in Figure B.4. Outside the jet, the Prabhu method gives similar results for the induced drag. However, within the jet, the induced drag is significantly lower than the implemented method within this thesis.

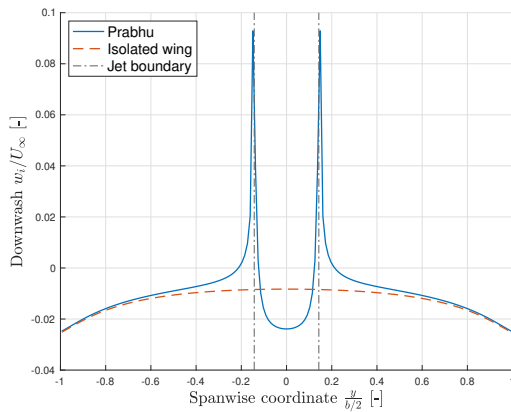


Figure B.3: Downwash distribution obtained by the Prabhu method.

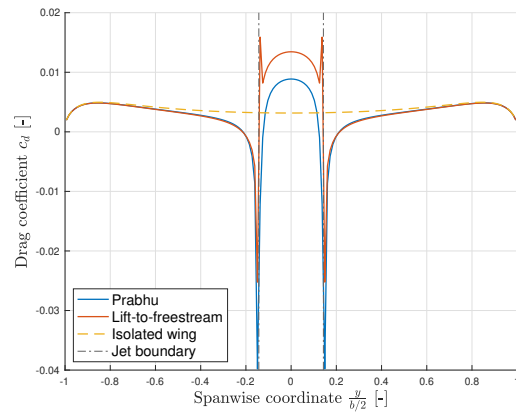


Figure B.4: Lift-induced drag distribution with a center located jet with $\mu = 0.667$.

Now, the position of the jet is changed from the center of the wing to the wingtip. The corresponding circulation distribution and vorticity shedding of this situation is seen in Figure B.5. Only one jump is seen in the circulation distribution, as the other slipstream boundary lies outside of the span of the wing. Furthermore, the vortex shedding distribution shows that the part near the wingtip, where the vortex shedding is higher than the center of the wing, lies within the jet. Due to these two differences with respect to the center-located jet, the method described by Ferrari and Prabhu does not give reasonable results anymore as the same downwash structure is obtained as was visualized in Figure B.6.

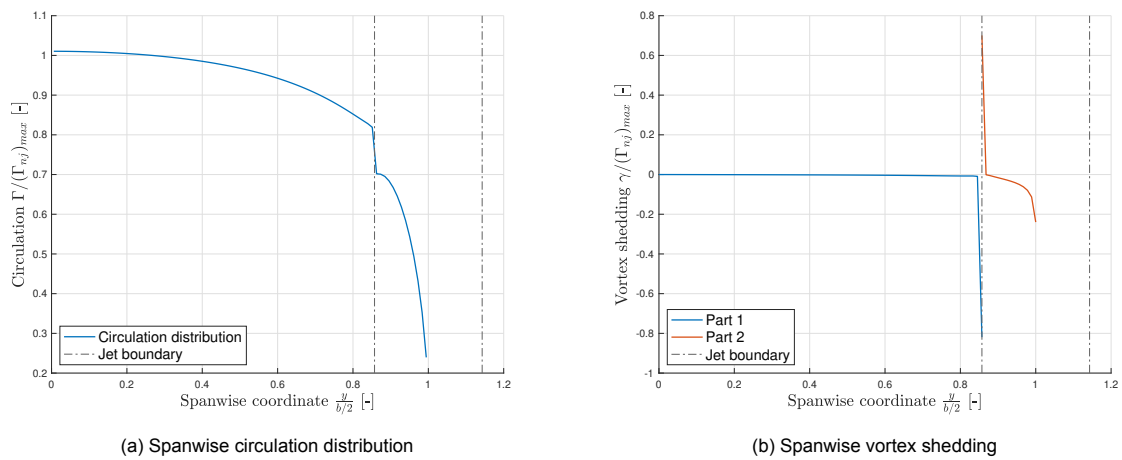
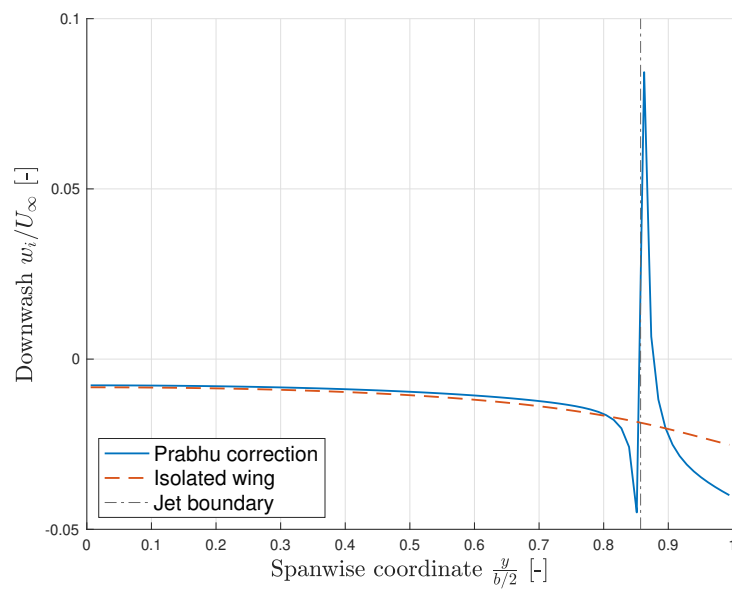
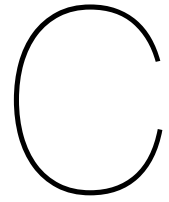


Figure B.5: Jet velocity located at the wingtip.

Figure B.6: Incorrect downwash distribution obtained with the Prabhu correction for a tip-located jet with $\mu = 0.667$.



Swirl Averaging

A similar approach was taken in averaging the swirl or the tangential velocities over the height of the propeller slipstream. A similar division of elements over the propeller cross-section is used, as seen in Figure 5.5. The velocity is multiplied by the area of the element. Subsequently, it is divided by the area of the strip, such that the averaged swirl velocity over the strip is obtained. The mathematical representation of the averaging of the tangential velocities is given in Equation C.1.

$$\overline{u_{z_i}} = \frac{\sum_1^j u_{z_{i,j}} \Delta y}{j \Delta z} \quad (\text{C.1})$$

First, the approach is tested by a simple representation of the swirl of a propeller. As was done by Nederlof [10], a sine wave with an amplitude of 5 m/s is used to represent the tangential velocities of the propeller. The direct swirl from the sine wave and averaged swirl are presented in Figure C.1. The averaged tangential velocity is lower than the actual swirl. The amplitude of the averaged swirl wave only reaches 3 m/s and is shifted slightly towards the center of the propeller.

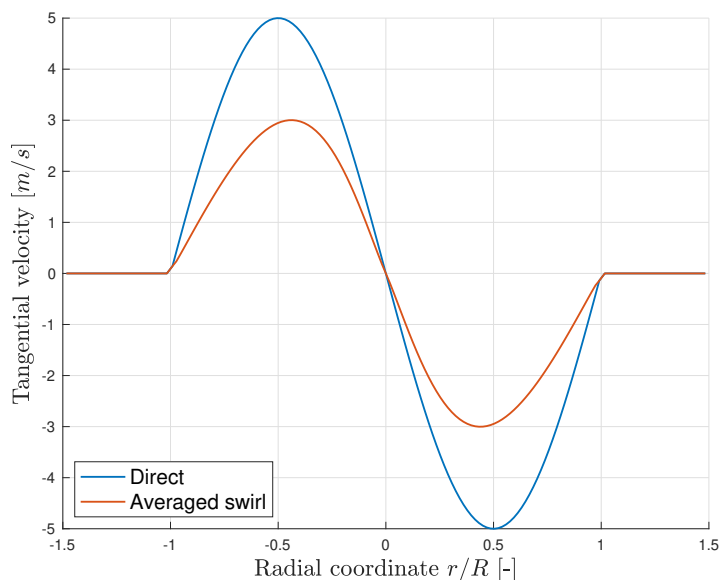


Figure C.1: Swirl averaging applied to a sine wave with an amplitude of 5 m/s.

The swirl averaging method is also applied to a propeller-wing system as is used during the analysis in Chapter 7. OP 1 is used within this comparison as this resulted in the highest swirl induced by the propeller. Figure C.2 shows the performance of the wing with and without the swirl averaging method

applied. In Figure C.2a, the lift distributions of the same propeller-wing systems are visualized. The lift distribution showing the highest lift in section II has no swirl averaging. As a system lift coefficient of 0.35 is desired for both systems, more lift has to be produced within section I for the system where swirl averaging is applied. The drag distributions of the previously described systems are visualized in Figure C.2b. From a visual inspection, it is seen that the lift-induced drag and swirl recovery are reduced by the averaging of the tangential velocities. As the swirl recovery is reduced by a larger amount, the total drag reduction with section II has reduced. Within section I, the lift-induced drag of both systems remain very similar to each other. This reasoning is also applied to the system coefficients, which are compared in Table C.1. The lift-induced drag has slightly decreased, whereas the net positive swirl recovery reduced by a factor of 0.71. Finally, it is seen that the combined drag of the system with the swirl averaged over the height of the propeller is 1.14 times larger compared to the system where the swirl is directly taken at the control points of the wing.

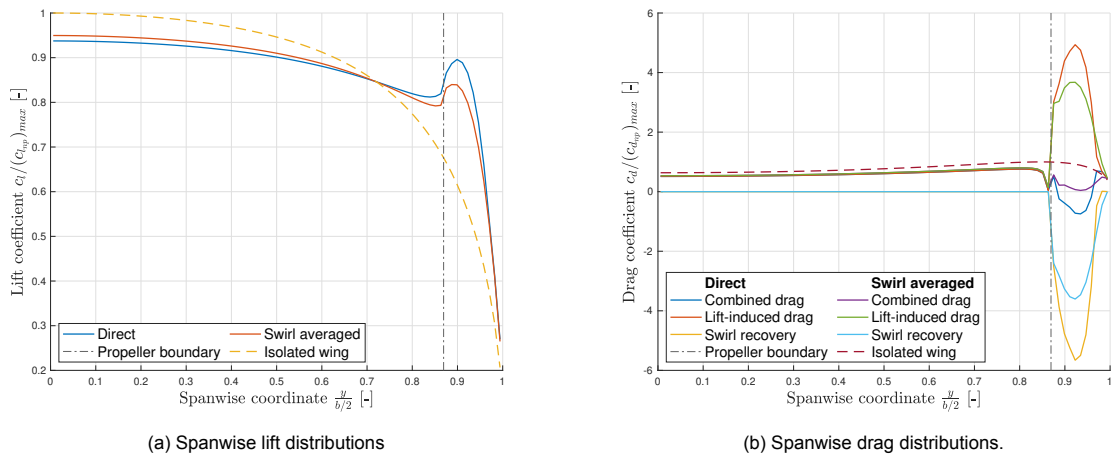
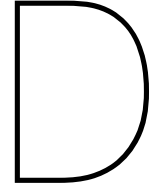


Figure C.2: Spanwise performance by the influence of the swirl averaging method.

Table C.1: System coefficients of the system with averaged swirl velocities with respect to the direct configuration.

	Swirl averaged
$c_L / (c_L)_{dir}$	1.0
$c_{D_i} / (c_{D_i})_{dir}$	0.96
$c_{D_{sr}} / (c_{D_{sr}})_{dir}$	0.71
$c_D / (c_D)_{dir}$	1.14

The presented results are for a propeller at OP 1, such that the swirl of the propeller is large. This also results in larger differences in drag for both approaches of implementing the swirl into the system. Taking propeller OPs, where the disk loading is lower, would result in smaller differences between the approaches.



Prabhu-Rethorst Correction

As explained in Section 5.2.2, the correction of the finite size of the jet is based on a uniform axial velocity. During the analyses, a non-uniform axial velocity distribution is used, but a correction is applied, assuming that the jet is uniform with a velocity of the average of the non-uniform distribution. Prabhu [32] presented a method to include the distribution of the axial velocity into the Rethorst correction. Willemsen [19] has presented this method for the distribution of one side of the propeller. In this section, the method is adapted such that the method is corrected for the two sides of the axial distributions of the propeller.

The axial velocity distribution is discretized into multiple uniform axial velocities. This is schematically visualized in Figure D.1. Multiple corrections are applied for each axial velocity step with the corresponding radius, r_i . The correction method works from the outer step to the center of the propeller slipstream. The corresponding velocity ratio for each correction, μ_i , used for each velocity step is obtained by Equation D.1. The final correction matrix for the Prabhu-Rethorst method is obtained by summing the correction matrices.

$$\mu_i = \frac{U_\infty + u_{i-1}}{U_\infty + u_i} \quad (\text{D.1})$$

This correction is applied for two different axial velocity profiles, both visualized in Figure D.2. The first profile has an increase in the axial velocity towards the center of the slipstream and follows from $u_x = 3 \cos(\pi r/2/R)$. In this case, the value of μ remains smaller than one, as assumed in the Rethorst correction. The second profile does not comply with this assumption but better represents a non-uniform axial velocity profile within the propeller slipstream.

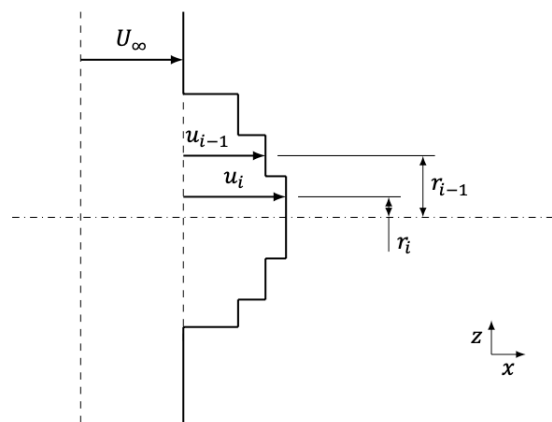


Figure D.1: Discretization method of a non-uniform axial velocity profile for the Prabhu-Rethorst correction [19].

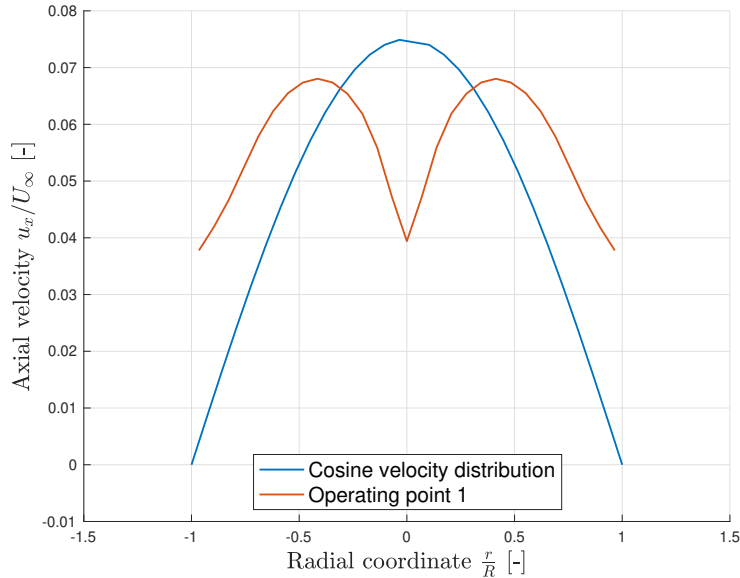


Figure D.2: Axial velocity distributions for the Prabhu-Rethorst correction.

D.1. Cosine Velocity Distribution

The lift distribution obtained by the Prabhu-Rethorst correction method for an axial cosine velocity distribution is visualized in Figure D.3. The wing with aspect ratio of 9.33 is at an angle of attack of 4 degrees with a freestream velocity of 40 m/s.

The single Rethorst correction is the method used during the analyses within the thesis. The Prabhu-Rethorst method is implemented as described previously in this appendix. It is seen that this method provides a smooth lift distribution, where the gradient is less compared to the single Rethorst correction. In this case, the velocity ratio, μ , remains smaller than one for each correction step. From these results, it is reasoned that the lift-induced drag of the wing reduces as the gradient of the spanwise lift distribution has reduced. As the lift distribution is symmetric over the center of the propeller slipstream, the net swirl recovery would not be affected by this method when tangential velocities would be present within the slipstream.

D.2. Operating Point 1

In Figure D.4, the same comparison is shown between the correction methods for the axial velocities of the actual propeller. In this case, however, the axial velocity behind the center of the propeller is lower with respect to the radial positions towards the tip of the propeller. This represents a more realistic axial velocity distribution of a propeller. The figure shows that, as is the case for the single Rethorst correction, the Prabhu-Rethorst method also shows discontinuities near the boundaries of the propeller slipstream. Unfortunately, it is very complex to validate the change in wing lift distribution by only the influence of the axial velocity increase from the propeller, but from these results, it could be interesting for future studies to implement this Prabhu-Rethorst method for the influence of the axial velocity of the propeller slipstream. Especially in optimization studies, the method could be of importance as it is expected that it lowers the amount of lift-induced drag by the reduction of the gradient of the spanwise lift distribution.

It is important to note that, using the correction from the outer radial positions towards the center of the propeller, the velocity ratio, μ , becomes larger than one as the velocity decreases towards the center of the propeller. In this case, the method does not comply with the assumptions made by Rethorst [34]. The effect of using a velocity ratio larger than one should be further investigated when this method is used.

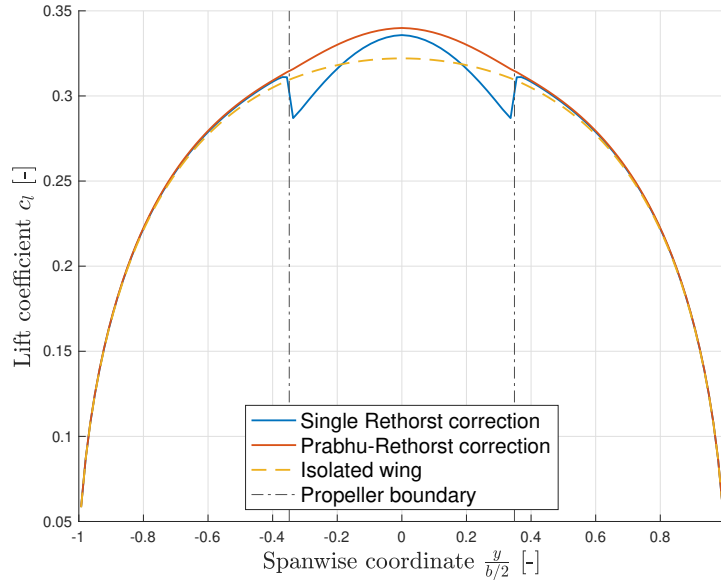


Figure D.3: Corrections for the cosine axial velocity distribution.

D.3. Computational Time

The Rethorst correction is computationally the most expensive module of the numerical model. The Bessel functions are the most expensive part of the correction. The examples of this appendix have 121 panels, of which 29 are within the propeller boundary. One Rethorst correction for a center-mounted propeller takes approximately 35 seconds on a 2.7 GHz Dual-Core Intel Core i5 processor with 8.0 GB installed RAM. The Prabhu-Rethorst correction should be evaluated 15 times for this propeller slipstream, increasing the computational time significantly. When the propeller is placed at the wingtip, it should be noted that a virtual wing is added to the correction method. For this wing, the time of the evaluation time of a single correction increases by more than four times for this example.

With the consideration between computational expense and accuracy, the decision is made not to include the Prabhu-Rethorst method as many propeller-wing system configurations are evaluated, including many with non-center located propellers such that virtual wings increase the computational expense significantly. With a single correction, enough accuracy is obtained to explore the findings in this thesis, such as the importance of the gradient of the isolated wing lift distribution. The small peaks at the boundary of the propeller slipstream do not influence the analyses of the propeller-wing system too much. For further numerical research on propeller-wing systems, where fewer configurations have to be evaluated, it is recommended to include the Prabhu-Rethorst correction.

For the specific correction, it could be explored whether a method could be developed such that the correction can be applied such that the velocity ratio remains smaller than one for all axial velocity distributions within the propeller slipstream, such that it complies with the assumptions made by Rethorst [34].

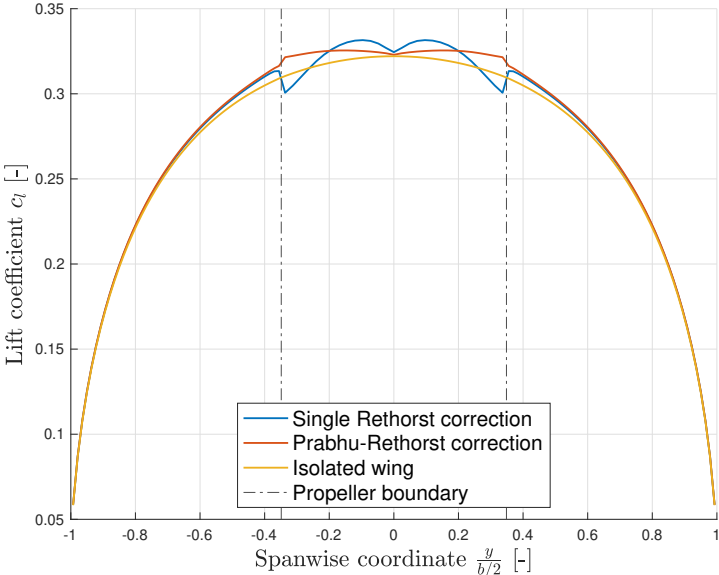


Figure D.4: Corrections for the propeller at OP 1 axial velocity distribution.